COMPUTATIONAL SCREENING FOR SINGLE METAL ATOM CATALYSTS ON $Mo_2B_2O_2$ FOR HIGH PERFORMANCE CATHODE MATERIALS OF LITHIUM-SULFUR BATTERIES

WONGSATHORN KAEWRAUNG

A Thesis Submitted in Partial Fulfillment of the Requirements for the
Degree of Master of Science in Chemistry
Suranaree University of Technology
Academic Year 2024

การคัดกรองตัวเร่งปฏิกิริยาอะตอมเดี่ยวโลหะทรานซิชันบน $Mo_2B_2O_2$ ด้วยวิธีเชิงคำนวณเพื่อใช้เป็นวัสดุแคโทดประสิทธิภาพสูงสำหรับแบตเตอรี่ลิเธียมซัลเฟอร์

นายวงศธร แก้วเรือง

วิทยานิพนธ์นี้เป็นส่วนหนึ่งของการศึกษาตามหลักสูตรปริญญาวิทยาศาสตรมหาบัณฑิต
สาขาวิชาเคมี
มหาวิทยาลัยเทคโนโลยีสุรนารี
ปีการศึกษา 2567

COMPUTATIONAL SCREENING FOR SINGLE METAL ATOM CATALYSTS ON $Mo_2B_2O_2$ FOR HIGH PERFORMACE CATHODE MATERIALS OF LITHIUM-SULFUR BATTERIES

Suranaree University of Technology has approved this thesis submitted in partial fulfillment of the requirements for a Master's Degree.

Thesis Examining Committee

(Prof. Dr. Kritsana Sagarik)
Chairperson

(Assoc. Prof. Dr. Suwit Suthirakun)
Member (Thesis Advisor)

(Dr. Anchalee Junkaew)
Member (Thesis Co-Advisor)

(Assoc. Prof. Dr. Thanayuth Kaewmaraya)
Member

(Assoc. Prof. Dr. Kamonwad Ngamchuea)
Member

(Assoc. Prof. Dr. Yupaporn Ruksakulpiwat)
Vice Rector for Academic Affairs
and Quality Assurance

(Prof. Dr. Santi Maensiri)
Dean of the Institute of Science

วงศธร แก้วเรือง : การคัดกรองตัวเร่งปฏิกิริยาอะตอมเดี่ยวโลหะทรานซิชันบน $Mo_2B_2O_2$ ด้วยวิธีเชิงคำนวณเพื่อใช้เป็นวัสดุแคโทดประสิทธิภาพสูงสำหรับแบตเตอรี่ลิเธียมซัลเฟอร์ (COMPUTATIONTATIONAL SCREENING FOR SINGLE ATOM CATALYSTS ON $Mo_2B_2O_2$ FOR HIGH PERFORMANCE CATHODE MATERIALS OF LITHIUM-SULFUR BATTERIES)
อาจารย์ที่ปรึกษา : รองศาสตราจารย์ ดร.สุวิทย์ สุธีรากุล, 135 หน้า.

คำสำคัญ: แบตเตอรีลิเธียม-ซัลเฟอร์ตัวเร่งปฏิกิริยาอะตอมเดี่ยว โลหะทรานซิชันสองมิติ MBene ทฤษฎีฟังก์ชันนอลความหนาแน่น การคำนวณหลักการแรก

แบตเตอรีลิเธียม-ซัลเฟอร์นับว่าเป็นทางเลือกที่น่าสนใจแทนแบตเตอรีลิเทียม-ไอออนแบบดั้งเดิม เนื่องจากมีความหนาแน่นพลังงานในทางทฤษฎีสูงและต้นทุนการผลิตต่ำกว่า อย่างไรก็ตาม ประสิทธิภาพของแบตเตอรีชนิดนี้ยังถูกจำกัดด้วยปัญหาการลดลงของความจุ ซึ่งส่วนใหญ่เกิดจากปรากฏการณ์ที่เรียกว่า “shuttle effect” และการสลายตัวของลิเทียโพลีซัลไฟด์ในสถานะของแข็งที่เป็นไปอย่างเชื่องช้า ในวิทยานิพนธ์ฉบับนี้ ได้ใช้การคำนวณตามหลักการแรก เพื่อเสนอให้ใช้วัสดุ $Mo_2B_2O_2$ ที่ตกแต่งด้วยอะตอมเดี่ยวเป็นวัสดุแคโทดที่มีศักยภาพสำหรับแบตเตอรีลิเทียม-ซัลเฟอร์ จากผลศึกษาพบว่า โลหะทรานซิชัน 3*d* และ 4*d* สามารถเพิ่มความสามารถในการดูดซับลิเทียโพลีซัลไฟด์ได้อย่างมีนัยสำคัญผ่านการสร้างพันธะระหว่างโลหะทรานซิชันและซัลเฟอร์ ความแตกต่างของความแข็งแรงในการดูดซับ LiPSs ระหว่างโลหะทรานซิชัน 3*d* และ 4*d* นั้นมาจากความแตกต่างในโครงสร้างอิเล็กทรอนิกส์ คุณสมบัติทางเรขาคณิต การเติมอิเล็กตรอนในไฮบริไดเซชันระหว่าง d กับ p ออร์บิทัล และระดับพลังงานของสถานะ d ของแต่ละอะตอมเดี่ยว ซึ่งส่งผลให้เกิดรูปแบบการดูดซับที่แตกต่างกันในแต่ละกลุ่ม การเติมอะตอมเดี่ยวไม่เพียงแต่ช่วยเสริมความแข็งแรงของการดูดซับ แต่ยังช่วยส่งเสริมการเปลี่ยนแปลงลิเทียโพลีซัลไฟด์ที่ละลายได้ให้กลายเป็นชนิดที่ไม่ละลายขนาดเล็กลง ซึ่งช่วยลดปัญหาลิเทียโพลีซัลไฟด์ละลายและ shuttle effect ได้อย่างมีประสิทธิภาพ ในบรรดาวัสดุทั้งหมด วัสดุ V- และ Nb-$Mo_2B_2O_2$ แสดงความสามารถในการดูดซับลิเทียโพลีซัลไฟด์ที่แข็งแกร่งที่สุดและมีการเร่งปฏิกิริยาในกระบวนปฏิกิริยารีดักชันของกำมะถันที่ยอดเยี่ยม การศึกษานี้จึงให้ข้อมูลเชิงลึกและแนวทางเชิงกลยุทธ์ในการออกแบบวัสดุที่มีประสิทธิภาพสูง ซึ่งช่วยเพิ่มความเสถียรและประสิทธิภาพของแบตเตอรีลิเทียม-ซัลเฟอร์อย่างก้าวหน้า

สาขาวิชาเคมี ลายมือชื่อนักศึกษา Wongsathorn
ปีการศึกษา 2567 ลายมือชื่ออาจารย์ที่ปรึกษา
ลายมือชื่ออาจารย์ที่ปรึกษาร่วม

WONGSATHORN KAEWRAUNG : COMPUTATIONAL SCREENING FOR SINGLE ATOM CATALYSTS ON $Mo_2B_2O_2$ FOR HIGH PERFORMANCE CATHODE MATERIALS OF LITHIUM-SULFUR BATTERIES.
THESIS ADVISOR : ASSOC. PROF. SUWIT SUTHIRAKUN, Ph.D. 135 PP.

Keyword: Lithium-sulfur batteries, Single-atom catalysts, Transition metal borides (MBene), Density functional theory (DFT), First-principles method

Lithium-sulfur (Li-S) batteries offer a promising alternative to traditional lithium-ion batteries, boasting a high theoretical energy density and lower production costs. Nevertheless, their performance is hindered by capacity fading and poor cycling stability, mainly caused by the shuttle effect of soluble lithium polysulfides (LiPSs) and the sluggish decomposition of solid LiPSs. In this thesis, the first-principles calculations were employed to suggest single-atom (SA) decorated $Mo_2B_2O_2$ (SA-$Mo_2B_2O_2$) as a potential cathode material for Li-S batteries. The results suggested that 3*d*- and 4*d*-transition metals significantly enhance LiPS adsorption through the formation of strong transition metal-sulfur (TM-S) bonds. Variations in LiPS adsorption strength between 3*d*- and 4*d*-transition metals are attributed to differences in their electronic structures, geometric properties, electron filling in d-p hybridization, and energy level of d states of each SA, leading to distinct adsorption patterns for each group. SA doping not only strengthens LiPS adsorption but also promotes the conversion of soluble LiPSs into smaller, insoluble species, effectively alleviating LiPSs dissolution. Among SA-$Mo_2B_2O_2$, V- and Nb-$Mo_2B_2O_2$ show the strongest LiPS adsorption and exceptional catalytic activities in the sulfur reduction reaction (SRR), reducing the shuttle effect and enhancing charge-discharge efficiency. This study provides valuable insights and a strategic approach for designing high-performance SA-$Mo_2B_2O_2$ cathodes, advancing the stability and efficiency of Li-S batteries.

School of Chemistry
Academic Year 2024

Student's Signature Wongsathorn
Advisor's Signature
Co-Advisor's Signature

ACKNOWLEDGEMENTS

I am deeply grateful to my thesis advisor, Assoc. Prof. Dr. Suwit Suthirakun, and my co-advisors, Dr. Anchalee Junkaew, for their constant support, valuable guidance, thoughtful discussions, and ongoing encouragement throughout my thesis journey. Their knowledge and dedication have been essential to the success of this research. I sincerely thank Prof. Dr. Kritsana Sagarik, Assoc. Prof. Dr. Thanayuth Kaewmaraya, and Assoc. Prof Dr. Kamonwad Ngamchuea for their time and expertise as members of my thesis committee. Their valuable feedback and guidance have significantly improved this work. I am truly thankful to the Development and Promotion of Science and Technology Talents Project (DPST, Thailand) for granting me a scholarship that made it possible to pursue my master's degree. I also appreciate the financial support from Suranaree University of Technology (SUT), which was crucial for completing this research. I am grateful to the NSTDA Supercomputer Center (ThaiSC) and the Institute of Science, Suranaree University of Technology, for providing the computational resources essential for this research. I also thank the faculty and staff of the School of Chemistry, Institute of Science, Suranaree University of Technology, for their support, guidance, and encouragement throughout my academic journey. I sincerely thank Sirisak Singsen and Lappawat Ngamwongwan for their guidance, patience, and practical advice on computational techniques, which greatly improved the quality of my research. I am also truly grateful to my friends and colleagues in the Computational Materials Science and Catalysis (COMSCAT) Group for their support, teamwork, and encouragement, making my academic journey both productive and enjoyable. Finally, I am truly grateful to my family and my girlfriend, Ms. Jutikan Uttamoth, for their unwavering love, support, and belief in me. I sincerely thank everyone who has supported and contributed to this work, whether directly or indirectly. Your guidance, encouragement, and assistance have been invaluable and deeply appreciated.

Wongsathorn Kaewraung

CONTENTS

Page

ABSTRACT IN THAI I

ABSTRACT IN ENGLISH II

ACKNOWLEDGEMENTS III

CONTENTS IV

LIST OF TABLES VII

LIST OF FIGURES VIII

LIST OF ABBREVIATIONS XV

CHAPTER

I INTRODUCTION 1

1.1 Introduction 1

1.2 Research objectives 6

1.3 Scope and limitations 6

1.4 References 7

II LITERATURE REVIEW 11

2.1 Overview of lithium-sulfur batteries (Li-S batteries) 11

2.2 Study sulfur reduction reaction and sulfur evolution reaction 16

2.3 Developing cathode materials to address challenges 20

2.4 Mo_2B_2-based MBene with oxygen functionalization 22

2.5 Single-atom catalysts 25

2.6 Reference 31

III CALCULATION DETAILS 39

3.1 Schrödinger equation for many particles problem 40

3.2 Density functional theory 41

3.2.1 The Hohenberg-Kohn theorems 41

3.2.2 The Kohn-Shamequation 42

3.2.3 Exchange-correlation functional 45

CONTENTS (Continued)

Page

3.2.4 Pseudopotential 45
3.2.4 Self-Consistent Field approach 45
3.3 Geometry optimization 49
3.4 vdW correction 51
3.5 Climbing image nudged elastic band method 53
3.6 Ab initio molecular dynamics 55
3.7 Gibbs free energy (G) calculation 57
3.8 Crystal orbital Hamilton population (COHP) 58
3.9 Summary of computational details 60
3.10 References 61

IV STRUCTURAL AND ELECTRONIC PROPERTIES OF $Mo_2B_2O_2$ AND SINGLE ATOM DECOATED $Mo_2B_2O_2$ 63

4.1 Geometric and Electronic properties of calculated pristine and SA decorated $Mo_2B_2O_2$ 64
4.2 Key Properties of Single Atoms Affecting the Stability of SA-$Mo_2B_2O_2$ 71
4.3 References 76

V SUPPRESSION OF THE SHUTTLE EFFECT BY SINGLE ATOM DECORATION 77

5.1 Effect of Single-Atom Decoration on LiPSs Adsorption Energy in $Mo_2B_2O_2$ 77
5.2 LiPSs Adsorption Energy When Surrounded by Solvent Molecules 89
5.3 References 92

VI TRANSITION METAL TYPES AND THEIR EFFECT ON LiPSs ADSORPTION 94

6.1 Study Properties of SA-$Mo_2B_2O_2$ Affecting LiPSs Adsorption 94
6.2 Effect of Electron Occupancy in d-p Hybridization on Li_2S_6 Adsorption 99
6.3 Selective Orbital Coupling 109
6.4 References 113

CONTENTS (Continued)

Page

VII ELECTROCHEMICAL REACTION OF SULFUR ON SA-$Mo_2B_2O_2$ 114

7.1 SRR Catalytic Activity of Pristine and SA-$Mo_2B_2O_2$ 114

7.2 Oxidation Reaction Process of Pristine and SA-$Mo_2B_2O_2$ 120

7.3 References 125

VII CONCLUSIONS 127

APPENDIX 129

CURRICULUM VITAE 135

LIST OF TABLES

Table **Page**

4.1 SA adsorption energy and SA diffusion energy barrier for each SA-$Mo_2B_2O_2$ ... 70

4.2 Description of properties to find correlation with SA adsorption energies.....72

5.1 Geometric parameters of optimized molecular and bulk structure S_8/LiPS species..... 78

5.2 Bond lengths of S-S at different positions for Li_2S_6 and Li_2S_4 adsorption on SA-$Mo_2B_2O_2$ (3*d*-transition metals).....85

5.3 Bond lengths of S-S at different positions for Li_2S_6 and Li_2S_4 adsorption on SA-$Mo_2B_2O_2$ (4*d*-transition metals).....86

5.4 Charge of Li_2S_6, SA, and surface oxygen atom (O) in pristine and SA-$Mo_2B_2O_2$..... 88

6.1 Description of properties to find correlation, including electronic properties (green region) and geometric properties (red region)..... 95

LIST OF FIGURES

Figure **Page**

1.1 Volumetric and gravimetric energy densities of Li-S batteries compared to those of other batteries....2

1.2 Battery configurations of Li–S battery, including sulfur–carbon cathode, metallic, lithium anode, electrolyte, and separator....3

2.1 Schematic diagram of a commercial Li-S battery configuration, featuring a graphene-sulfur composite as the cathode and lithium metal as the anode.... 11

2.2 (a) Voltage profile and chemical reactions occurring at the sulfur cathode. (b) Sulfur K-edge XANES spectra and reference spectra illustrating changes in absorbance during electrochemical cycling, with charge and discharge endpoints indicated in red.... 13

2.3 Scheme of polysulfide shuttle effect.... 14

2.4 Problems during the charge and discharge process of Li-S batteries.... 15

2.5 Energy profile for the reduction of polysulfides on TM@NG, excluding the contributions of electrons and lithium ions.... 17

2.6 Energy profile for the reduction of polysulfides and overpotential of rate-limiting step.... 18

2.7 Energy barrier graphs for Li_2S decomposition with configuration of TM-N_4-C.. 19

2.8 (a) Density of states for Ni and Co phosphides showing d-band shift caused by Co doping, where E_F represents Fermi energy level. (b) Change in activation energy for Li_2S nucleation when using Ni_2P and $Ni_2Co_4P_3$ as cathode materials.... 21

2.9 Structure and classification of MAB and related MBene phases by their crystal structures.... 23

2.10 The crystal structures of Mo-B phases obtained through an evolutionary Crystal structure search.... 23

LIST OF FIGURES (Continued)

Figure **Page**

2.11 Schematics illustrating the variation in surface free energy and specific activity per metal atom as a function of metal particle size, along with the role of support in stabilizing single atoms 25

2.12 Illustration of the structure of the reducible support, non-reducible support and metal NPs sintering/dispersing on different supports 26

2.13 (a) Decomposition barriers of Li_2S and (b) Li-ion diffusion barriers of different SA-NG. (c) Li_2S_6 binding energy of each SA-NG 28

2.14 (a) Gibbs free energy for HER after introducing different metal single atoms on $Mo_2B_2O_2$ and $W_2B_2O_2$, respectively 29

2.15 Schematic representation of suitable configuration SA decorated on $Mo_2B_2O_2$ 30

3.1 Comparison of wavefunctions in a nuclear Coulomb potential (blue) and a pseudopotential (red) 47

3.2 Flowchart showing the process of solving the Kohn-Sham equation 48

3.3 Schematic representation of the optimization process in DFT calculations. ... 51

3.4 Schematic of the potential energy surface (PES) and NEB calculation, showing the initial reaction pathway (white line) and the optimized reaction pathway (black line). 54

4.1 The most stable structure of $Mo_2B_2O_2$ before being decorated with SA 64

4.2 The possible configuration of the single transition metal atom on $Mo_2B_2O_2$ surface. Mo, B, O, and single transition metal (SA) atoms are represented by purple, green, red, and blue, respectively. 65

4.3 Configuration of SA-$Mo_2B_2O_2$, including 3*d*- and 4*d*-transtion metals. It exhibited average SA-O bond length of each substance (Avg of $d_{SA\text{-}O}$) and SA adsorption energy ($E_{ads,SA}$) 66

LIST OF FIGURES (Continued)

Figure **Page**

4.4 Correlation between SA adsorption energy and atomic number for 3*d*- and 4*d*-transition metals. 68

4.5 Potential energy profiles of (a) Li ion diffusion and (b) V ion diffusion on $Mo_2B_2O_2$. The relationship between the SA diffusion energy barrier and (c) atomic number and (d) SA adsorption energy for each period. In case of SA diffusion energy barrier compared with SA adsorption energy was separated by two regions, including green region (energy barrier more than 1.0 eV) and red region (energy barrier less than 1.0 eV). 69

4.6 Projected density of states (PDOS) of $Mo_2B_2O_2$ and the example of SA-$Mo_2B_2O_2$ which are V- and Nb-$Mo_2B_2O_2$. Femi level is adjusted to 0 eV. 70

4.7 Heatmap of Pearson correlation coefficient matrix for SA adsorption energy of 3*d*- and 4*d*-transition metals 73

4.8 Feature correlation between properties and $E_{ads,SA}$ for each period. The x value represents the strength of correlation between pairs of variables, represented by Pearson correlation coefficients. A darker color suggests a stronger correlation with SA adsorption energy compared to other features. 74

4.9 Crystal orbital Hamilton population (COHP) graph of the shortest SA-O bond for each example SA-$Mo_2B_2O_2$ from each period. Spin up and Spin down states were showed through red and black line. Green area suggests bonding orbital states, whereas antibonding orbital states were represented in red area 75

5.1 The relaxed (a) molecular structures of LiPS species and (b) bulk structures of S_8 and Li_2S 78

LIST OF FIGURES (Continued)

Figure		Page
5.2	Suitable adsorption configurations of Li_2S_6 on pristine $Mo_2B_2O_2$	79
5.3	Suitable adsorption configurations of Li_2S_6 on SA-$Mo_2B_2O_2$ of 3*d*-transition metals	81
5.4	Suitable adsorption configurations of Li_2S_6 on SA-$Mo_2B_2O_2$ of 4*d*-transition metals	83
5.5	The Li_2S_x adsorption energy of 3*d*- and 4*d*-transition metals, including Li_2S, Li_2S_2, Li_2S_4, and Li_2S_6	83
5.6	Li_2S_6 adsorption energies of various SA-$Mo_2B_2O_2$ compared to the pristine $Mo_2B_2O_2$ (dashed line)	84
5.7	S-S bond breaking positions for Li_2S_6 and Li_2S_4 adsorption on SA-$Mo_2B_2O_2$, with numbered sulfur positions.	85
5.8	Projected density of states (PDOS) of Li_2S_6 adsorbed on $Mo_2B_2O_2$ and the example of SA-$Mo_2B_2O_2$ which are V- and Nb-$Mo_2B_2O_2$. Femi level is adjusted to 0 eV.	87
5.9	The most stable configuration and degree of charge transfer of Li_2S_6 molecule adsorbed on pristine $Mo_2B_2O_2$, V- and Nb-$Mo_2B_2O_2$.	87
5.10	Initial configurations of pristine, V-, and Nb-$Mo_2B_2O_2$ surrounded by DOL and DME molecules before AIMD simulation...	90
5.11	Low-energy configurations of (a) DOL- and (b) DME-solvated Li_2S_6. All configurations were calculated using AIMD with a time step of 1 fs for 10 ps...	91
6.1	Representation of computational approaches for determining interaction energy (E_{int}) and decomposition energy of Li_2S_6 ($E_{dis-Li_2S_x}$) and SA-$Mo_2B_2O_2$ ($E_{\mathbf{dis-sub}}$)	96
6.2	Pearson correlation heatmap for properties influencing LiPSs adsorption by 3*d*- and 4*d*-transition metals	97

LIST OF FIGURES (Continued)

Figure **Page**

6.3 Feature correlation analysis between properties of SA/SA-$Mo_2B_2O_2$ and target, including $E_{Li_2S_6}$, E_{int}, $E_{dis-Li_2S_6}$ for each period. The x-axis represents the Pearson correlation coefficients, representing the strength of correlation between variable pairs. Darker colors suggest stronger correlations with SA adsorption energy relative to other features.....98

6.4 (a) Ligand field theory diagram with (b) example PDOS of SA-$Mo_2B_2O_2$, including V- and Nb-$Mo_2B_2O_2$ 100

6.5 Schematic illustration of analysis projected density of states (PDOS) for Ligand Field Theory writing, as shown in Ti-$Mo_2B_2O_2$ example..... 101

6.6 (a) Projected density of states (PDOS) of example SA-$Mo_2B_2O_2$ which show SA-O bonding are more negative energy than SA-S bonding. (b) Considering PDOS of Zn and Cd-$Mo_2B_2O_2$, d^{10} transition metals, that show p state of S and Zn near Femi energy. 101

6.7 Ligand field theory diagrams with PDOS of each 3*d*-transtion metal for SA-$Mo_2B_2O_2$..... 102

6.8 Ligand field theory diagrams with PDOS of each 4*d*-transtion metal for SA-$Mo_2B_2O_2$..... 103

6.9 Crystal orbital Hamilton population (COHP) graph of 3*d*-transition metals for SA-$Mo_2B_2O_2$ when Li_2S adsorbed. Spin up and Spin down states were showed through red and black line. Green area suggests bonding orbital states, whereas antibonding orbital states were represented in red area. 104

LIST OF FIGURES (Continued)

Figure **Page**

6.10 Crystal orbital Hamilton population (COHP) graph of 4*d*-transition metals for SA-$Mo_2B_2O_2$ when Li_2S adsorbed. Spin up and Spin down states were showed through red and black line. Green area suggests bonding orbital states, whereas antibonding orbital states were represented in red area. 105

6.11 This diagram shows the methods for filling electron states in response to changes in the type of transition metal, with groups separated by color regions. Zn- and Cd-$Mo_2B_2O_2$ are excluded from consideration due to their use of p states in bonding with sulfur (S) atoms. 107

6.12 Ligand field theory diagrams with PDOS of Pd-$Mo_2B_2O_2$. 108

6.13 Relationship between transition complex bond order and Li_2S adsorption energy on SA-$Mo_2B_2O_2$ for 3*d*- and 4*d*-transition metals. 108

6.14 PDOS of d states of each SA-$Mo_2B_2O_2$ and π state of isolate S_2 molecule. The gray dashed line represents the Fermi level, while the blue dashed line indicates the $\pi^*\downarrow$ energy level. 110

6.15 PDOS for S_2 adsorbed on V- and Nb-$Mo_2B_2O_2$. The gray dashed line represents the Fermi level. 110

6.16 Relationship between the energy level of $d_{x^2-y^2}\downarrow$ state and the integrated crystal orbital Hamilton populations (-ICOHP), using the $\pi^*\downarrow$ energy level as a reference. The blue dashed line indicates the $\pi^*\downarrow$ energy level. 112

7.1 Gibbs free energy diagram for conversion from Li_2S_4 to Li_2S when adsorbed on pristine and SA-$Mo_2B_2O_2$ of 3*d*-transition metals at U_{eq} = 2.15 V 116

LIST OF FIGURES (Continued)

Figure **Page**

7.2 Gibbs free energy diagram for conversion from Li_2S_4 to Li_2S when adsorbed on pristine and SA-$Mo_2B_2O_2$ of 4*d*-transition metals at U_{eq} = 2.15 V 117

7.3 Overpotential for the Li_2S_4* to Li_2S* conversion steps at an equilibrium potential of U_{eq} = 2.15 V for SA-$Mo_2B_2O_2$ systems with 3*d*- and 4d-transition metal single atom (SA) 118

7.4 Gibbs free energy diagram showing conversion from S_8 to Li_2S when adsorbed on pristine and three representative SA-$Mo_2B_2O_2$ system from 3*d*- and 4*d*-transition metals at *U* = 0 eV 119

7.5 Gibbs free energy diagram for sulfur reduction reaction (SRR) of pristine and various SA-$Mo_2B_2O_2$ at U_{eq} = 2.15 V. The SRR process consists of five electron transfer steps and the final Li_2S nucleation step that does not involve electron transfer 120

7.6 Potential energy profiles for Li ion diffusion on pristine and candidates SA-$Mo_2B_2O_2$ surfaces, with initial state (IS), transition state (TS), and final state (FS) 121

7.7 Potential energy profiles of Li diffusion through [100] for V- and Nb-$Mo_2B_2O_2$ 122

7.8 Potential energy profiles of S diffusion from SA site through [100] for V- and Nb-$Mo_2B_2O_2$ 123

7.9 Most stable configurations of sulfur poisoning before and after the adsorption of Li_2S_6 and Li_2S on V- and Nb-$Mo_2B_2O_2$ 124

7.10 Low-energy configurations of (a) DME- and DOL-solvated Li_2S_6, and (c) DME- and (d) DOL-solvated Li_2S_6 under sulfur poisoning on candidates SA-$Mo_2B_2O_2$. All configurations were calculated using AIMD with a time step of 1 fs for 10 ps. In summary, both pristine and SA-$Mo_2B_2O_2$ effectively facilitate 124

LIST OF ABBREVIATIONS

Li	= Lithium
S	= Sulfur
DOL	= 1,3-dioxolane
DME	= 2-dimethoxyethane
LiPS	= Lithium polysulfide
SA	= Single atom
SAC	= Single atom catalysts
TM	= Transition metal
SRR	= Sulfur reduction reaction
CV	= Cyclic voltammograms
ALD	= Atomic layer deposition
CVD	= Chemical vapor deposition
XPS	= X-ray photoelectron spectroscopy
DFT	= Density functional theory
AIMD	= Ab-initio molecular dynamics
VASP	= Vienna ab initio simulation package
GGA	= Generalized gradient approximation
PDOS	= Projected density of states
PAW	= Projector-augmented wave
PBE	= Perdew-Burke-Ernzerhof
CI-NEB	= Climbing image-nudged elastic band
TS	= Transition state
XC	= Exchange-correlation
SCF	= Self-consistent field
NEB	= Nudged elastic band
COHP	= Crystal orbital Hamilton population
LFT	= Ligand Field Theory

CHAPTER I

INTRODUCTION

The world's energy use is increasing rapidly because of population growth and industrial development. Currently, humanity's use of fossil fuels is causing serious environmental harm. Fossil fuel consumption leads to local pollution, impacting air quality and ecosystems. Additionally, the greenhouse gases emitted from fossil fuel consumption are a major driver of global climate change.

To solve these critical environmental issues, advancing energy storage technologies that support renewable energy sources has become essential (Solaun et al., 2019). They use an electrochemical process to give energy instead of burning fossil fuels. Rechargeable batteries, particularly lithium-ion (Li-ion) batteries, are among the most promising solutions and are widely used in portable electronics, electric vehicles, and grid energy storage. Li-ion batteries store energy through a process known as Li-ion intercalation, where lithium ions move between the battery's anode and cathode during charging and discharging cycles (Yangtao Liu et al., 2021). Despite their broad applications, Li-ion batteries have inherent limitations regarding their theoretical specific capacities and energy density (387 Wh kg^{-1}, 155 mA h g^{-1}) (Yuqing Chen et al., 2021). Consequently, developing new materials and innovative technologies that can exceed these limitations is crucial to the future of high-capacity battery technologies. Among the new battery technology, lithium-sulfur (Li-S) batteries have gained significant attention due to their high theoretical capacity (2600 Wh kg^{-1}) and energy density (1672 mA h g^{-1}) (Wild et al., 2015), as shown in **Figure 1.1**.

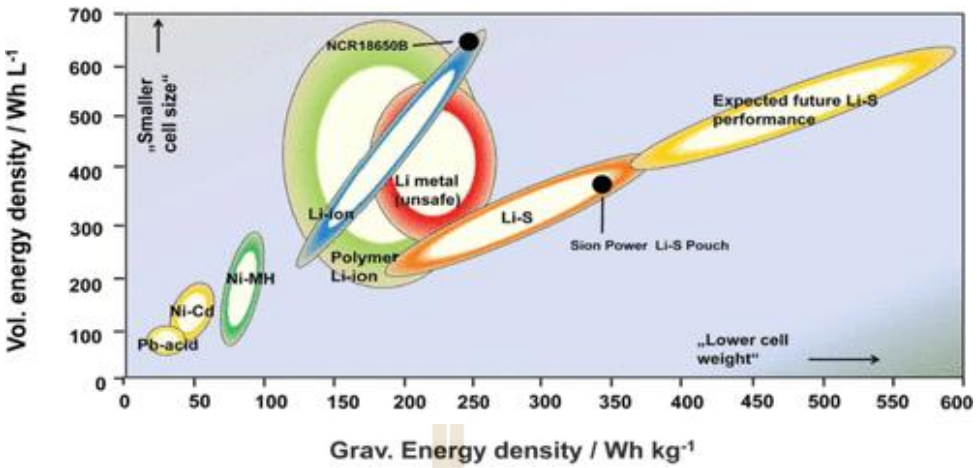

Figure 1.1 Volumetric and gravimetric energy densities of Li-S batteries compared to those of other batteries (Hagen et al., 2015).

A typical Li-S battery consists of two electrodes: a lithium metal anode and a sulfur-based cathode. Between these electrodes is a separator and a conductive electrolyte, which can be either liquid or solid (**Figure 1.2**) (Barghamadi et al., 2013). They play a critical role in maintaining ion conductivity and preventing direct contact between the anode and cathode. A key advantage of Li-S batteries is their sulfur cathode, as sulfur is both environmentally friendly and low-cost. The high capacity of Li-S batteries is achieved through a sulfur reduction reaction (SRR). During the discharge process, lithium ions (Li^+) from the anode react with sulfur molecules (S_8) at the cathode, producing lithium polysulfides (LiPSs). These LiPSs consist of both long-chain molecules (Li_2S_x where x = 4, 6, 8) with high solubility, and short-chain molecules (Li_2S_2 and Li_2S) that are solid with high resistivity (Scheers et al., 2014).

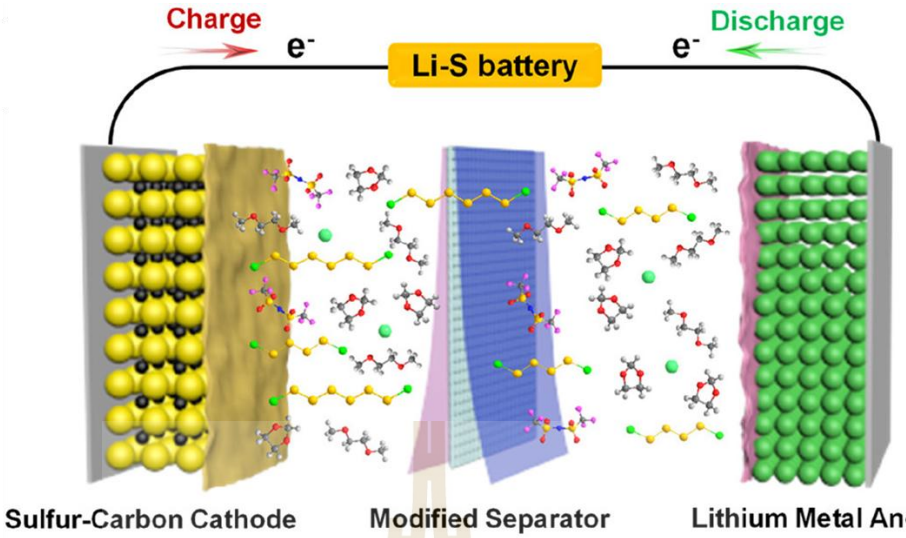

Figure 1.2 Schematic illustration of Li–S battery, including sulfur–carbon cathode, metallic lithium anode, electrolyte, and separator (Li et al., 2019).

While their high capacity and energy density make Li-S batteries attractive as an alternative to Li-ion batteries, they still face several challenges that negatively impact their Coulombic efficiency and stability. Three primary issues suppress Li-S battery performance:

(1) The intermediate LiPSs, including Li_2S_8, Li_2S_6, and Li_2S_4, are soluble in electrolytes. These soluble LiPSs enable the diffusion to the anode side where they are electrochemically reduced and chemically reacted to Li_2S_2/Li_2S covering the anode, resulting in a self-discharge process. This phenomenon, commonly known as the “shuttle effect”, causes loss of sulfur content, reduces Coulombic efficiency, and accelerates battery degradation (Xiong et al., 2014).

(2) During the discharge process, final products like solid lithium polysulfides (LiPSs), such as Li_2S_2 and Li_2S, form on the cathode surface. These compounds are highly insulating, leading to increased internal resistance. The strong chemical bonds between Li and S in Li_2S_2 and Li_2S result in sluggish reaction kinetics, causing slower redox reactions and prolonged charging times (Manthiram et al., 2015).

(3) The cathode material undergoes significant volumetric changes during the SRR reaction, leading to mechanical stress that can cause cracking and structural degradation. This mechanical failure results in battery performance and cycling stability (T. Wang et al., 2017).

To address these challenges, researchers have focused on developing advanced cathode materials, as many issues originate from this electrode. Recent studies have explored materials that have adsorption-catalysis dual properties to manage soluble and insoluble LiPSs. Notable materials frequently studied in research include graphene (Y. Zhang et al., 2018), carbon nanotubes (M. Zheng et al., 2019), transition metal oxides (Da Zhang et al., 2021), metal-organic frameworks (MOFs) (Y. Zheng et al., 2019), MXene (Z. Xiao et al., 2019), and MBene (Y. Xiao et al., 2021). Among these materials, MBenes show great potential for improving the performance of high-performance Li-S batteries.

MBenes are a novel family of two-dimensional (2D) materials with excellent electrical conductivity, high stability, and large surface area (Hayat et al., 2024). They are synthesized by etching three-dimensional (3D) materials, including M_2AB_2 and MAB, where M denotes an early transition metal, A represents aluminum, and B stands for boron (Gennady et al., 1994). However, only a few 2D phases, such as Ti_2B_2, Mo_2B_2 and Cr_2B_2, can be synthesized. These are produced by selectively etching away the aluminum layer from precursor compounds, including Ti_2InB_2 (J. Wang et al., 2019), MoAlB (Alameda et al., 2018), and Cr_2AlB_2 (H. Zhang et al., 2018), respectively.

Additionally, during the etching process, functional groups such as O-, F-, -OH, and others typically form on the surface of MBene, depending on the etching solution used. These surface-functional groups enhance the hydrophilicity of MBene materials and influence their electrochemical properties (Khaledialidusti et al., 2021). In the context of Li-S batteries, Xiao et al. reported the functionalization of Mo_2B_2 with surface groups such as O and F, finding that the O-functionalized Mo_2B_2 significantly improved battery performance. The presence of the O surface group alleviate the polysulfide shuttling effect and reduced the decomposition barrier of Li_2S, thus enhancing both the cycle life and capacity of the battery (Y. Xiao et al., 2021). Although pristine show good performance, further improvements are still necessary.

Introducing single-atom catalysts (SACs) into electrode materials is considered as a promising strategy to enhance the performance of Li-S batteries. SACs offer the benefit of atomic-level precision, which provide high atomic utilization and maximize the active sites for catalytic reactions. SACs usually use transition metal atoms, which act as Lewis acid site for accepting electrons from LiPSs, due to partially filled d-orbitals, resulting in boosting cathode performance (Yuanjun Chen et al., 2018). Recent studies reported that SACs, such as SA-graphene (Yang et al., 2021), SA-MoS_2 (Yanyun Liu et al., 2020), and SA-MXene (Di Zhang et al., 2020), can help reduce energy barriers of the SRR process and alleviate the shuttle effect by anchoring polysulfides at single-atom (SA) sites. However, the effect of SA with MBene for Li-S batteries are still not fully understood.

In this study, we study the role of single transition metal atoms on MBene as cathode materials for Li-S batteries using the density functional theory (DFT). Specifically, we focus on the Mo_2B_2 structure with oxygen functionalization ($Mo_2B_2O_2$), a promising type of MBene known for its excellent catalytic and conductive properties. We screened 19 transition metal atoms from 3*d* and 4*d*, excluding Mo, as it is already present in the $Mo_2B_2O_2$ structure. In the initial step, we explored the most stable adsorption sites for SA by calculating their adsorption energies and diffusion on the $Mo_2B_2O_2$ surface. Next, we examined the adsorption configurations of LiPSs to understand how SA decoration helps suppress the shuttle effect. We then selected the single atom decorated on $Mo_2B_2O_2$ (SA-$Mo_2B_2O_2$) with the strongest LiPSs adsorption to further study the effect of explicit solvent molecule on the LiPS adsorption using ab initio molecular dynamics (AIMD) simulations in a 1,3-dioxolane (DOL) and 2-dimethoxyethane (DME) solvents. Additionally, we rationale the correlation between adsorption strength of LiPS and transition metals. Finally, we examined the catalytic activity of sulfur reduction reaction (SRR) and the oxidation of Li_2S in these SA-$Mo_2B_2O_2$ configurations, as these are critical properties for improving Li-S battery performance.

1.1 Research objectives

The objective of this research is to use first-principles computations to screen single-transition metal atom catalysts on the $Mo_2B_2O_2$ for (i) suppressing shuttle effect of large LiPSs, (ii) effectively converting S_8 to $L_{i2}S$ in SRR during the discharge process, and (iii) decomposing Li_2S_2 and Li_2S during the charge process. The configuration and electronic properties of different SA were analyzed both before and after LiPSs adsorption to rationale the strong interaction between LiPSs and SA-$Mo_2B_2O_2$. Additionally, we studied the d-orbital energy states of each single atom to explain the varying adsorption behaviors. After studying adsorptivity, we examined the performance of the SRR and the oxidation process related to Li_2S decomposition to suggest which SA-$Mo_2B_2O_2$ can facilitate both reduction and oxidation process during charging/discharging. By understanding the role of SA and selecting the most effective SA-$Mo_2B_2O_2$, this study can provide guidance for future experimental and theoretical studies on SA-$Mo_2B_2O_2$ to enhance the performance of Li-S batteries.

1.2 Scope and limitations

In this thesis, we screen SA-$Mo_2B_2O_2$ to find the best performance materials through computational calculations. The materials should exhibit strong LiPSs adsorption and facilitate reduction and oxidation processes. The calculations use spin-polarized density functional theory (DFT) method with the plane-wave technique, as implemented in the Vienna Ab initio Simulation Package (VASP 5.4.) (Kresse et al., 1996a, 1996b). The frozen-core projector augmented wave (PAW) method is used to model the electron-ion interactions (Blöchl, 1994), while the generalized gradient approximation (GGA) with the Perdew-Burke-Ernzerhof (PBE) functional approximates the exchange-correlation interactions (Perdew et al., 1996). For $Mo_2B_2O_2$, we include valence electrons for Mo 4d5s, B 2s2p, O 2s2p, while for LiPS molecules, we include Li 2s and S 3s3p. For screening SA transition metals, we consider both 3*d* and 4*d* metals, accounting for their 3d4s and 4d5s valence electrons, respectively. For studies involving LiPS adsorption, we account for weak van der Waals interactions between the adsorbates and SA-$Mo_2B_2O_2$ using an DFT-D3 (Klimeš et al., 2010). Each model is

considered fully optimized when the energy difference reaches 10^{-6} eV, and residual forces fall below 0.02 eV/Å. Although DFT provides accurate total energy and configurations, it may underestimate electronic properties like the band gap. However, since previous studies have shown that pristine $Mo_2B_2O_2$ and doping with transition metal exhibits metallic behavior with no band gap (Mou et al., 2023), the accuracy of the band gap is not a primary concern in this study. We use Bader charge analysis to examine charge distribution before and after LiPS adsorption by calculating net particle charges. To study the shuttle effect in the presence of solvent molecules, we perform ab initio molecular dynamics (AIMD) simulations with a 1 fs time step over a total of 10 ps at 300 K, employing the NVT ensemble with a Nose-Hoover thermostat. This duration is sufficient to suggest any changes in the polysulfides structure within the solvent. Additionally, the crystal orbital Hamilton population (COHP) method (Mou et al., 2023) is used to analyze electron occupancy in bonding and antibonding orbitals. For calculating energy barrier regarding on SA diffusion, Li diffusion, and Li_2S decomposition, we apply the Climbing image Nudged Elastic Band (CI-NEB) method (Mou et al., 2023). The computational techniques used in this study provide insights into the role of each SA, which is essential for developing cathode materials with SA applications in the future.

1.3 References

Alameda, L. T., Moradifar, P., Metzger, Z. P., Alem, N., and Schaak, R. E. (2018). Topochemical Deintercalation of Al from MoAlB: Stepwise Etching Pathway, Layered Intergrowth Structures, and Two-Dimensional MBene. *Journal of the American Chemical Society, 140*(28), 8833-8840.

Barghamadi, M., Kapoor, A., and Wen, C. (2013). A Review on Li-S Batteries as a High Efficiency Rechargeable Lithium Battery. *Journal of The Electrochemical Society, 160*(8), A1256.

Blöchl, P. E. (1994). Projector augmented-wave method. *Physical Review B, 50*(24), 17953-17979.

Chen, Y., Ji, S., Chen, C., Peng, Q., Wang, D., and Li, Y. (2018). Single-Atom Catalysts: Synthetic Strategies and Electrochemical Applications. *Joule, 2*(7), 1242-1264.

Chen, Y., Kang, Y., Zhao, Y., Wang, L., Liu, J., Li, Y., Liang, Z., He, X., Li, X., Tavajohi, N., and Li, B. (2021). A review of lithium-ion battery safety concerns: The issues, strategies, and testing standards. *Journal of Energy Chemistry, 59*, 83-99.

Gennady, P. S., and Alexander, L. I. (1994). The chemical bonding and electronic properties of metal borides. *Russian Chemical Reviews, 63*(9), 711.

Hagen, M., Hanselmann, D., Ahlbrecht, K., Maça, R., Gerber, D., and Tübke, J. (2015). Lithium–Sulfur Cells: The Gap between the State-of-the-Art and the Requirements for High Energy Battery Cells. *Advanced Energy Materials, 5*(16), 1401986.

Hayat, A., Bashir, T., Ahmed, A. M., Ajmal, Z., Alghamdi, M. M., El-Zahhar, A. A., Sohail, M., Amin, M. A., Al-Hadeethi, Y., Ghasali, E., Raza, S., and Orooji, Y. (2024). Novel 2D MBenes-synthesis, structure, properties with excellent performance in energy conversion and storage: A review. *Materials Science and Engineering: R: Reports, 159*, 100796.

Khaledialidusti, R., Khazaei, M., Wang, V., Miao, N., Si, C., Wang, J., and Wang, J. (2021). Exploring structural, electronic, and mechanical properties of 2D hexagonal MBenes. *Journal of Physics: Condensed Matter, 33*(15), 155503.

Klimeš, J., Bowler, D. R., and Michaelides, A. (2010). Chemical accuracy for the van der Waals density functional. *Journal of Physics: Condensed Matter, 22*(2), 022201.

Kresse, G., and Furthmüller, J. (1996a). Efficiency of ab-initio total energy calculations for metals and semiconductors using a plane-wave basis set. *Computational Materials Science, 6*(1), 15-50.

Kresse, G., and Furthmüller, J. (1996b). Efficient iterative schemes for ab initio total-energy calculations using a plane-wave basis set. *Physical Review B, 54*(16), 11169-11186.

Li, B., Xu, H., Ma, Y., and Yang, S. (2019). Harnessing the unique properties of 2D materials for advanced lithium–sulfur batteries. *Nanoscale Horizons, 4*(1), 77-98.

Liu, Y., Cui, C., Liu, Y., Liu, W., and Wei, J. (2020). Application of MoS_2 in the cathode of lithium sulfur batteries. *RSC Advances, 10*(13), 7384-7395.

Liu, Y., Zhang, R., Wang, J., and Wang, Y. (2021). Current and future lithium-ion battery manufacturing. *iScience, 24*(4), 102332.

Manthiram, A., Chung, S.-H., and Zu, C. (2015). Lithium–Sulfur Batteries: Progress and Prospects. *Advanced Materials, 27*(12), 1980-2006.

Mou, Y., Wang, Y., Wan, J., Yao, G., Feng, C., Zhang, H., and Wang, Y. (2023). Rational design of 2D MBene-based bifunctional OER/ORR dual-metal atom catalysts: a DFT study. *Physical Chemistry Chemical Physics, 25*(42), 29135-29142.

Perdew, J. P., Burke, K., and Ernzerhof, M. (1996). Generalized Gradient Approximation Made Simple. *Physical Review Letters, 77*(18), 3865-3868.

Scheers, J., Fantini, S., and Johansson, P. (2014). A review of electrolytes for lithium–sulphur batteries. *Journal of Power Sources, 255*, 204-218.

Solaun, K., and Cerdá, E. (2019). Climate change impacts on renewable energy generation. A review of quantitative projections. *Renewable and Sustainable Energy Reviews, 116*, 109415.

Wang, J., Ye, T.-N., Gong, Y., Wu, J., Miao, N., Tada, T., and Hosono, H. (2019). Discovery of hexagonal ternary phase Ti_2InB_2 and its evolution to layered boride TiB. *Nature Communications, 10*(1), 2284.

Wang, T., Kretschmer, K., Choi, S., Pang, H., Xue, H., and Wang, G. (2017). Fabrication Methods of Porous Carbon Materials and Separator Membranes for Lithium–Sulfur Batteries: Development and Future Perspectives. *Small Methods, 1*(8), 1700089.

Wild, M., O'Neill, L., Zhang, T., Purkayastha, R., Minton, G., Marinescu, M., and Offer, G. J. (2015). Lithium sulfur batteries, a mechanistic review. *Energy & Environmental Science, 8*(12), 3477-3494.

Xiao, Y., Li, Y., Guo, Z., Tang, C., Sa, B., Miao, N., Zhou, J., and Sun, Z. (2021). Functionalized Mo2B2 MBenes: Promising anchoring and electrocatalysis materials for Lithium-Sulfur battery. *Applied Surface Science, 566*, 150634.

Xiao, Z., Li, Z., Meng, X., and Wang, R. (2019). MXene-engineered lithium–sulfur batteries. *Journal of Materials Chemistry A, 7*(40), 22730-22743.

Xiong, S., Xie, K., Diao, Y., and Hong, X. (2014). Characterization of the solid electrolyte interphase on lithium anode for preventing the shuttle mechanism in lithium–sulfur batteries. *Journal of Power Sources, 246*, 840-845.

Yang, T., Xia, J., Piao, Z., Yang, L., Zhang, S., Xing, Y., and Zhou, G. (2021). Graphene-Based Materials for Flexible Lithium–Sulfur Batteries. *ACS Nano, 15*(9), 13901-13923.

Zhang, D., Gu, R., Lan, F. Y., Guo, W. Y., Deng, C. W., Xu, Q. J., Li, H. X., and Min, Y. L. (2021). "Anchor-Turbo" Strategy for Constructing Ni–VO_2 Coating Layer to Achieve Wide Temperature and High-Performance Lithium–Sulfur Batteries. *ACS Sustainable Chemistry & Engineering, 9*(48), 16251-16261.

Zhang, D., Wang, S., Hu, R., Gu, J., Cui, Y., Li, B., Chen, W., Liu, C., Shang, J., and Yang, S. (2020). Catalytic Conversion of Polysulfides on Single Atom Zinc Implanted MXene toward High-Rate Lithium–Sulfur Batteries. *Advanced Functional Materials, 30*(30), 2002471.

Zhang, H., Xiang, H., Dai, F.-z., Zhang, Z., and Zhou, Y. (2018). First demonstration of possible two-dimensional MBene CrB derived from MAB phase Cr_2AlB_2. *Journal of Materials Science & Technology, 34*(11), 2022-2026.

Zhang, Y., Gao, Z., Song, N., He, J., and Li, X. (2018). Graphene and its derivatives in lithium–sulfur batteries. *Materials Today Energy, 9*, 319-335.

Zheng, M., Chi, Y., Hu, Q., Tang, H., Jiang, X., Zhang, L., Zhang, S., Pang, H., and Xu, Q. (2019). Carbon nanotube-based materials for lithium–sulfur batteries. *Journal of Materials Chemistry A, 7*(29), 17204-17241.

Zheng, Y., Zheng, S., Xue, H., and Pang, H. (2019). Metal–organic frameworks for lithium–sulfur batteries. *Journal of Materials Chemistry A, 7*(8), 3469-3491.

CHAPTER II

LITERATURE REVIEW

2.1 Overview of lithium-sulfur batteries (Li-S batteries)

Among next-generation rechargeable batteries, lithium-sulfur batteries (LSBs) stand out as promising candidates for energy storage technology, replacing Li-ion batteries. This is due to their high specific capacity of 1675 mA h g^{-1}, high energy density of 2600 Wh kg^{-1}, and low cost associated with the sulfur cathode (Wild et al., 2015). **Figure 2.1** presents the configuration of Li-S battery which mainly consists of Li metal anode and sulfur-based cathode supported by conductive materials. At the cathode, sulfur is most stable in the form of cyclo-octasulfur (S_8), a ring-structured molecule (S. S. Zhang et al., 2010).

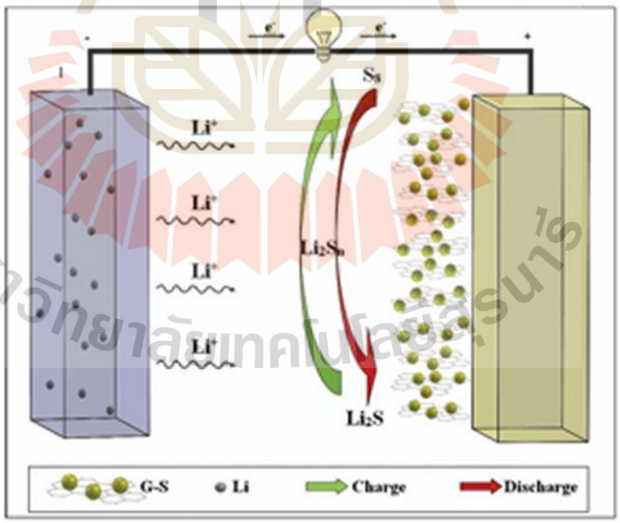

Figure 2.1 Schematic diagram of a Li-S battery configuration, featuring a graphene-sulfur composite as the cathode and lithium metal as the anode (Barghamadi et al., 2013).

The reaction mechanism of Li-S battery differs from that of Li-ion batteries which operate via an intercalation-deintercalation mechanism. The high specific capacity is produced from the redox reaction, known as sulfur reduction reaction (SRR). The overall reaction of this redox reaction:

$$16\ Li^+ + 16\ e^- + S_8 \rightleftharpoons 8Li_2S \qquad (2.1)$$

The conversion reaction between sulfur and Li_2S occurs as a multi-step electrochemical process with a potential of 2.15 V versus Li/Li (Ji et al., 2010). Charge-discharge voltage profiles and cyclic voltammograms (CV) have shown that the SRR generally involves two or three stages, depending on the reaction temperature and composition of the Li-S battery (Akridge et al., 2004; Barchasz et al., 2012). As shown in **Figure 2.2**. The first state involves the reduction of sulfur to higher order polysulfides at 2.4 V. These polysulfides tend to dissolve in electrolytes (D.-W. Wang et al., 2013):

$$S_8 + 2Li^+ + 2e^- \longrightarrow Li_2S_8 \qquad 2.39V \text{ vs. } Li^0/Li^+ \qquad (2.2)$$

$$3Li_2S_8 + 2Li^+ + 2e^- \longrightarrow 4Li_2S_6 \qquad 2.37V \text{ vs. } Li^0/Li^+ \qquad (2.3)$$

$$2Li_2S_6 + 2Li^+ + 2e^- \longrightarrow 3Li_2S_4 \qquad 2.24V \text{ vs. } Li^0/Li^+ \qquad (2.4)$$

During this stage, disproportionation of Li_2S_x can lead to the formation of shorter-chain Li_2S_y (where $y < x$). Additionally, Li_2S_8 dissolved in the electrolyte can undergo electrochemical reduction at the lithium metal anode (Nazar et al., 2014).

$$Li_2S_x \longrightarrow Li_2S_y + (x - y)S \qquad (2.5)$$

$$3Li_2S_8 + 2Li^+ + 2e^- \leftrightarrow 4Li_2S_6 \qquad (2.6)$$

Next stage, at low voltage (<2.1V), high-order polysulfides are further reduced to form low-order polysulfide. These low-order polysulfide, such as Li_2S_2 and Li_2S, precipitate as solid layers on the cathode surface, forming an insulating layer (S. S. Zhang, 2013):

$$Li_2S_4 + 2Li^+ + 2e^- \longrightarrow 2Li_2S_2 \qquad 2.20V \text{ vs } Li^0/Li^+ \qquad (2.7)$$

$$Li_2S_2 + 2Li^+ + 2e^- \longrightarrow 2Li_2S \qquad 2.15V \text{ vs } Li^0/Li^+ \qquad (2.8)$$

These stages explain the multi-stage reduction process in Li-S batteries. These transformations are essential for the battery's high capacity and performance.

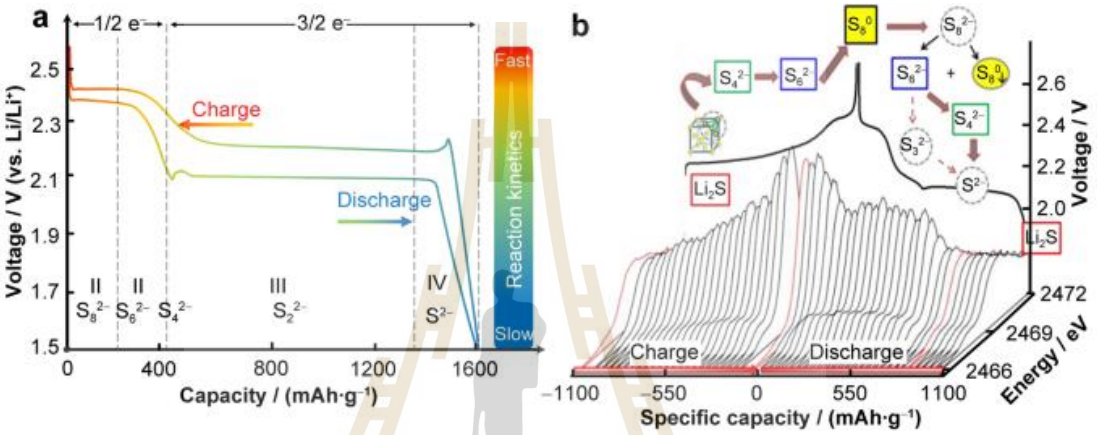

Figure 2.2 (a) Voltage profile and chemical reactions occurring at the sulfur cathode. (b) Sulfur K-edge XANES spectra and reference spectra illustrating changes in absorbance during electrochemical cycling, with charge and discharge endpoints indicated in red (Cuisinier et al., 2013).

Although Li-S batteries offer several advantages for high-performance batteries, they still face challenges due to the conversion reaction, which leads to low Coulombic efficiency and limited stability over repeated cycles. The challenges in Li-S batteries come from the cathode, anode, and electrolyte. The main challenges at cathode include LIPSs dissolution, low conductivity of S and Li_2S, and cathode volume change. In the case of polysulfide dissolution, high-order LiPSs, including Li_2S_8, Li_2S_6, and Li_2S_4, easily dissolve into electrolyte. Once dissolved, these polysulfides tend to diffuse from the cathode to the anode due to a concentration gradient and electric field, where they are reduced to short-chain LIPSs at the anode. This process is described by the following equations and summarize in **Figure 2.3**:

$$(n\text{-}1)Li_2S_x + 2Li^+ + 2e^- \longrightarrow nLi_2S_{x-1} \text{ an electrochemical reduction} \qquad (2.9)$$

This phenomenon, known as the "shuttle effect," leads to low Coulombic efficiency and self-discharge (Evers et al., 2013). Ether-based electrolytes typically facilitate the dissolution of high-order LiPSs (Shim et al., 2002).

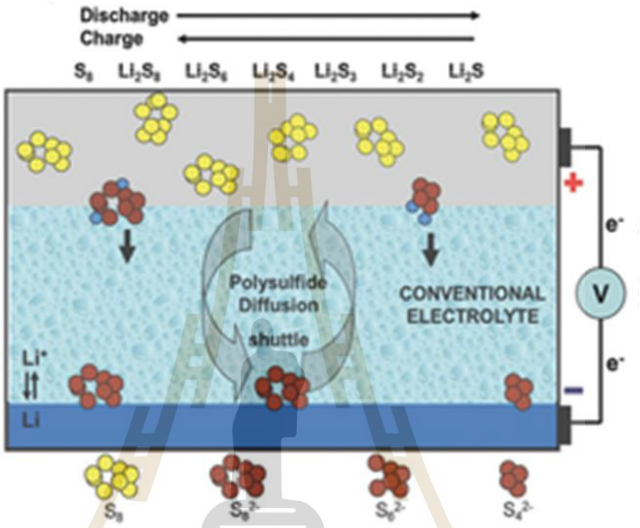

Figure 2.3 Scheme of polysulfide shuttle effect (R. Xu et al., 2013).

Besides the dissolution of LiPSs, the coverage of short-chain LiPSs on the cathode, including Li_2S_2 and Li_2S, results in low conductivity due to their non-conductive nature (Manthiram et al., 2015). However, it is difficult to convert Li_2S_2 and Li_2S back to other forms of LiPSs due to the high energy barrier for their decomposition. This results in sluggish kinetics and requires a high overpotential (Y. Yang et al., 2012). Another issue is the volumetric change during the SRR. The density difference between sulfur and Li_2S is approximately 80%, with sulfur at 2.03 g cm^{-3} and Li_2S at 1.66 g cm^{-3}. This extreme change led to polarization of cathode and loss effective contact between the active material and the collector (Song et al., 2016).

Regarding anode, the main problem is the poor stability of Li metal. Li can reduce electrolytes molecules, forming unstable solid-electrolyte interphase (SEI) layer. This can be explained by the Fermi energy of Li metal being higher than the unoccupied states of the electrolyte molecules (Aurbach et al., 2009), resulting in

capacity loss and reduced anode efficiency. Additionally, dendrite formation of Li metal can occur alongside LiPSs deposits on the anode surface. Lithium dendrites can pierce the separator, which may lead to short-circuit (X. Xu et al., 2017). LiPSs can irreversibly react with lithium metal to form a non-conductive Li_2S passivation layer in anode site, leading to reduced performance of anode site.

Another issue is electrolyte depletion. Some electrolytes react strongly with high order polysulfides, while more stable electrolytes gradually deplete over time due to reactions with polysulfides and Li metal (Cuisinier et al., 2015). An example of this degradation mechanism can be observed in ether solvents, such as dimethoxymethane (DME) and dioxolane (DOL), as shown below (S. S. Zhang, 2013):

$$R\text{–}O\text{–}R + Li_2S_n \longrightarrow R\text{–}OLi + R\text{-}S_nLi \quad (2.10)$$

$$R\text{–}O\text{–}R + Li_2 \longrightarrow 2R\text{–}OLi + R\text{-}R^+ \quad (2.11)$$

Overall, the problems were summarized in **Figure 2.4**. These challenges still need to be overcome and alleviated to promote and develop high-performance lithium-sulfur batteries.

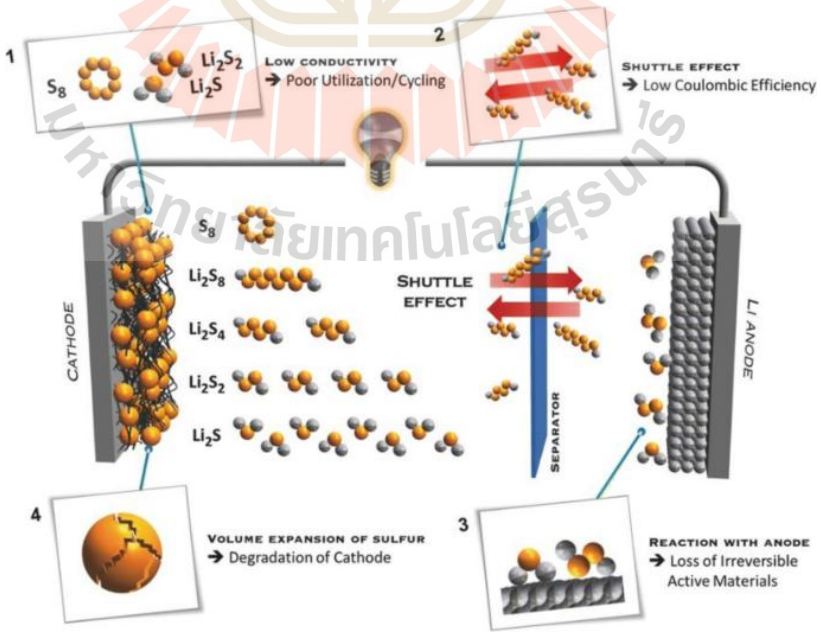

Figure 2.4 Problems during the charge and discharge process of Li-S batteries (L. Yang et al., 2020).

2.2 Study sulfur reduction reaction and sulfur evolution reaction

The processes occurring on cathode side of Li-S batteries involve conversion between S_8 to Li_2S. During discharge, Li ions and electrons from anode transfer to cathode, where they react with S_8 in a process called the sulfur reduction reaction (SRR). During charging, oxidation occurs in a process known as the sulfur evolution reaction (SER). Li-S bond in Li_2S break to convert back to S_8 (D. Liu et al., 2018). These reactions involve transfer of 16 electrons. Nevertheless, the study of these reactions remains challenging due to the lack of effective methods to identify polysulfide intermediates and conversion step. Additionally, determining theoretical equilibrium potential for simulating SRR and SER is difficult. Therefore, the design of electrocatalysts that accelerate SRR and SER remains challenging for computational studies.

For SRR, previous research has proposed many intermediates of polysulfides, suggested through both experimental and computational methods. The current understanding, commonly used in the computational studies, focuses on the thermodynamic conversion of polysulfides, including Li_2S_x (x = 8, 6, 4, 2, 1) (Zhou et al., 2020). The elementary steps in this understanding are represented by Equations (2.12) -(2.16):

$$S_8^* + 2Li^+ + 2e^- \rightarrow Li_2S_8^* \quad (2.12)$$

$$Li_2S_8^* \rightarrow Li_2S_6^* + \frac{1}{4} S_8 \quad (2.13)$$

$$Li_2S_6^* \rightarrow Li_2S_4^* + \frac{1}{4} S_8 \quad (2.14)$$

$$Li_2S_4^* \rightarrow Li_2S_2^* + \frac{1}{4} S_8 \quad (2.15)$$

$$Li_2S_2^* \rightarrow Li_2S^* + \frac{1}{4} S_8 \quad (2.16)$$

These equations exhibit conversion of polysulfides through decomposition of S_8 to Li_2S by breaking S-S bonds. The potential limiting step of these calculations is usually suggested to be the conversion between Li_2S_4 and Li_2S, as shown in **Figure 2.5**. These steps show a critical challenge like those observed in experiments. If catalytic material can lower the energy barrier of the potential limiting step, it is considered a

promising candidate for use as a cathode material in Li-S batteries. Consequently, this proposition of the mechanism has been used in many computational studies. Nevertheless, these equations propose the conversion of LiPSs without accounting for the contributions of electrons and lithium ions. These differ from the mechanism in which S_8 is converted into smaller molecules by reacting with lithium ions and electrons transferred from the anode.

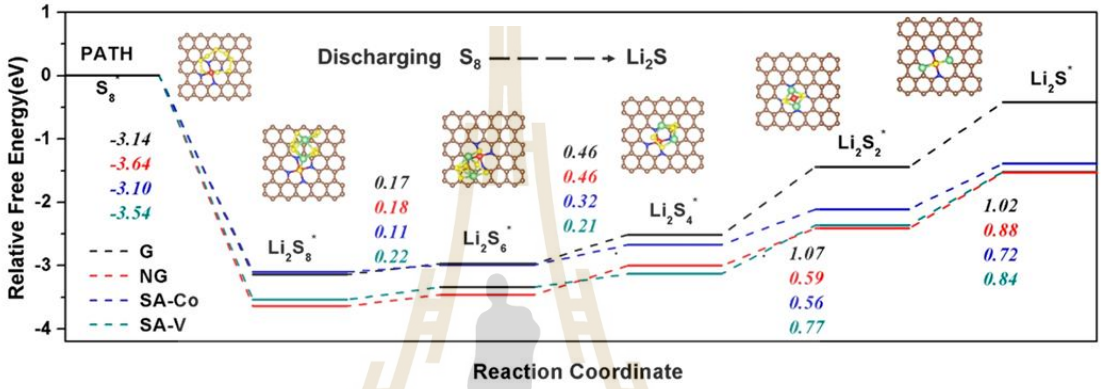

Figure 2.5 Energy profile for the reduction of polysulfides on TM@NG, excluding the contributions of electrons and lithium ions (Zhou et al., 2020).

To refine the equations used to explain SRR in computational simulations, researchers have attempted to include the contribution of electrons in Gibbs free energy calculations, analogous to the ORR and OER processes(Nørskov et al., 2004). As shown in Equations (2.17)-(2.22), this mechanism consists five electron-transfer step and one non-electron-transfer step (Z. Du et al., 2019; R. Wang et al., 2020)

$$S_8 + 2\,Li^+ + 2\,e^- + * \rightarrow Li_2S_8^* \tag{2.17}$$

$$Li_2S_8^* + \frac{2}{3}Li^+ + \frac{2}{3}e^- + \frac{1}{3}* \rightarrow \frac{4}{3}Li_2S_6^* \tag{2.18}$$

$$\frac{4}{3}Li_2S_6^* + \frac{4}{3}Li^+ + \frac{4}{3}e^- + \frac{2}{3}* \rightarrow 2Li_2S_4^* \tag{2.19}$$

$$2Li_2S_4^* + 4Li^+ + 4e^- + 2* \rightarrow 4Li_2S_2^* \tag{2.20}$$

$$2Li_2S_2^* + 8Li^+ + 8e^- + 4* \rightarrow 4Li_2S^* \tag{2.21}$$

$$2Li_2S^* \rightarrow 4Li_2S + 8* \quad (2.22)$$

Because these equations consider electrons transfer, the overpotential of the SRR can be calculate based on ORR, as shown in Equation (2.23):

$$\eta_{SRR} = U_{eq} - \min\left[\frac{\Delta G_{0,i}}{ne}\right] \quad (2.23)$$

where $\Delta G_{0,i}$ represents the Gibbs free energy change of each elementary step, and ne denotes the number of electrons transferred in each step. The case of U_{eq} which are theoretical equilibrium potential usually involves two potentials. First, it can be calculated based on the standard free energy of Li_2S formation, as defined by Equation (2.24):

$$\Delta G_f^0 = 8G(Li_2S_{bulk})^0 - 8(S_8)^0 - 16G(Li_{atom})^0 \quad (2.24)$$

The equilibrium potential of the 16e⁻ SRR is derived as ΔG_f^0/16e⁻ which is usually 2.02 V. The free energy diagram, including the overpotential based on this understanding, is shown in **Figure 2.6**. Alternatively, the theoretical equilibrium potential can also be referenced from the average cell voltage of Li-S batteries, which is approximately 2.15 V (Akridge et al., 2004; Evers et al., 2012). Both calculations still suggest that the potential limiting step is conversion from Li_2S_4 to Li_2S.

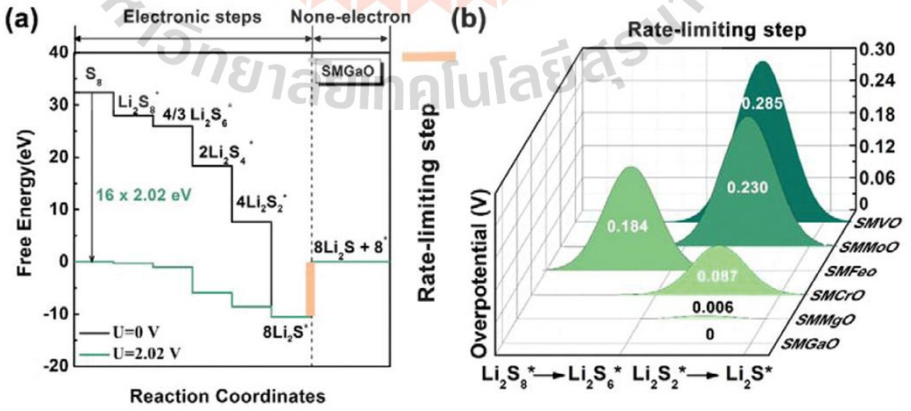

Figure 2.6 Energy profile for the reduction of polysulfides and overpotential of rate-limiting step (L. Wang et al., 2022).

During the charging process, SER involves the conversion of Li_2S in solid state back to S_8. This occurs through the breaking of Li–S bonds, releasing Li atoms into the electrolyte (Arneson et al., 2018; S. Li et al., 2020; Li et al., 2016; L. Wang et al., 2015; Liang Zhang et al., 2017), as shown in Equation (2.25):

$$Li_2S \rightarrow S^{2-} + 2Li^+ + 2e^- \quad (2.25)$$

Nevertheless, the SER still faces sluggish kinetics during the charging process due to the challenging decomposition of Li_2S, which requires a high energy barrier to break the Li–S bonds. Consequently, computational studies focus on this step to represent the overall SER by reducing the energy barrier to accelerate SER. The model of the decomposition process considers the conversion of Li_2S into LiS clusters and single Li ion. Li ion diffuses from the LiS cluster, representing Li diffusion after Li–S bond breaking. The energy barrier for Li-S bond breaking was calculated by CI-NEB method. An example of this study is shown in **Figure 2.7**.

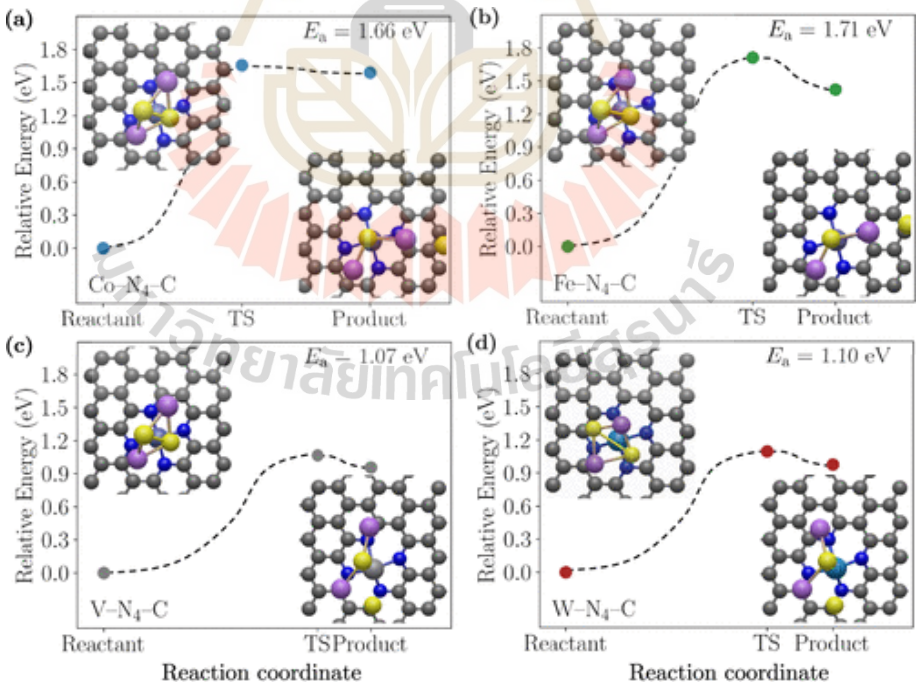

Figure 2.7 Energy barrier graphs for Li_2S decomposition with configuration of TM-N_4-C (Andritsos et al., 2021).

2.3 Developing cathode materials to address challenges.

Among the components of Li-S batteries, the cathode materials play a critical role in determining the energy density and power density of Li-S batteries. However, S_8 cannot be directly used in the cathode because it is an insulator for both electron and ion conduction. To address this, S_8 needs to be coated or combined with conductive materials to facilitate electron transfer and enable the efficient conversion of LiPSs.

In the early stages of cathode development, researchers often combined S_8 with various carbon-based materials, such as porous carbon, graphene, and carbon nanotubes (Ren et al., 2019; Z. Xu et al., 2020). The carbon materials provide excellent electron and ion transport for non-conductive sulfur and alleviate the problem from volume change of sulfur. However, while simple carbon materials can initially improve conductivity, they also lead to a reduction in the energy density of the electrode (Bhargav et al., 2020). Furthermore, as discussed in Section 2.1, the cathode faces several challenges, including the shuttle effect and the insulating nature of Li_2S. To overcome these issues, researchers have developed new strategies to improve cathode performance. Key strategies include structure engineering, crystal structure engineering, and electronic structure engineering.

In context of structure and crystal engineering, researchers have explored various dimensional structures, ranging from 0D to 3D, using synthesized or biomimetic materials. They have also investigated the effects of crystal facets and phases on material performance. Another widely studied approach, both experimentally and computationally, is electronic structure engineering. This strategy focuses on modifying the electronic structure of materials, which influences bonding strength with LiPSs and enhances catalytic activity, with their partially filled *d*-orbitals, playing a crucial role in LiPSs adsorption and SRR. The goal is to adjust the energy level of the d-state to align more closely with the orbital energy levels of the sulfur host (T. Wang et al., 2021). For example, Zhang et al. compared the performance of Ni_2P with and without alloying cobalt. Their study suggested that the Co 3*d* energy band had a lower filling fraction and higher center than Ni 3*d*, resulting in stronger LiPSs adsorption. Alloying cobalt also

reduced the activation energy for the conversion of LiPSs, as shown in **Figure 2.8** (Shen et al., 2020).

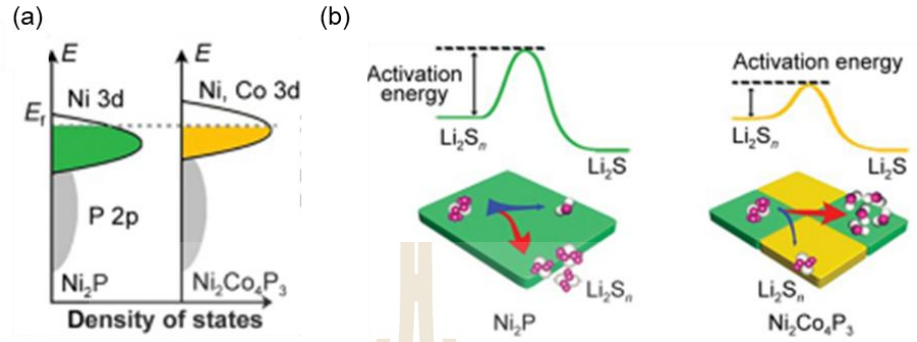

Figure 2.8 (a) Density of states for Ni and Co phosphides showing d-band shift caused by Co doping, where E_f represents Fermi energy level. (b) Change in activation energy for Li_2S nucleation when using Ni_2P and $Ni_2Co_4P_3$ as cathode materials (Shen et al., 2020).

The second strategy involves interface electronic structure engineering, or heterostructure development. This method combines the advantages of two components and modifies the electronic structure at the interface, leading to faster electron transfer and improved chemisorption. These benefits enhance the adsorption and conversion of polysulfides (J. Zhang et al., 2019; Zuo et al., 2022). For example, Chen's research suggests that $ZnFe_2O_4$–Ni_5P_4 Mott–Schottky heterojunction material significantly improves sulfur cathode performance. The side of $ZnFe_2O_4$ provides strong polysulfide adsorption, while Ni_5P_4 exhibits excellent catalytic properties (D. Zhang et al., 2022).

The latest method is single-atom catalyst engineering, which utilizes the unique electronic properties and coordinated environment of single atoms doped into supporting materials. For example, Zhang et al.'s work suggested that Fe single atoms enhance binding with sulfur atoms and improve electron transfer, alleviating the shuttle effect (G. Liu et al., 2022). Different single-atom metals exhibit distinct properties that influence LiPSs adsorption and the catalytic activity of SRR. Therefore,

the design and study of single-atom catalysts offers a promising direction for improving lithium–sulfur batteries.

2.4 Mo_2B_2-based MBene with oxygen functionalization

Currently, the development and discovery of two-dimensional (2D) materials are one of major goals in both experimental and computational research. Among these materials, MBenes is an intriguing new material used in energy applications and electrocatalysis due to their diverse electrical, mechanical, and magnetic properties. MBenes were first reported in 2015 by Ade and Hillebrecht (Ade et al., 2015). Successfully synthesized crystalline structures include orthorhombic and hexagonal MBenes, which are typically produced through exfoliation or etching techniques from MAB phases(Majed et al., 2023), a family of three-dimensional (3D) structures. The primary approach to MBene synthesis involves using MAB phases with acidic (HCl/LiF) or basic (NaOH) aqueous solutions to remove A layer. A second approach used the defragmentation of bulk powders into nanostructures. Additionally, MBenes can be synthesized through physical vapor deposition (PVD)(Sahu et al., 2021), chemical vapor deposition (CVD) method(Z. Zhang et al., 2024), and Molten Salt Method(Jothi et al., 2018). MAB phases show distinct structural formulas, including MAB (414 phases with Immm crystal symmetry), M_2AB_2 (212 phases with Cmmm crystal symmetry), M_3AB_4 (314 phase with Pmmm symmetry), and M_4AB_6 (416 phase with Cmmm crystal symmetry), where M represents transition metals and A represents atoms from IIA and IVA group(Ade et al., 2015), as shown in **Figure 2.9.** In MAB phases, M–A bonds are primarily metallic, while M–B bonds exhibit a mix of covalent, metallic, and ionic character due to the metalloid nature of boron (2.04 on the Pauling scale).

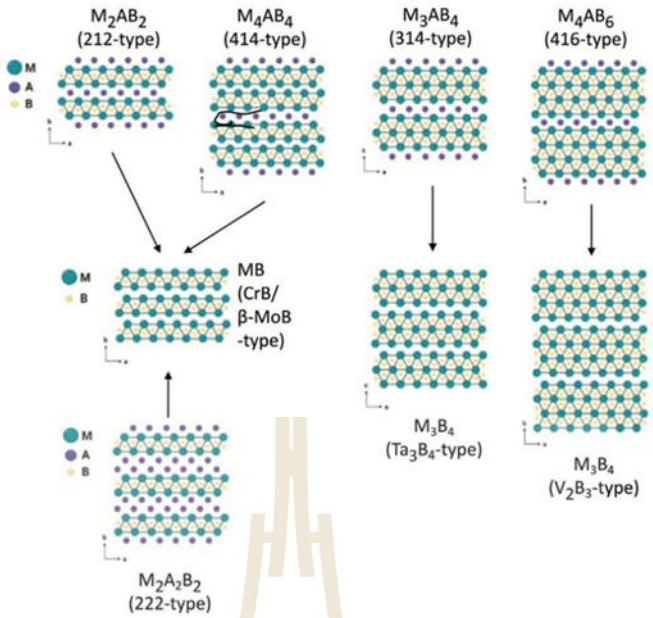

Figure 2.9 Structure and classification of MAB and related MBene phases by their crystal structures (Music et al., 2007).

Among 2D MBene materials, molybdenum-based borides have promising properties, including low cost, easy synthesis, high stability, and potential as alternative to metal catalysts(Park et al., 2017; Y. Wang et al., 2020). The known crystal structures include **α**-MoB, Mo_2B, **β**-MoB, **α**-MoB_2, **β**-MoB_2, Mo_2B_4, and Mo_2B_5(Rout et al., 2024). MoB and Mo_2B_2 are well-studied members of the MBene family and are typically synthesized by selectively etching aluminum layers from MoAlB. The crystal structure of these phases is shown in **Figure 2.10**.

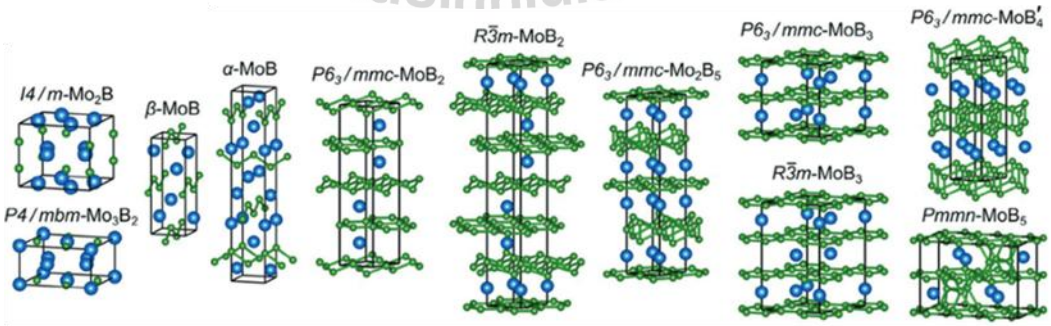

Figure 2.10 The crystal structures of Mo-B phases obtained through an evolutionary crystal structure search (Rybkovskiy et al., 2020).

The Mo_2B_2 structure is synthesized by selectively removing the middle aluminum (Al) layer from MoAlB through chemical etching with NaOH. Their 3D structure, MoAlB, belongs to a class of layered ternary borides that are structurally similar to MAX phases. Mo_2B_2 possesses noteworthy properties, including high flexural and compressive strength, oxidation resistance, metallic conductivity, and excellent thermal conductivity (Ali et al., 2017; Kota et al., 2016). Additionally, when used as an anode in Li-ion batteries, it shows high theoretical gravimetric capacities of 444 mAh/g (Guo et al., 2017). Mo_2B exhibits three stable phases that include orthorhombic, hexagonal, and tetragonal structures. Although Mo_2B_2 can be synthesized through etching, obtaining pure Mo_2B_2 is challenging due to the functional groups (F, O, and OH) that form on the surface during the etching process, depending on the etching solution. However, these functional groups significantly enhance the stability and catalytic activity of Mo_2B_2. (S. Liu et al., 2023). From previous research, they evaluated the advantage of functional group on surface (MoBX; X = O, S, Se, and Te) as anode for Na and K ion batteries. They wrote that the presence of functional groups on surface could facilitate ion diffusion by reducing energy barrier, leading to improved battery capacity. Moreover, their results on Young's modulus and Poisson's ratio of MoB and MoBX suggest that surface functionalization improves in-plane stiffness, which helps reduce electrode cracking and pulverization issues, ultimately enhancing stability. (K. Liu et al., 2021). When used as cathode material in Li-S batteries, functionalized Mo_2B_2 has shown promising results. Xiao and colleagues studied Mo_2B_2 functionalized with surface groups such as O and F and found that these functional groups improve the material's anchoring performance, helping to suppress the shuttle effect in Li-S batteries. Their calculations also suggest that surface functionalization reduces the diffusion and decomposition barriers of Li_2S. Among the materials in this work, $Mo_2B_2O_2$ exhibit superior performance compared to $Mo_2B_2F_2$, making it a more suitable cathode material for Li-S batteries (Xiao et al., 2021).

2.5 Single-atom catalysts

Single-atom catalysts (SACs) are among the most promising strategies for improving performance of heterogeneous catalysts by maximizing atomic utilization. Research into SACSs began in the 1990s (L. Li et al., 2020). These catalysts are created by reducing metal particles or bulk materials down to single atoms (A. Wang et al., 2018), as shown in **Figure 2.11**.

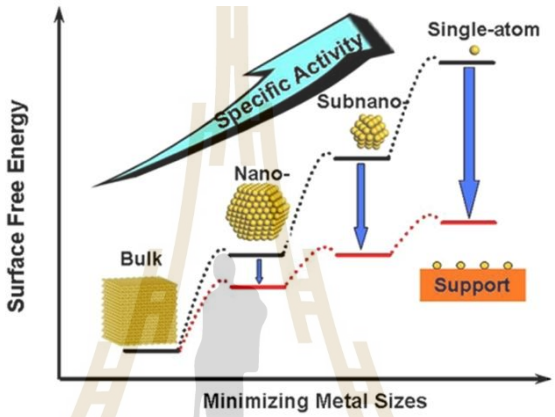

Figure 2.11 Schematics illustrating the variation in surface free energy and specific activity per metal atom as a function of metal particle size, along with the role of support in stabilizing single atoms (X.-F. Yang et al., 2013).

SACs of then exhibit superior catalytic activity compared to nanoparticles, bulk materials, and traditional heterogenous catalysts attributed to factors such as increased surface free energy, quantum size effects, unsaturated coordination environments, and strong metal–support interactions. Nevertheless, maintaining the isolation of single atoms is challenging due to their aggregation. The stability of these isolated atoms is influenced by factors including the reducibility of the support material, reaction temperature, and partial pressure.

Selecting an appropriate support material is crucial for stabilizing single atoms. Reducible supported are effective in maintaining isolated atoms, whereas non-reducible supported may lead to aggregation into nanoparticles. This phenomenon was shown in **Figure 2.12**, which compares the effects of reducible and non-reducible

transition metal oxide supports. However, reaction conditions significantly impact the formation and stability of isolated atoms (DeRita et al., 2019).

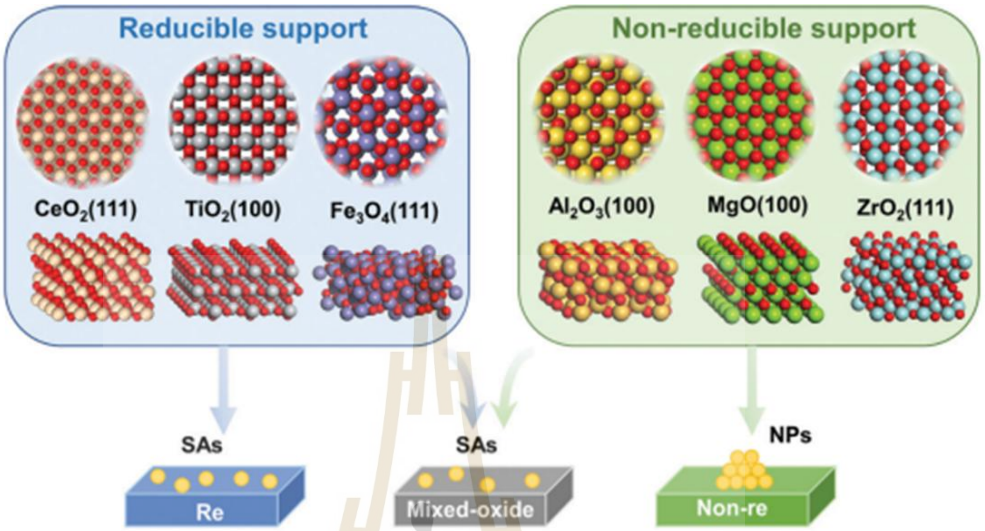

Figure 2.12 Illustration of the structure of the reducible support, non-reducible support and metal NPs sintering/dispersing on different supports (L. Li et al., 2020).

To prevent agglomeration into clusters or particles, careful consideration of synthetic methods is essential. Currently, there are four primary methods for synthesizing SACs: pyrolysis, atomic layer deposition (ALD)/chemical vapor deposition (CVD), ball milling, and solution-based chemistry. Each method offers different advantages. Pyrolysis method allows control over loading amounts by utilizing high temperature and an inert atmosphere (Pei et al., 2015). Atomic layer deposition (ALD) and Chemical Vapor Deposition (CVD) method enable atomic-level control and high purity of single atoms (Qu et al., 2018; Lei Zhang et al., 2018). Ball milling and solution-based chemistry method are rapid, cost-effective methods for producing single atoms (Bi et al., 2018; Deng et al., 2015). It's important to note that not all methods are suitable for producing SACs. Careful selection of the synthesis method is essential to ensure the purity and isolation of single atoms.

Due to their excellent electrical conductivity, combined with catalytic activity and selectivity, SACs are promising materials for addressing challenges in Li-S batteries, including those related to the cathode, anode, and separator. SACs show great

potential for enhancing the reaction kinetics of LiPSs conversion and mitigating the shuttle effect (Mikhaylik et al., 2004). In the development of cathode materials, a key strategy to alleviate the shuttle effect involves increasing chemical adsorption of LiPSs. Beyond strong adsorption, cathode materials must also promote the efficient conversion of LiPSs. The use of SACs was first reported by Yang and co-workers, who studied Fe–N doped carbon (Fe–NC) as a cathode material (Z. Liu et al., 2018). In this configuration, iron atoms serve as single-atom catalysts, forming strong interactions with LiPSs through sulfur–iron bonds, thereby accelerating redox reactions during charge and discharge cycles. The Fe-NC cathode showed enhanced cycle stability, maintaining a capacity of 427 mAh g^{-1} after 300 cycles, effectively alleviating the shuttle effect and preserving coulombic efficiency. Ji and co-workers extended this approach by synthesizing Co–N doped graphene (Co–NG) materials through pyrolysis (Zhenzhen Du et al., 2019). Experimental results indicated that Co–NG exhibited performance comparable to Fe–NC. Density functional theory (DFT) calculations suggested several advantages of cobalt doping in graphene. Co doping increased the density of states at the Fermi level, resulting in higher electrical conductivity. The energy barrier for Li2S oxidation was lowered, improving oxidation kinetics when doping with Co. Additionally, the potential-limiting step in the conversion from Li_2S_2 to LiS was accelerated. Stronger Co–S bonds enhanced adsorption energy, leading to more effective LiPS trapping. These studies highlight the potential of SACs in advancing cathode materials for Li–S batteries. However, the performance of SACs varies with the type of single atom used, making the design and selection of single atom doping a critical research focus.

For example, Cui and colleagues studied eight types of metal–nitrogen-doped graphene (M–NG, where M = Fe, Mn, Ru, Zn, Co, Cu, V, and Ag) using DFT calculations (Zhou et al., 2020), as show in **Figure 2.13**. They screened the best M-NG materials by studying the decomposition energy of Li_2S and the stability of M-NG structures. Among these materials, vanadium with nitrogen doped graphene (V–NG) exhibited the lowest energy barrier for Li_2S decomposition and the highest LiPS binding energy, effectively suppressing the shuttle effect. When synthesized, V–NG achieved an initial specific capacity of mAh g^{-1} at 0.5C. Based on these findings, high-performance cathode

materials should meet three critical criteria, including strong LiPS trapping, effective deposition sites, and accelerated LiPS conversion. Consequently, the study of SACs through experimental, computational, or combined method represents a promising pathway for solving the challenges faced by Li–S batteries.

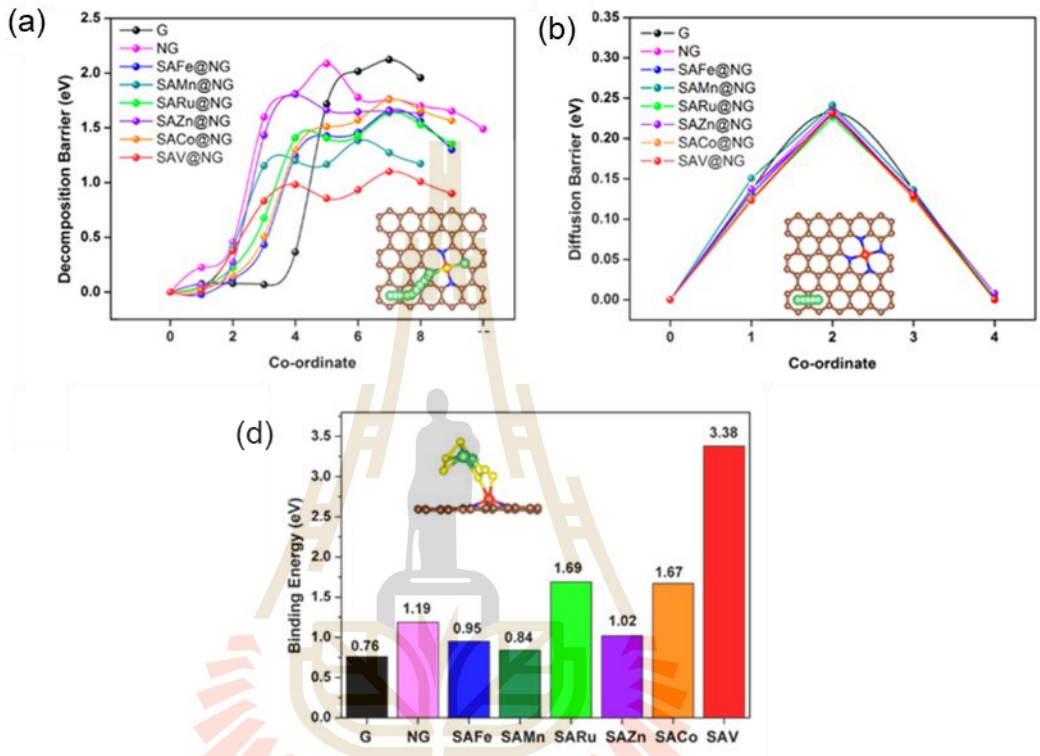

Figure 2.13 (a) Decomposition barriers of Li_2S and (b) Li-ion diffusion barriers of different SA-NG. (c) Li_2S_6 binding energy of each SA-NG (Zhou et al., 2020).

As mentioned above, SACs play a crucial role in enhancing the adsorption and catalytic activity of materials. Consequently, combining SACs with MBenes represents a promising direction for development. Recent studies have shown increasing interest in SACs supported on MBenes for various energy devices, attributed to the high conductivity and catalytic activity of both the single atom site and the MBene support.(Shukla, 2024; E. Wang et al., 2022; Yao et al., 2020). Moreover, these materials have shown significant potential as electrodes for reactions such as the oxygen reduction reaction (ORR)(E. Wang et al., 2022; T. Zhang et al., 2021) hydrogen reduction reaction (HER) (B. Li et al., 2020), and nitrogen reduction reaction (NRR) (Yao et al., 2020). Interestingly, even when using the same transition metal, the optimal single

atom can vary depending on the type of MBene used. For instance, Li and co-workers studied single metal atoms supported on $W_2B_2O_2$ (SA-$W_2B_2O_2$) and compared them to those supported on $Mo_2B_2O_2$ (SA-$Mo_2B_2O_2$) for HER. Their findings suggested significant differences in HER activity between SA-$W_2B_2O_2$ and SA-$Mo_2B_2O_2$, even with the same single metal atom (B. Li et al., 2020). As shown in **Figure 2.14,** SA-$W_2B_2O_2$ outperformed SA-$Mo_2B_2O_2$, particularly for V and Zn single atoms. These results highlight that the choice of MBene affects the selection of the optimal single atom, emphasizing the importance of finding the right SA-MBene combination for achieving the best performance.

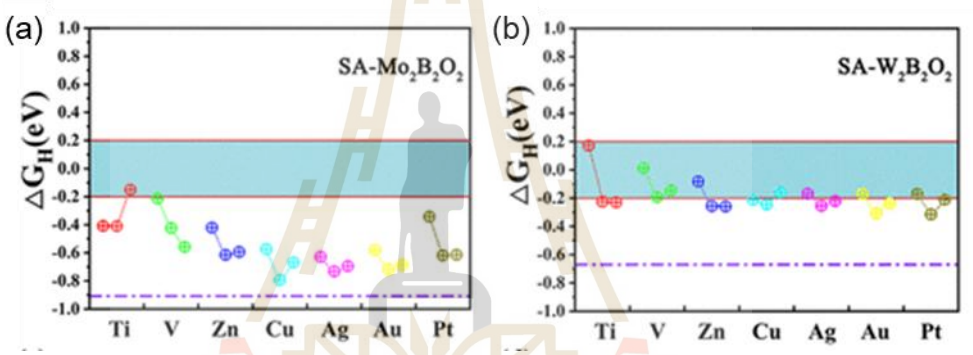

Figure 2.14 (a) Gibbs free energy for HER after introducing different metal single atoms on $Mo_2B_2O_2$ and $W_2B_2O_2$, respectively (B. Li et al., 2020).

In this thesis, we focused on SA-$Mo_2B_2O_2$ as a cathode material for Li-S batteries. This choice is particularly interesting because these materials have not yet been extensively studied in this application. Furthermore, the ideal single atom for optimizing both adsorption and catalytic activity on $Mo_2B_2O_2$ remains unknown. However, previous research provides valuable insights into the suitable sites for single atom decoration. As shown in **Figure 2.15**, the optimal site for single-atom decoration is the hollow site, where the single atom binds with four oxygen atoms (S_0). This knowledge serves as a foundation for our study.

Given the unique potential of SACs and MBenes, further research into their combinations could open new opportunities for advancing energy storage and conversion technologies. Specifically, exploring the interactions between different

single atoms and MBenes across a variety of reactions and applications may provide critical insights for the design of next-generation materials.

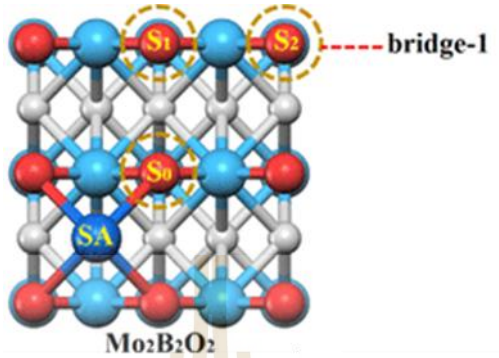

Figure 2.15 Schematic representation of suitable configuration SA decorated on $Mo_2B_2O_2$ (B. Li et al., 2020).

2.5 References

Ade, M., and Hillebrecht, H. (2015). Ternary Borides Cr_2AlB_2, Cr_3AlB_4, and Cr_4AlB_6: The First Members of the Series $(CrB_2)_nCrAl$ with n = 1, 2, 3 and a Unifying Concept for Ternary Borides as MAB-Phases. *Inorganic Chemistry, 54*(13), 6122-6135.

Akridge, J. R., Mikhaylik, Y. V., and White, N. (2004). Li/S fundamental chemistry and application to high-performance rechargeable batteries. *Solid State Ionics, 175*(1), 243-245.

Ali, M. A., Hadi, M. A., Hossain, M. M., Naqib, S. H., and Islam, A. K. M. A. (2017). Theoretical investigation of structural, elastic, and electronic properties of ternary boride MoAlB. *physica status solidi (b), 254*(7), 1700010.

Andritsos, E. I., Lekakou, C., and Cai, Q. (2021). Single-Atom Catalysts as Promising Cathode Materials for Lithium–Sulfur Batteries. *The Journal of Physical Chemistry C, 125*(33), 18108-18118.

Arneson, C., Wawrzyniakowski, Z. D., Postlewaite, J. T., and Ma, Y. (2018). Lithiation and Delithiation Processes in Lithium–Sulfur Batteries from Ab Initio Molecular Dynamics Simulations. *The Journal of Physical Chemistry C, 122*(16), 8769-8779.

Aurbach, D., Pollak, E., Elazari, R., Salitra, G., Kelley, C. S., and Affinito, J. (2009). On the Surface Chemical Aspects of Very High Energy Density, Rechargeable Li–Sulfur Batteries. *Journal of The Electrochemical Society, 156*(8), A694.

Barchasz, C., Molton, F., Duboc, C., Leprêtre, J.-C., Patoux, S., and Alloin, F. (2012). Lithium/Sulfur Cell Discharge Mechanism: An Original Approach for Intermediate Species Identification. *Analytical Chemistry, 84*(9), 3973-3980.

Barghamadi, M., Kapoor, A., and Wen, C. (2013). A Review on Li-S Batteries as a High Efficiency Rechargeable Lithium Battery. *Journal of The Electrochemical Society, 160*(8), A1256.

Bhargav, A., He, J., Gupta, A., and Manthiram, A. (2020). Lithium-Sulfur Batteries: Attaining the Critical Metrics. *Joule, 4*(2), 285-291.

Bi, W., Li, X., You, R., Chen, M., Yuan, R., Huang, W., Wu, X., Chu, W., Wu, C., and Xie, Y. (2018). Surface Immobilization of Transition Metal Ions on Nitrogen-Doped Graphene Realizing High-Efficient and Selective CO_2 Reduction. *Advanced Materials, 30*(18), 1706617.

Cuisinier, M., Cabelguen, P.-E., Evers, S., He, G., Kolbeck, M., Garsuch, A., Bolin, T., Balasubramanian, M., and Nazar, L. F. (2013). Sulfur Speciation in Li–S Batteries Determined by Operando X-ray Absorption Spectroscopy. *The Journal of Physical Chemistry Letters, 4*(19), 3227-3232.

Cuisinier, M., Hart, C., Balasubramanian, M., Garsuch, A., and Nazar, L. F. (2015). Radical or Not Radical: Revisiting Lithium–Sulfur Electrochemistry in Nonaqueous Electrolytes. *Advanced Energy Materials, 5*(16), 1401801.

Deng, D., Chen, X., Yu, L., Wu, X., Liu, Q., Liu, Y., Yang, H., Tian, H., Hu, Y., Du, P., Si, R., Wang, J., Cui, X., Li, H., Xiao, J., Xu, T., Deng, J., Yang, F., Duchesne, P. N., Zhang, P., Zhou, J., Sun, L., Li, J., Pan, X., and Bao, X. (2015). A single iron site confined in a graphene matrix for the catalytic oxidation of benzene at room temperature. *Science Advances, 1*(11), e1500462.

DeRita, L., Resasco, J., Dai, S., Boubnov, A., Thang, H. V., Hoffman, A. S., Ro, I., Graham, G. W., Bare, S. R., Pacchioni, G., Pan, X., and Christopher, P. (2019). Structural evolution of atomically dispersed Pt catalysts dictates reactivity. *Nat Mater, 18*(7), 746-751.

Du, Z., Chen, X., Hu, W., Chuang, C., Xie, S., Hu, A., Yan, W., Kong, X., Wu, X., Ji, H., and Wan, L.-J. (2019). Cobalt in Nitrogen-Doped Graphene as Single-Atom Catalyst for High-Sulfur Content Lithium–Sulfur Batteries. *Journal of the American Chemical Society, 141*(9), 3977-3985.

Du, Z., Chen, X., Hu, W., Chuang, C., Xie, S., Hu, A., Yan, W., Kong, X., Wu, X., Ji, H., and Wan, L. J. (2019). Cobalt in Nitrogen-Doped Graphene as Single-Atom Catalyst for High-Sulfur Content Lithium-Sulfur Batteries. *J Am Chem Soc, 141*(9), 3977-3985.

Evers, S., and Nazar, L. F. (2013). New Approaches for High Energy Density Lithium–Sulfur Battery Cathodes. *Accounts of Chemical Research, 46*(5), 1135-1143.

Evers, S., Yim, T., and Nazar, L. F. (2012). Understanding the Nature of Absorption/Adsorption in Nanoporous Polysulfide Sorbents for the Li–S Battery. *The Journal of Physical Chemistry C, 116*(37), 19653-19658.

Guo, Z., Zhou, J., and Sun, Z. (2017). New two-dimensional transition metal borides for Li ion batteries and electrocatalysis. *Journal of Materials Chemistry A, 5*(45), 23530-23535.

Ji, X., and Nazar, L. F. (2010). Advances in Li–S batteries. *Journal of Materials Chemistry, 20*(44), 9821-9826.

Jothi, P. R., Yubuta, K., and Fokwa, B. P. T. (2018). A Simple, General Synthetic Route toward Nanoscale Transition Metal Borides. *Advanced Materials, 30*(14), 1704181.

Kota, S., Zapata-Solvas, E., Ly, A., Lu, J., Elkassabany, O., Huon, A., Lee, W. E., Hultman, L., May, S. J., and Barsoum, M. W. (2016). Synthesis and Characterization of an Alumina Forming Nanolaminated Boride: MoAlB. *Sci Rep, 6*, 26475.

Li, B., Wu, Y., Li, N., Chen, X., Zeng, X., Arramel, Zhao, X., and Jiang, J. (2020). Single-Metal Atoms Supported on MBenes for Robust Electrochemical Hydrogen Evolution. *ACS Applied Materials & Interfaces, 12*(8), 9261-9267.

Li, L., Chang, X., Lin, X., Zhao, Z.-J., and Gong, J. (2020). Theoretical insights into single-atom catalysts. *Chemical Society Reviews, 49*(22), 8156-8178.

Li, S., Leng, D., Li, W., Qie, L., Dong, Z., Cheng, Z., and Fan, Z. (2020). Recent progress in developing Li2S cathodes for Li–S batteries. *Energy Storage Materials, 27*, 279-296.

Li, X., Zai, J., Xiang, S., Liu, Y., He, X., Xu, Z., Wang, K., Ma, Z., and Qian, X. (2016). Regeneration of Metal Sulfides in the Delithiation Process: The Key to Cyclic Stability. *Advanced Energy Materials, 6*(19), 1601056.

Liu, D., Zhang, C., Zhou, G., Lv, W., Ling, G., Zhi, L., and Yang, Q.-H. (2018). Catalytic Effects in Lithium–Sulfur Batteries: Promoted Sulfur Transformation and Reduced Shuttle Effect. *Advanced Science, 5*(1), 1700270.

Liu, G., Wang, W., Zeng, P., Yuan, C., Wang, L., Li, H., Zhang, H., Sun, X., Dai, K., Mao, J., Li, X., and Zhang, L. (2022). Strengthened d–p Orbital Hybridization through Asymmetric Coordination Engineering of Single-Atom Catalysts for Durable Lithium–Sulfur Batteries. *Nano Letters, 22*(15), 6366-6374.

Liu, K., Zhang, B., Chen, X., Huang, Y., Zhang, P., Zhou, D., Du, H., and Xiao, B. (2021). Modulating the Open-Circuit Voltage of Two-Dimensional MoB MBene

Electrode via Specific Surface Chemistry for Na/K Ion Batteries: A First-Principles Study. *The Journal of Physical Chemistry C, 125*(33), 18098-18107.

Liu, S., Bai, L., Wang, J., Zhang, M., and Niu, L. (2023). A first-principles study of functionalization effects on mechanical stability and electronic structure of Mo2B2 monolayers. *Materials Letters, 351*, 135068.

Liu, Z., Zhou, L., Ge, Q., Chen, R., Ni, M., Utetiwabo, W., Zhang, X., and Yang, W. (2018). Atomic Iron Catalysis of Polysulfide Conversion in Lithium–Sulfur Batteries. *ACS Applied Materials & Interfaces, 10*(23), 19311-19317.

Majed, A., Torkamanzadeh, M., Nwaokorie, C. F., Eisawi, K., Dun, C., Buck, A., Urban, J. J., Montemore, M. M., Presser, V., and Naguib, M. (2023). Toward MBenes Battery Electrode Materials: Layered Molybdenum Borides for Li-Ion Batteries. *Small Methods, 7*(8), 2300193.

Manthiram, A., Chung, S. H., and Zu, C. (2015). Lithium-sulfur batteries: progress and prospects. *Adv Mater, 27*(12), 1980-2006.

Mikhaylik, Y. V., and Akridge, J. R. (2004). Polysulfide Shuttle Study in the Li/S Battery System. *Journal of The Electrochemical Society, 151*(11), A1969.

Music, D., and Schneider, J. M. (2007). The correlation between the electronic structure and elastic properties of nanolaminates. *JOM, 59*(7), 60-64.

Nazar, L. F., Cuisinier, M., and Pang, Q. (2014). Lithium-sulfur batteries. *MRS Bulletin, 39*(5), 436-442.

Nørskov, J. K., Rossmeisl, J., Logadottir, A., Lindqvist, L., Kitchin, J. R., Bligaard, T., and Jónsson, H. (2004). Origin of the Overpotential for Oxygen Reduction at a Fuel-Cell Cathode. *The Journal of Physical Chemistry B, 108*(46), 17886-17892.

Park, H., Encinas, A., Scheifers, J. P., Zhang, Y., and Fokwa, B. P. T. (2017). Boron-Dependency of Molybdenum Boride Electrocatalysts for the Hydrogen Evolution Reaction. *Angewandte Chemie International Edition, 56*(20), 5575-5578.

Pei, G. X., Liu, X. Y., Wang, A., Lee, A. F., Isaacs, M. A., Li, L., Pan, X., Yang, X., Wang, X., Tai, Z., Wilson, K., and Zhang, T. (2015). Ag Alloyed Pd Single-Atom Catalysts for Efficient Selective Hydrogenation of Acetylene to Ethylene in Excess Ethylene. *ACS Catalysis, 5*(6), 3717-3725.

Qu, Y., Li, Z., Chen, W., Lin, Y., Yuan, T., Yang, Z., Zhao, C., Wang, J., Zhao, C., Wang, X., Zhou, F., Zhuang, Z., Wu, Y., and Li, Y. (2018). Direct transformation of bulk copper into copper single sites via emitting and trapping of atoms. *Nature Catalysis, 1*(10), 781-786.

Ren, M., Lu, X., Chai, Y., Zhou, X., Ren, J., Zheng, Q., and Lin, D. (2019). A three-dimensional conductive cross-linked all-carbon network hybrid as a sulfur host for high performance lithium-sulfur batteries. *Journal of Colloid and Interface Science, 552*, 91-100.

Rout, C. S., Shinde, P. V., Patra, A., and Jeong, S. M. (2024). Recent Developments and Future Perspectives of Molybdenum Borides and MBenes. *Advanced Science, 11*(21), 2308178.

Rybkovskiy, D. V., Kvashnin, A. G., Kvashnina, Y. A., and Oganov, A. R. (2020). Structure, Stability, and Mechanical Properties of Boron-Rich Mo–B Phases: A Computational Study. *The Journal of Physical Chemistry Letters, 11*(7), 2393-2401.

Sahu, R., Bogdanovski, D., Achenbach, J.-O., Zhang, S., Hans, M., Primetzhofer, D., Schneider, J. M., and Scheu, C. (2021). Direct MoB MBene domain formation in magnetron sputtered MoAlB thin films. *Nanoscale, 13*(43), 18077-18083.

Shen, Z., Cao, M., Zhang, Z., Pu, J., Zhong, C., Li, J., Ma, H., Li, F., Zhu, J., Pan, F., and Zhang, H. (2020). Efficient Ni2Co4P3 Nanowires Catalysts Enhance Ultrahigh-Loading Lithium–Sulfur Conversion in a Microreactor-Like Battery. *Advanced Functional Materials, 30*(3), 1906661.

Shim, J., Striebel, K. A., and Cairns, E. J. (2002). The Lithium/Sulfur Rechargeable Cell : Effects of Electrode Composition and Solvent on Cell Performance. *Journal of The Electrochemical Society, 149*(10), A1321.

Shukla, A. (2024). Tailoring Hydrogen Evolution Reaction with single-atom catalysts on Ti2B MBenes: Insights from computational screening. *International Journal of Hydrogen Energy, 77*, 479-485.

Song, J., Yu, Z., Gordin, M. L., and Wang, D. (2016). Advanced Sulfur Cathode Enabled by Highly Crumpled Nitrogen-Doped Graphene Sheets for High-Energy-Density Lithium–Sulfur Batteries. *Nano Letters, 16*(2), 864-870.

Wang, A., Li, J., and Zhang, T. (2018). Heterogeneous single-atom catalysis. *Nature Reviews Chemistry, 2*(6), 65-81.

Wang, D.-W., Zeng, Q., Zhou, G., Yin, L., Li, F., Cheng, H.-M., Gentle, I. R., and Lu, G. Q. M. (2013). Carbon–sulfur composites for Li–S batteries: status and prospects. *Journal of Materials Chemistry A, 1*(33), 9382-9394.

Wang, E., Zhang, B., Zhou, J., and Sun, Z. (2022). High catalytic activity of MBenes-supported single atom catalysts for oxygen reduction and oxygen evolution reaction. *Applied Surface Science, 604*, 154522.

Wang, L., Hu, Z., Wan, X., Hua, W., Li, H., Yang, Q.-H., and Wang, W. (2022). Li2S4 Anchoring Governs the Catalytic Sulfur Reduction on Defective $SmMn_2O_5$ in Lithium–Sulfur Battery. *Advanced Energy Materials, 12*(20), 2200340.

Wang, L., Wang, Y., and Xia, Y. (2015). A high performance lithium-ion sulfur battery based on a Li2S cathode using a dual-phase electrolyte. *Energy & Environmental Science, 8*(5), 1551-1558.

Wang, R., Luo, C., Wang, T., Zhou, G., Deng, Y., He, Y., Zhang, Q., Kang, F., Lv, W., and Yang, Q.-H. (2020). Bidirectional Catalysts for Liquid–Solid Redox Conversion in Lithium–Sulfur Batteries. *Advanced Materials, 32*(32), 2000315.

Wang, T., Luo, D., Zhang, Y., Zhang, Z., Wang, J., Cui, G., Wang, X., Yu, A., and Chen, Z. (2021). Hierarchically Porous Ti3C2 MXene with Tunable Active Edges and Unsaturated Coordination Bonds for Superior Lithium–Sulfur Batteries. *ACS Nano, 15*(12), 19457-19467.

Wang, Y., Zhang, H., Jiao, S., Chou, K.-C., and Zhang, G.-H. (2020). A facile pathway to prepare molybdenum boride powder from molybdenum and boron carbide. *Journal of the American Ceramic Society, 103*(4), 2399-2406.

Wild, M., O'Neill, L., Zhang, T., Purkayastha, R., Minton, G., Marinescu, M., and Offer, G. J. (2015). Lithium sulfur batteries, a mechanistic review. *Energy & Environmental Science, 8*(12), 3477-3494.

Xiao, Y., Li, Y., Guo, Z., Tang, C., Sa, B., Miao, N., Zhou, J., and Sun, Z. (2021). Functionalized Mo2B2 MBenes: Promising anchoring and electrocatalysis materials for Lithium-Sulfur battery. *Applied Surface Science, 566*, 150634.

Xu, R., Belharouak, I., Li, J. C. M., Zhang, X., Bloom, I., and Bareño, J. (2013). Role of Polysulfides in Self-Healing Lithium–Sulfur Batteries. *Advanced Energy Materials, 3*(7), 833-838.

Xu, X., Wang, S., Wang, H., Xu, B., Hu, C., Jin, Y., Liu, J., and Yan, H. (2017). The suppression of lithium dendrite growth in lithium sulfur batteries: A review. *Journal of Energy Storage, 13*, 387-400.

Xu, Z., Fan, M., Wang, J., Zhang, F., Lin, W., and Zhang, H. (2020). Trace Iron-Decorated Nitrogen/Sulfur Co-Doped Hierarchically Porous Carbon for Oxygen Reduction and Lithium–Sulfur Batteries. *ACS Applied Energy Materials, 3*(3), 2719-2726.

Yang, L., Li, Q., Wang, Y., Chen, Y., Guo, X., Wu, Z., Chen, G., Zhong, B., Xiang, W., and Zhong, Y. (2020). A review of cathode materials in lithium-sulfur batteries. *Ionics, 26*(11), 5299-5318.

Yang, X.-F., Wang, A., Qiao, B., Li, J., Liu, J., and Zhang, T. (2013). Single-Atom Catalysts: A New Frontier in Heterogeneous Catalysis. *Accounts of Chemical Research, 46*(8), 1740-1748.

Yang, Y., Zheng, G., Misra, S., Nelson, J., Toney, M. F., and Cui, Y. (2012). High-Capacity Micrometer-Sized Li2S Particles as Cathode Materials for Advanced Rechargeable Lithium-Ion Batteries. *Journal of the American Chemical Society, 134*(37), 15387-15394.

Yao, M., Shi, Z., Zhang, P., Ong, W.-J., Jiang, J., Ching, W.-Y., and Li, N. (2020). Density Functional Theory Study of Single Metal Atoms Embedded into MBene for Electrocatalytic Conversion of N_2 to NH_3. *ACS Applied Nano Materials, 3*(10), 9870-9879.

Zhang, D., Luo, Y., Liu, J., Dong, Y., Xiang, C., Zhao, C., Shu, H., Hou, J., Wang, X., and Chen, M. (2022). $ZnFe_2O_4$–Ni_5P_4 Mott–Schottky Heterojunctions to Promote Kinetics for Advanced Li–S Batteries. *ACS Applied Materials & Interfaces, 14*(20), 23546-23557.

Zhang, J., Zhang, J., Liu, K., Yang, T., Tian, J., Wang, C., Chen, M., and Wang, X. (2019). Abundant Defects-Induced Interfaces Enabling Effective Anchoring for Polysulfides and Enhanced Kinetics in Lean Electrolyte Lithium–Sulfur Batteries. *ACS Applied Materials & Interfaces, 11*(50), 46767-46775.

Zhang, L., Banis, M. N., and Sun, X. (2018). Single-atom catalysts by the atomic layer deposition technique. *National Science Review, 5*(5), 628-630.

Zhang, L., Sun, D., Feng, J., Cairns, E. J., and Guo, J. (2017). Revealing the Electrochemical Charging Mechanism of Nanosized Li_2S by in Situ and Operando X-ray Absorption Spectroscopy. *Nano Letters, 17*(8), 5084-5091.

Zhang, S. S. (2013). Liquid electrolyte lithium/sulfur battery: Fundamental chemistry, problems, and solutions. *Journal of Power Sources, 231*, 153-162.

Zhang, S. S., Foster, D., and Read, J. (2010). A high energy density lithium/sulfur–oxygen hybrid battery. *Journal of Power Sources, 195*(11), 3684-3688.

Zhang, T., Zhang, B., Peng, Q., Zhou, J., and Sun, Z. (2021). Mo_2B_2 MBene-supported single-atom catalysts as bifunctional HER/OER and OER/ORR electrocatalysts. *Journal of Materials Chemistry A, 9*(1), 433-441.

Zhang, Z., Li, Y., Mo, F., Wang, J., Ling, W., Yu, M., and Huang, Y. (2024). MBene with Redox-Active Terminal Groups for an Energy-Dense Cascade Aqueous Battery. *Advanced Materials, 36*(16), 2311914.

Zhou, G., Zhao, S., Wang, T., Yang, S.-Z., Johannessen, B., Chen, H., Liu, C., Ye, Y., Wu, Y., Peng, Y., Liu, C., Jiang, S. P., Zhang, Q., and Cui, Y. (2020). Theoretical Calculation Guided Design of Single-Atom Catalysts toward Fast Kinetic and Long-Life Li–S Batteries. *Nano Letters, 20*(2), 1252-1261.

Zuo, J.-H., Zhai, P.-B., He, Q.-Q., Wang, L., Chen, Q., Gu, X.-K., Yang, Z.-L., and Gong, Y.-J. (2022). In-situ constructed three-dimensional MoS_2–MoN heterostructure as the cathode of lithium–sulfur battery. *Rare Metals, 41*(5), 1743-1752.

CHAPTER III
CALCULATION DETAILS

In this thesis, we used density functional theory to describe the quantum behavior of atoms, molecules, and 2D materials. To study single atom decoration on $Mo_2B_2O_2$ (SA-$Mo_2B_2O_2$), various computational methods were employed, providing understanding for suggestion the most suitable SA-$Mo_2B_2O_2$ as a cathode material for Li-S batteries. This chapter provides an overview of the theoretical and computational methods used in this thesis. It begins with an introduction to the fundamentals of the Schrödinger equation for multi-particle systems (Section 3.1), followed by a detailed explanation of the core principles of DFT (Section 3.2).

Subsequently, the methodology for structural optimization, a crucial step in providing stable structures, is described in Section 3.3. To address the errors inherent in DFT calculations, techniques for error correction are discussed in Section 3.4. For studying the reaction kinetics of Li_2S decomposition and atom diffusion, the climbing image-nudged elastic band (CI-NEB) method is introduced in Section 3.5. Additionally, ab initio molecular dynamics (AIMD) simulations were used to study the adsorption behavior of LiPSs, including solvent effects, and to analyze their dynamic behavior at the atomic level (Section 3.6).

To further understand the sulfur reduction reaction (SRR) process with SA-$Mo_2B_2O_2$, Gibbs free energy (G) calculations were employed, as detailed in Section 3.7. The crystal orbital Hamilton population (COHP) method, used to evaluate bond strength, is described in Section 3.8. All these methodologies were implemented using the Vienna Ab initio Simulation Package (VASP), as summarized in Section 3.9.

3.1 Schrödinger equation for many particles

Understanding the quantum behavior of systems with multiple particles is fundamentally grounded in the Schrödinger equation. Formulated by Erwin Schrödinger in the 1920s, this equation provides a mathematical framework for describing the wavefunctions of complex systems. The general form of the Schrödinger equation can be written

$$\hat{H}\Psi(\vec{R_i}, \vec{r_j}) = E\Psi(\vec{R_i}, \vec{r_j}) \tag{3.1}$$

The equation is an eigenvalue equation where $\hat{H}$ is the Hamiltonian operator, Ψ is the wavefunction dependent on the coordinates of nuclei ($\vec{R_i}$) and electrons ($\vec{r_j}$), and E is the energy eigenvalue of the system. The Hamiltonian operator consists of kinetic energy and potential energy terms for nuclei and electrons. Thus, the Hamiltonian can be written as

$$\begin{aligned}\hat{H} &= T_N + T_e + V_{NN} + V_{Ne} + V_{ee} \\ &= -\sum_{i=1}^{N} \frac{\hbar^2}{2M_i}\nabla_{R_i}^2 - \sum_{j=1}^{n} \frac{\hbar^2}{2m_j}\nabla_{r_j}^2 + \frac{1}{2}\sum_{i=1}^{N}\sum_{i'=1}^{N} \frac{1}{4\pi\epsilon_0}\frac{Z_i Z_{i'} e^2}{|R_i - R_{i'}|} \\ &\quad - \sum_{i=1}^{N}\sum_{j=1}^{n} \frac{1}{4\pi\epsilon_0}\frac{Z_i e^2}{|R_i - r_j|} + \frac{1}{2}\sum_{j=1}^{n}\sum_{j'=1}^{n} \frac{1}{4\pi\epsilon_0}\frac{e^2}{|r_j - r_{j'}|}\end{aligned} \tag{3.2}$$

Where T_N and T_e are kinetic energy operators of nucleus and electron, respectively. V_{NN}, V_{Ne} and V_{ee} are potential operators of nucleus-nucleus interaction, nucleus-electron interaction, and electron-electron interaction, respectively. The kinetic operators can be explained as shown in equation (3.2), including $\hbar = h/2\pi$. M_i is the mass of nucleus and m_j is mass of an electron. The potential operators consist of Z_i, R_i, and r_j which are atomic number of nuclei and position of nucleus and electrons, respectively.

Solving the full Schrödinger equation with many particles is computationally challenging due to the complexity of the system. To simplify the problem, the Born-Oppenheimer approximation (Born et al., 1927) is often applied. This approximation assumes that the motion of atomic nuclei and electrons occurs on vastly different time scales. Therefore, the motions of nuclei and electrons can be treated as

decoupled, allowing the nuclei to be considered fixed while solving the electronic Schrödinger equation. Consequently, the Hamiltonian operator can be reduced as equation 3.3 based on the time-independent Schrödinger

$$\begin{pmatrix} -\sum_{j=1}^{n} \frac{\hbar^2}{2m_j} \nabla_{r_j}^2 & -\sum_{i=1}^{N} \sum_{j=1}^{n} \frac{1}{4\pi\epsilon_0} \frac{Z_i e^2}{|R_i - r_j|} \\ & +\frac{1}{2} \sum_{j=1}^{n} \sum_{j'=1}^{n} \frac{1}{4\pi\epsilon_0} \frac{e^2}{|r_j - r_{j'}|} \end{pmatrix} \Psi(\vec{r}_j) = E\Psi(\vec{r}_j) \quad (3.3)$$

The Born-Oppenheimer approximation can determine electronic energy level and wavefunctions, which form the basis of calculating a wide range of molecular properties. These include bond lengths, bond angles, vibrational frequencies, and other characteristics critical to understanding molecular systems.

3.2 Density functional theory

Density functional theory (DFT) is a quantum mechanical (QM) method widely used in chemistry and physics to calculate the electronic density of atoms, as shown in equation (3.4), instead of tracking individual particles within the system. This theory simplifies the approximation of Schrödinger equation, offering a more computationally efficient alternative to the Hartree-Fock method. he electron density, expressed in terms of the wavefunction, represents a fundamental connection between the DFT method and the quantum mechanical description of electronic systems:

$$\rho(\vec{r}) = \sum_i \Psi_i^*(\vec{r}) \Psi_i(\vec{r}) = \sum_i |\Psi(\vec{r})|^2 \quad (3.4)$$

where $\rho(\vec{r})$ represents the electron density at a given position $\vec{r}$, where interaction between electrons is not explicitly considered.

3.2.1 The Hohenberg-Kohn theorems

The Hohenberg-Kohn theorems (Hohenberg et al., 1964), developed by Pierre Hohenberg and Walter Kohn in 1964, are foundational principles in quantum mechanics and form the theoretical basis of DFT. The theorems consist of two key statements, often referred to as the first and second Hohenberg-Kohn theorems.

In case of first theorem, the external potential $V(r)$ uniquely determines the ground-state electron density $\rho(r)$, and vice versa. In other words, knowing the

external potential allows you to determine the electron density, and knowing the electron density allows you to reconstruct the external potential. This theorem forms the basis for expressing the total energy of a quantum system as a function of electron density, $E[\rho]$, and the external potential, $V(r)$. The main goal of DFT is to suggest the electron density which minimized the total energy. This energy is ground-state electron density and energy. $\rho_0(r)$,

For the second theorem, it emphasizes the uniqueness of the ground-state electron density and the total energy of a quantum system. It describes a one-to-one correspondence between the ground-state electron density, $\rho_0(r)$, and the external potential, $V_0(r)$, which results in the same minimum value of the ground-state energy. In other words, a single ground-state electron density and its corresponding external potential uniquely minimize the total energy of the system. This relationship is mathematically represented as:

$$E[\rho_0(r)] = \frac{\partial E[\rho(r)]}{\partial \rho}|_{\rho=\rho_o(r)} = min_{\rho\to\rho_0} E[\rho(r)] \qquad (3.5)$$

These theorems form the basis of DFT, which focuses on suggesting the electron density that minimizes the total energy functional of a quantum system. Although the Hohenberg-Kohn theorems do not provide a direct method for calculating the ground-state electron density, they offer a theoretical framework that ensures the accuracy and reliability of DFT in predicting the properties of many-electron systems.

3.2.2 The Kohn-Sham equation

The second Hohenberg-Kohn theorem provides the foundation for determining the ground-state energy of a quantum system by minimizing the total energy functional with respect to the electron density. In the framework of DFT, the total energy of a many-electron system is expressed as a functional of the electron density. This approach allows for the accurate prediction of ground-state properties without explicitly solving the many-body Schrödinger equation.

In the Kohn-Sham equation, a central component of DFT, the kinetic energy of electrons in a many-particle system is separated into two terms: (1) the kinetic energy

of non-interacting electrons and (2) the contribution from electron-electron correlations, often referred to as the correlation effect on kinetic energy. This decomposition leads to the formulation of the kinetic energy for electrons in a many-particle system as:

$$T[\rho(r)] = T_{non}[\rho(r)] + T_{cor}[\rho(r)] \tag{3.6}$$

For a system consisting of nuclei N and electrons N_e, the kinetic energy of non-interacting electrons can be represented as:

$$T_{non}[\rho(r)] = \sum_{i}^{N_e} \langle \psi_i(r) | \frac{-\nabla^2}{2} | \psi_i(r) \rangle \tag{3.7}$$

This term describes kinetic energy as if the electrons were moving independently, disregarding electron-electron interactions. However, in real systems, interactions between electrons significantly impact the total energy, necessitating the inclusion of potential energy terms. The potential energy contributions from electron-electron interactions and electron-nucleus interactions are given by:

$$V_{ee} = \langle \psi_e(r) | \frac{1}{2} \sum_{i}^{N_e} \sum_{j}^{N_e} \frac{1}{|r_i - r_j|} | \psi_e(r) \rangle = \frac{1}{2} \int \int \frac{\rho(r)\rho(r')}{|r - r'|} dr dr' \tag{3.8}$$

$$V_{Ne} = \langle \psi_e(r) | \sum_{i}^{N} \sum_{j}^{N_e} \frac{-Z_i}{|R_i - r_j|} | \psi_e(r) \rangle = -\sum_{i=1}^{N} \int \frac{Z_I \rho(r)}{|R_I - r|} dr \tag{3.9}$$

These terms encapsulate the electrostatic forces within the system. V_{ee} accounts for the repulsive interactions between electrons, while V_{Ne} describes the attractive forces between electrons and nuclei. Together, these terms are crucial for determining the system's total energy.

In the Hartree-Fock approximation, the exchange energy naturally arises from the antisymmetric nature of electron wavefunctions, a consequence of the Pauli exclusion principle. However, this approximation neglects the correlation energy, which represents the additional energy associated with the dynamic interactions between electrons. To overcome this limitation, DFT combines both the exchange and

correlation energy into a single term known as the exchange-correlation energy, denoted as:

$$E_{xc}[\rho(r)] = E_x[\rho(r)] + E_c[\rho(r)] \tag{3.10}$$

This unified term allows DFT to incorporate both effects seamlessly, improving accuracy over the Hartree-Fock method. The total energy of a many-particle system in DFT is expressed as:

$$\begin{aligned} E[\rho(r)] = T_{non}[\rho(r)] + \frac{1}{2}\int\int \frac{\rho(r)\rho(r')}{|r-r'|}drdr' \\ - \sum_{i=1}^{N} \frac{Z_i\rho(r)}{|R_i - r|}dr + E_{xc}[\rho(r)] \end{aligned} \tag{3.11}$$

According to the second Hohenberg-Kohn theorem, the ground-state energy of a quantum system corresponds to the minimum value of this energy functional. The condition for achieving this minimum is given by:

$$\left[-\frac{\nabla_i^2}{2} + V_{eff}[\rho(r)]\right]\psi_i^{KS}(r) = E_i\psi_i^{KS}(r) \tag{3.12}$$

The effective potential in the Kohn-Sham equation, which governs the behavior of the electrons, can be written as:

$$\begin{aligned} V_{eff}[\rho(r)] &= V_H[\rho(r)] + V_{ext}[\rho(r)] + Vxc[\rho(r)] \\ &= \frac{1}{2}\int \frac{\rho(r')}{|r-r'|}dr' - \sum_{i=1}^{N}\frac{Z_i}{|R_i - r|} + V_{xc}[\rho(r)] \end{aligned} \tag{3.13}$$

This effective potential includes contributions from the external potential, the Hartree potential (arising from electron-electron interactions), and the exchange-correlation potential, which incorporates quantum mechanical corrections. By solving the Kohn-Sham equations iteratively, the ground-state electron density and corresponding energy of the system can be determined. This methodology makes DFT a powerful tool for studying the electronic structure of complex systems, bridging the gap between computational efficiency and physical accuracy.

3.2.3 Exchange-correlation functional

For DFT calculations, the exchange-correlation potential (XC) accounts for all quantum mechanical interactions and effects that are not included in other potentials in density functional theory (DFT). The XC operator is a critical yet challenging component of DFT because its exact form remains unknown. Although XC energy typically constitutes less than 10% of the total energy, it plays a vital role in determining the properties of materials in DFT calculations.

In the present day, various approximations of the XC functional have been proposed, including the local density approximation (LDA) and the generalized gradient approximation (GGA). The local XC energy per electron can be expressed as:

$$\varepsilon_{XC}[\rho(\vec{r})] = \frac{1}{2}\int \frac{\rho_{XC}(\vec{r},\vec{r}')}{|\vec{r}-\vec{r}'|} d\vec{r}' \tag{3.14}$$

Then

$$E_{XC}[\rho(\vec{r})] = \int \rho(\vec{r})\, \varepsilon_{XC}(\vec{r},\rho) d\vec{r} \tag{3.15}$$

For the LDA, the XC functional is exact for a homogeneous electron gas. The XC energy for the LDA can be written as:

$$E_{XC}^{LDA}[\rho(\vec{r})] = \int \rho(\vec{r})\, \varepsilon_{XC}^{LDA}[\rho(\vec{r})] d\vec{r} \tag{3.16}$$

Nevertheless, the LDA has imitations in accurately describing systems with varying electron densities (inhomogeneous), making it less suitable for real systems with complex electronic structures. To overcome these limitations, GGA incorporates the density gradient, allowing it to account for inhomogeneous behavior more effectively. The general formula for the XC energy in GGA is given by:

$$E_{XC}^{GGA}[\rho(\vec{r})] = \int \rho(\vec{r})\, \varepsilon_{XC}^{GGA}[\rho(\vec{r}), \nabla\rho(\vec{r})] d\vec{r} \tag{3.17}$$

GGA functionals are widely used due to their accuracy for a range of properties, inculding ground-state energies, molecular geometries, and covalent bonding. The are also well-suited for weakly bonded systems (Santra, 2010). Currently, several forms of

GGA functionals have been developed, including PW91 (J. P. Perdew et al., 1992), PBE (Ernzerhof et al., 1999; Hammer et al., 1999; Wan et al., 2021). In our work, the PBE functional is mainly used due to iss balance of accuracy and computational efficiency. The PBE functional can be written as:

$$\varepsilon_{XC}^{PBE}[\rho(\vec{r}), \nabla\rho(\vec{r})] = -\frac{3}{4}\left(\frac{3}{\pi}\right)^{\frac{1}{3}} n^{\frac{1}{3}}(\vec{r})F(x) \tag{3.19}$$

where

$$F(x) = 1 + a - \frac{a}{1+bx^2}, \qquad x = \frac{|\nabla\rho(\vec{r})|}{n^{\frac{4}{3}}(\vec{r})} \tag{3.20}$$

Where a and b are constants. Substituting equation (3.19) into equation (3.20), the corresponding XC potential for PBE is:

$$V_{XC}^{PBE}[\rho(\vec{r})] = \frac{\delta E_{XC}^{PBE}[\rho(\vec{r})]}{\delta\rho(\vec{r})} \tag{3.21}$$

The PBE functional's ability to incorporate density gradients while maintaining computational simplicity makes it a popular choice for a wide range of applications in materials science and quantum chemistry.

3.2.4 Pseudopotentials

Pseudopotentials are an essential tool for simplifying complex calculations in computational chemistry. They replace the true potential of atomic nuclei with an effective potential designed to replicate the behavior of valence (outermost) electrons, while either simplifying or neglecting the contributions of tightly bound inner-core electrons. In most cases, bond formation and electronic properties are determined by valence electrons, while core electrons are treated as part of the nuclei under the frozen-core approximation. This method simplifies the description of pseudo-wavefunctions and facilitates the practical use of plane-wave basis sets. Additionally, this simplification significantly reduces the computational cost of electronic structure calculations while maintaining accuracy for many properties of interest.

As shown in **Figure 3.1**, the pseudo and exact potential align when the interparticle distance exceeds the specified cutoff radius (r_c). Similarly, the pseudo (ψ_{peudo}) and exact (ψ_{exact}) wavefunctions also converge beyond this radius. Within the region below r_c , however, the exact wavefunction exhibits pronounced oscillations.

These oscillations make solving the Schrödinger equation challenging, as achieving a smooth and numerically stable wavefunction in this region requires significant computational effort, as shown by the red solid line in the figure.

To overcome this issue, a smoother pseudo-wavefunction is employed, which significantly reduces computational cost while maintaining accuracy. For the pseudo wavefunction and potential to be effective, they must satisfy the following criteria: (1) Consistency: The pseudo wavefunction and potential should match the exact counterparts beyond the cutoff radius. (2) Smoothness: Within the r_c region, the pseudo wavefunction should minimize oscillations to simplify numerical calculations. (3) Transferability: The pseudopotential should accurately describe the behavior of valence electrons across various chemical environments. These requirements ensure that pseudopotentials serve as an efficient and accurate approach to simplifying electronic structure calculations.

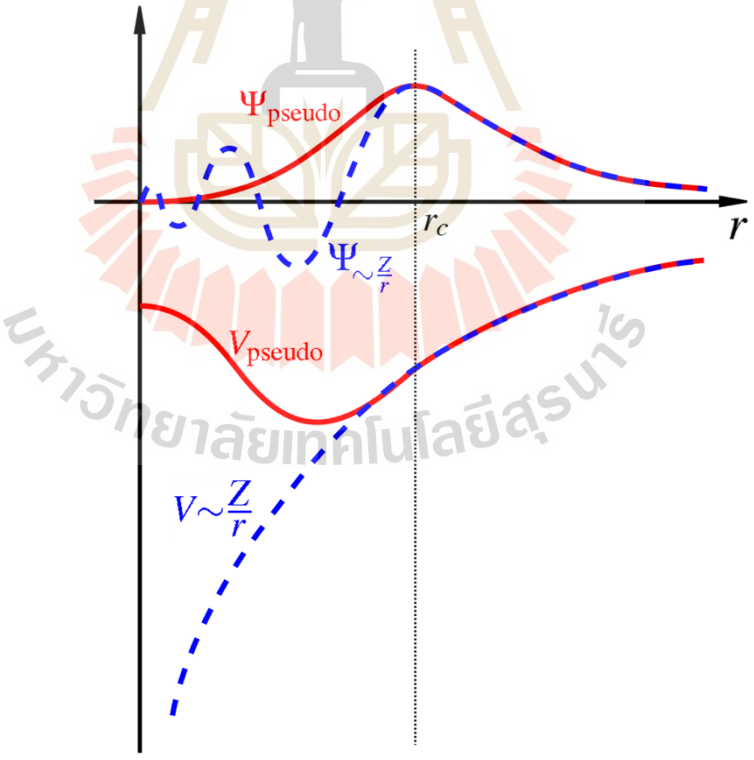

Figure 3.1 Comparison of wavefunctions in a nuclear Coulomb potential (blue) and a pseudopotential (red) (Grajcarova, 2013).

3.2.5 Self-consistent field approach

In practical DFT calculations, the ground-state energy of a many-body system is determined using a self-consistent field (SCF) method. This approach focuses on finding the lowest-energy configuration of atoms by solving the Kohn-Sham equation. **Figure 3.2** presents the flowchart of this process, ensuring that the electron density and effective potential reach a stable and consistent solution.

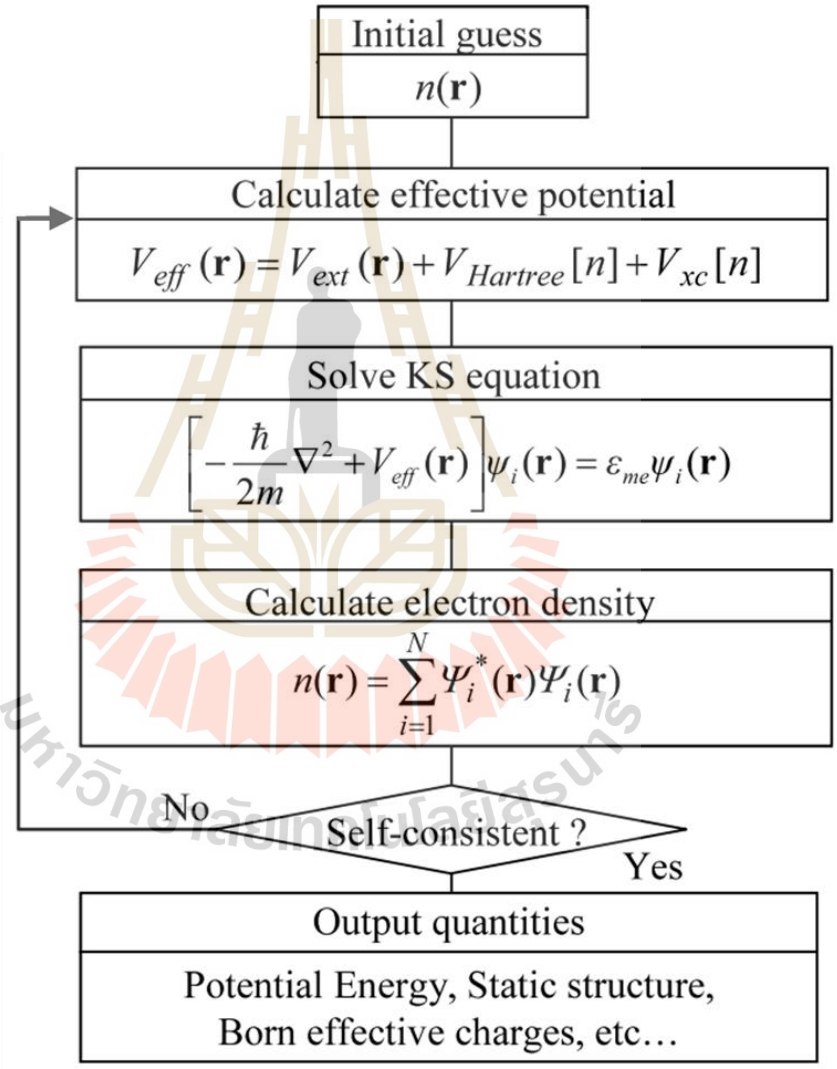

Figure 3.2 Flowchart showing the process of solving the Kohn-Sham equation (Nakamachi et al., 2013).

The SCF calculation follows a systematic process to determine the ground-state energy in density functional theory (DFT) calculations. The steps involved are as follows:

1. Initial electron density guess: make an initial assumption for the electron density
2. Effective potential calculation: compute the effective potential using the initial electron density
3. Solving the Kohn-Sham equation: Solve the Kohn-Sham equation to suggest the eigenvalues (total energy) and eigenvectors (wavefunctions)
4. New electron density calculation: Generate a new electron density based on the calculated eigenvectors (wavefunctions).
5. New energy calculation: Calculate the total electronic energy using the updated electron density in the Kohn-Sham equation
6. Energy convergence check: if the difference between the new and previous electronic energy is smaller than the predefined convergence criterion, the calculation terminates, and the resulting values are accepted. However, If the difference exceeds, update the electron density with the new values and repeat the process from step 2. This process is repeated until the calculated energy and electron density reach convergence, ensuring a consistent solution for the electron density and effective potential. In this thesis, the convergence criterion is set to 10^{-6} eV.

3.3 Geometry optimization

Geometry optimization is a critical step in DFT calculations, particularly for studying molecules and materials. The goal is to find the most energetically favorable arrangement of atoms by minimizing the system's total energy while adjusting atomic positions and, if applicable, unit cell dimensions. An overview of the geometry optimization process is provided below (see **Figure 3.3**). First step, it is initial geometry which starts with the initial atomic coordinate of the system. Next, the DFT calculation determines the system's total energy using the self-consistent field (SCF) method and further calculates the atomic forces using the Hellmann-Feynman theorem. In case of

convergence check after calculations, If the calculated atomic forces are below the predefined tolerance limit, the optimization is complete, and the resulting geometry is accepted. However, If the atomic forces exceed the tolerance limit, the atomic positions are adjusted based on the calculated forces and gradients. The optimization process then returns to step 2, iterating until convergence is achieved. Optimization algorithms, such as the conjugate gradient method, are typically used to guide the adjustments (Dai et al., 2016).

Geometry optimization is a foundational process in DFT that allows for accurate predictions of molecular and material properties. This method offers critical insights into the behavior, stability, and structural characteristics of chemical systems by calculating the optimal atomic positions and total energy.

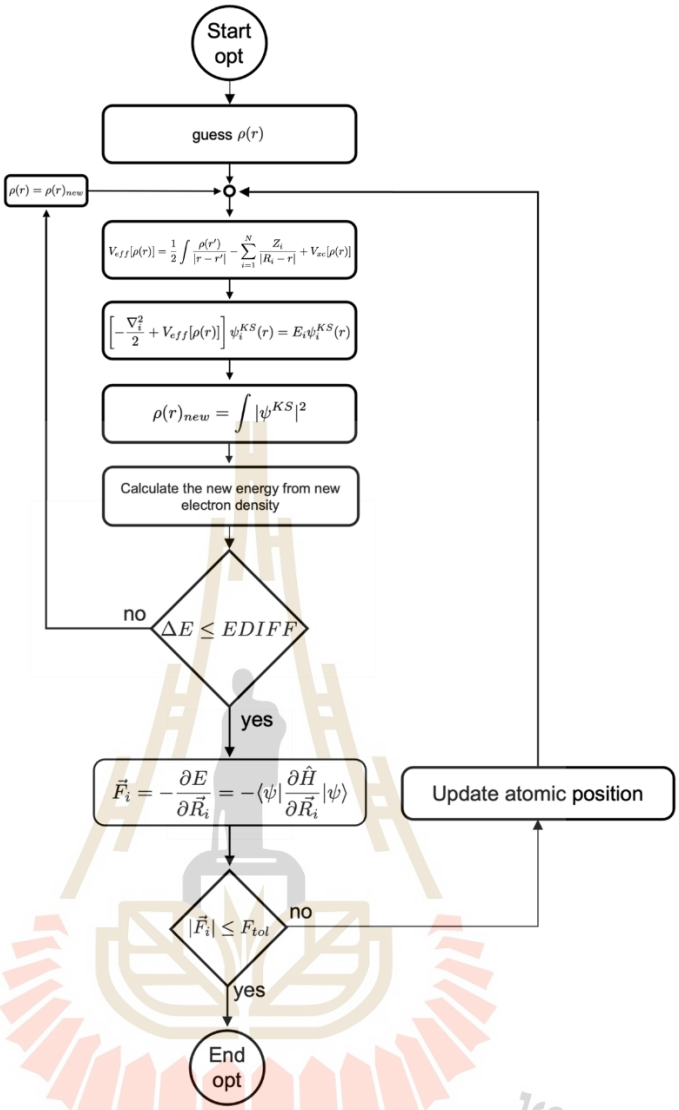

Figure 3.3 Schematic representation of the optimization process in DFT calculations.

3.4 vdW correction

One of the well-known limitations of DFT is its inability to accurately capture van der Waals (vdW) interactions. These interactions are weak, long-range forces between molecules or atoms that result from temporary fluctuations in electron density. Standard DFT functionals, including LDA and GGA, are designed to capture local exchange-correlation effects but frequently underestimate vdW interactions.

To overcome this limitation, various correction methods have been developed to incorporate vdW interactions into DFT calculations. One widely used approach in the DFT-D3 method developed by Grimme (Grimme et al., 2010). In this study, the

optPBE-vdW method (Klimes et al., 2010) is employed. This method modifies the standard PBE functional to systematically and accurately account for vdW interactions. Unlike the standard PBE functional, optPBE-vdW introduces a correction term to address long-range vdW interactions. This method improves the accuracy of DFT calculations for systems in which vdW forces play a significant role, including molecular complexes, layered materials, and systems with intermolecular interactions. The optPBE-vdW correction includes an interaction term between atomic pairs in the exchange-correlation functional, expressed as:

$$E_{disp}^{optPBE-vdW} = \sum_{AB} \frac{C_{6AB}}{R_{AB}^6} f_{damp}(R_{AB}) \tag{3.22}$$

Where:

$E_{disp}^{optPBE-vdW}$ is the dispersion energy correction

$\Sigma_{A,B}$ represents a sum over all atom pairs AAA and BBB in the system.

$C_{6,AB}$ is the dispersion coefficient for the atom pair AAA and BBB, determined empirically based on the types of atoms involved.

R_{AB} is the distance between atoms A and B.

$f_{damp}(R_{AB})$ is a damping function that ensures the correction smoothly decreases at short distances to avoid unphysical divergences.

The damping function is expressed as:

$$f_{damp}(R_{AB}) = 1 - exp(-\alpha(R_{AB} - R_S)^2) \tag{3.23}$$

Where:

- α is a damping parameter that controls the rate of decay.
- R_s is a cutoff radius beyond which the correction becomes negligible.

$C_{6,AB}$ coefficients, which represent the strength of dispersion interactions between atom pairs, are typically derived from empirical databases or parameterized based on experimental data. These coefficients vary depending on the atom types involved and are crucial for accurately describing vdW interactions.

3.5 Climbing image-nudged elastic band method

The climbing image-nudged elastic band (CI-NEB) (Henkelman et al., 2000) is an advanced computational technique widely used in DFT calculations to suggest transition states and map reaction pathways with precision. By enhancing the traditional Nudged Elastic Band (NEB) method, CI-NBE introduces a "climbing" image that converges toward the transition state, allowing for precise determination of the highest energy points along a reaction coordinate. Next, paraphrase will summarize knowledge of these methods.

In the case of NEB, it can calculate the reaction pathway by constructing a series of intermediate configurations (called images) that connect the initial and final states. Each image is characterized by specific atomic coordinates, forming an elastic band represented as [R_0, R_1, R_2, ..., R_N], where R_0 and R_N remain fixed as the initial and final state. The force acting on each image ($\boldsymbol{F_i}$) is a combination of spring force and true force. Spring force is used to ensure images remain evenly spaced along the reaction path. Ture force is used to account for the system's potential energy, acting perpendicular to the reaction path. The total force for an image i is expressed as:

$$\vec{F}_i^{NEB} = \vec{F}_i^{s||} - \nabla E(\vec{R}_i)^{\perp} \tag{3.24}$$

The true force is given by:

$$\nabla E(\vec{R}_i)^{\perp} = \nabla E(\vec{R}_i) - \nabla E(\vec{R}_i) \cdot \hat{\tau}_i \tag{3.25}$$

Where $\boldsymbol{\nabla E}$ is the gradient of energy with respect to atomic coordinates, and $\hat{\tau}_i$ is the normalized local tangent at image i. Spring force is defined as:

$$\vec{F}_i^{s||} = k(|\vec{R}_{i+1} - \vec{R}_i| - |\vec{R}_i - \vec{R}_{i-1}|)\hat{\tau}_i \tag{3.26}$$

Where k is spring constant. Optimization algorithms move the images according to NEB force until the forces converge below a set threshold. In our study, we set the convergence criterion for NEB calculations which is 0.05 eV/Å

The CI-NBE method improves upon NEB by refining the transition state suggestion. After several iterations with the standard NEB, the image with the highest

energy (i_{max}) is identified. This image is then allowed to "climb" toward the saddle point by modifying its force calculation:

$$\vec{F}_{i_{max}} = -\nabla E(\vec{R}_{i_{max}}) + 2\nabla E(\vec{R}_{i_{max}}) \cdot \hat{\tau}_{i_{max}} \tag{3.27}$$

This modification ensures that the climbing image is unaffected by spring forces and moves directly to the saddle point, representing the transition state. Consequently, the CI-NEB method is widely used in computational chemistry to study reaction mechanisms and calculate energy barriers for chemical reactions. It delivers three key benefits by determining the transition state with accuracy, mapping minimum energy pathways precisely, and providing insights into the reaction dynamics of complex systems.

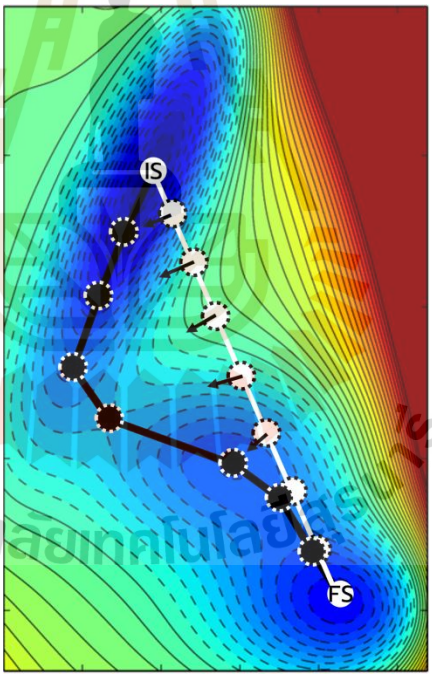

Figure 3.4 Schematic of the potential energy surface (PES) and NEB calculation, showing the initial reaction pathway (white line) and the optimized reaction pathway (black line).

Overall, the CI-NEB method combines the principles of the NEB method with the climbing image adjustment, providing an efficient and reliable approach for identifying transition states and understanding reaction mechanisms. By ensuring

accurate placement of the transition state along the reaction coordinate, CI-NEB is a critical tool for investigating complex chemical reactions and energy landscapes.

3.6 Ab initio molecular dynamics

Ab initio molecular dynamics (AIMD) is a powerful computational technique widely used in quantum chemistry and materials science to simulate the time-dependent motion of atoms and molecules. AIMD combines the principles of molecular dynamics (MD) with quantum mechanical calculations, often based on density functional theory (DFT) or other first-principles methods, to accurately model electronic structures and interatomic interactions. This hybrid approach enables AIMD to explore and understand the dynamic behavior of complex systems at the quantum level. The key components of AIMD can be summarized as follows.

1. Quantum mechanical calculations

At each time step, AIMD applies quantum mechanical methods, which is DFT in our work, to calculate the electronic structure and the resulting forces on each atom. These forces, denoted as equation (3.27), are derived from energy gradients of the electronic structure:

$$\vec{F}_i = -\langle\psi|\frac{\partial\hat{H}}{\partial\vec{R}_i}|\psi\rangle \tag{3.28}$$

2. Newton's equations of motion

The atomic position (r) and velocities (v) change over time following the principles of classical Newtonian mechanics. The movement of each atom is described by:

$$m_i\frac{d^2\vec{r}_i}{dt^2} = \vec{F}_i \tag{3.29}$$

3. Integration Scheme

Numerical methods, such as the Verlet or velocity-Verlet algorithms, are used to solve Newton’s equations of motion and update atomic positions and velocities at each time step:

$$\begin{aligned}\vec{a}_i(t+\Delta t) &= \frac{\vec{F}_i(t+\Delta t)}{m_i} \\ \vec{v}_i(t+\Delta t) &= \vec{v}_i(t) + \frac{1}{2}(\vec{a}_i(t) + \vec{a}_i(t+\Delta t)) \\ \vec{R}_i(t+\Delta t) &= \vec{R}_i(t) + \vec{v}_i(t)\Delta t + \frac{1}{2}\vec{a}_i(t)\Delta t^2\end{aligned} \tag{3.30}$$

4. Boundary Conditions

Periodic boundary conditions are applied to mimic an effectively infinite system, replicating the simulation cell in all directions. This method reduces edge effects and provides an accurate representation of atomic interactions in bulk materials

5. Temperature Control

AIMD simulations often use thermostats, such as the Nosé-Hoover thermostat, to regulate temperature. These control mechanisms enable simulations at specific temperatures, facilitating the study of temperature-dependent phenomena like phase transitions and reaction rates. (Hoover, 1985; Nosé, 1984).

6. Time Steps

The choice of the time step (Δt) is critical. It must be small enough (e.g., in the order of femtoseconds) to accurately capture atomic vibrations while maintaining computational efficiency. A carefully selected time step maintains accuracy while allowing for practical simulation durations.

AIMD simulations are powerful tools for studying dynamic processes in chemistry and materials science, offering a quantum-level understanding of phenomena including chemical reactions, vibrational dynamics, structural evolution, electrochemical systems. AIMD captures both electronic and atomic behavior, connecting quantum mechanics with real-world material properties. It is a valuable tool for studying systems that static DFT calculations cannot fully explain, helping us better understand molecular and material behavior at the atomic level.

3.7 Gibbs free energy (G) calculation

The Gibbs free energy (G) can be expressed as the sum of the system's enthalpy (H) and entropy (S), as shown below:

$$G = E_{elec} + E_{ZPE} - TS \tag{3.31}$$

Here, E_{elec} represents electronic energy, and E_{ZPE} is the zero-point energy correction applied to the electronic energy to account for quantum mechanical effects at absolute zero. The zero-point energy is calculated as:

$$ZPE = \sum_i \frac{h\nu_i}{2} \tag{3.32}$$

where, h is the Planck's constant and ν_i are the computed vibrational frequencies of the system. This correction is essential in ensuring accurate thermodynamic predictions, especially for molecular systems at low temperatures. For entropy (S), it is given by the equation:

$$S = k_B ln Q \tag{3.33}$$

The partition function (Q) can be expressed as the product of translational, rotational, and vibrational components:

$$Q = f_{trans} f_{vib} f_{rot} \tag{3.34}$$

In equation (3.33). The calculation of entropy relies on the partition function, which for ideal gas molecule can be divided into translational, rotational, and vibrational contributions. Each component corresponds to a specific type of motion or degree of freedom within the system. For a free-gas molecule, the translational partition function in three dimensions is given by:

$$f_{trans} = V\left(\frac{2\pi M k_b T}{h^2}\right)^{3/2} \tag{3.35}$$

where V is the volume of the gas, M is the molecular mass, k_B is the Boltzmann constant. Often, V can be substituted using the ideal gas equation of state $PV = k_BT$. For a single dimension, the translational partition function simplifies to:

$$f_{trans} = \frac{L\sqrt{2\pi m k_b T}}{h} \tag{3.36}$$

Where L is the characteristic length along one dimension. In case of the rotational partition function for a diatomic molecule can be expressed as:

$$f_{rot} = \frac{8\pi^2 I k_b T}{h^2} \tag{3.37}$$

Where I is the moment of inertia about an axis perpendicular to the molecular axis and passing through the center of mass.

In the harmonic approximation, the vibrational partition function is given as:

$$f_{vib} = \frac{1}{1 - e^{-h\omega/k_b T}} \tag{3.38}$$

Each vibrational mode contributes independently to the partition function, and the harmonic approximation assumes that the vibrations are small perturbations around equilibrium.

3.8 Crystal orbital Hamilton population (COHP)

The crystal orbital hamilton population (COHP) is a theoretical method used in computational chemistry and materials science to suggest chemical bonding in periodic systems (Steinberg et al., 2018). It is particularly effective in quantifying the bonding, nonbonding, and antibonding interactions between atomic orbitals in solids. The fundamental concept of COHP focused on partitioning the electronic structure of a system into contributions from specific atomic pairs or orbitals. It combines concepts from quantum mechanics and electronic structure theory, particularly the Hamiltonian formalism, to analyze the interaction between two atomic orbitals.

COHP is often evaluated relative to the Fermi level, which suggests the energy up to which the electronic states are occupied. The bonding interactions below the Fermi level are most significant in determining the stability of the system.

It can be calculated based on electronic Hamiltonian $(\hat{H})$ describes the total energy of the quantum system, including kinetic and potential energies. In COHP, it is used to evaluate the interaction between two atomic orbitals:

$$H_{ij} = \int \psi_i^*(\mathbf{r}) \hat{H} \psi_j(\mathbf{r}) d^3r \tag{3.39}$$

The term of Hamilton population quantifies the contribution of each orbital pair to the total electronic energy:

$$HP_{ij}(E) = -H_{ij}(E) \cdot n_{ij}(E) \tag{3.40}$$

After that, COHP is derived by integrating over all energy states:

$$-COHP(E) = -\sum_{i,j} H_{ij}(E) \cdot n_{ij}(E) \tag{3.41}$$

The negative value of COHP represents bonding contributions, whereas positive values show antibonding contributions. To obtain a single scalar value representing the total bonding interaction between two atoms, COHP can be integrated over all relevant energy levels:

$$ICOHP = \int_{E_{\min}}^{E_F} -COHP(E) dE \tag{3.42}$$

ICOHP value can suggest the bonding strength. Negative ICOHP suggest strong bonding interactions, while positive value suggest dominant antibonding interactions. Although COHP and ICOHP can explain the strength bond of pair atoms, it still has limitations which we should be concerned about. First, it is basis set dependence. Results can vary with the choice of basis sets, requiring careful validation. Computational cost increases with system size, especially for large supercells or complex systems. Lately, the choice of integration limits in ICOHP calculations can influence the results, particularly in systems with partially filled bands.

3.9 Summary of computational details

In this thesis, all calculations were employed using spin-polarized Density Functional Theory (DFT) as implemented in the Vienna Ab-initio Simulation Package (VASP 5.4) (Kresse et al., 1996a, 1996b). The frozen-core projector-augmented wave (PAW) method was used to describe the electron-ion interactions (Blöchl, 1994). For the $Mo_2B_2O_2$ structure, valence electrons included Mo 4d5s, B 2s2p, and O 2s2p treated within a plane-wave basis. For LiPS molecules, Li 2s and S 3s3p valence electrons were considered. Screening of single-atom (SA) transition metals included both 3*d*- and 4*d*-transition metals, considering their 3d4s and 4d5s valence electrons, respectively. The exchange-correlation interactions were approximated using the Generalized Gradient Approximation (GGA) with the Perdew-Burke-Ernzerhof (PBE) functional (John P. Perdew et al., 1996). Weak van der Waals interactions between the adsorbates (S_8 and LiPSs) and SA-$Mo_2B_2O_2$ were included using the DFT-D3 (Klimeš et al., 2010). Structural optimizations were carried out with a kinetic energy cutoff of 500 eV. Monkhorst-Pack k-point sampling was employed (Monkhorst et al., 1976), using a 5 × 5 × 1 grid for structural optimization and a 9 × 9 × 1 grid for electronic density of states (DOS) calculations. Optimization was considered complete when the energy difference between iterations reached 10^{-6} eV and residual forces were below 0.02 eV/Å. Charge distribution analysis was conducted using the Bader charge decomposition scheme (Tang et al., 2009). To investigate the shuttle effect in the presence of electrolyte molecules, ab initio molecular dynamics (AIMD) simulations were performed. These simulations examined the behavior of Li_2S_6 on SA-$Mo_2B_2O_2$ in 1,3-dioxolane (DOL) and 2-dimethoxyethane (DME) solvents. The simulations employed the NVT ensemble with a Nose-Hoover thermostat at 300 K, using a time step of 1 fs for a total simulation duration of 10 ps. Only Γ-point sampling was used to minimize computational costs, with an energy cutoff of 450 eV. The number of solvent molecules added to the vacuum region was based on their liquid densities: 1.06 g/cm³ for DOL and 0.87 g/cm³ for DME at room temperature. The energy barriers and reaction pathways for Li ion and SA diffusion were calculated using the Climbing Image Nudged Elastic Band (CI-NEB) method (Henkelman et al., 2000). Finally, electron occupancy in bonding and

antibonding orbitals was analyzed through Crystal Orbital Hamilton Population (COHP) analysis (Deringer et al., 2011).

3.10 References

Blöchl, P. E. (1994). Projector augmented-wave method. *Physical Review B, 50*(24), 17953-17979.

Born, M., and Oppenheimer, R. (1927). Zur Quantentheorie der Molekeln. *Annalen der Physik, 389*(20), 457-484.

Dai, X., Liu, Z., and Zhou, A. (2016). A Conjugate Gradient Method for Electronic Structure Calculations. *SIAM Journal on Scientific Computing, 39*

Deringer, V. L., Tchougréeff, A. L., and Dronskowski, R. (2011). Crystal Orbital Hamilton Population (COHP) Analysis As Projected from Plane-Wave Basis Sets. *The Journal of Physical Chemistry A, 115*(21), 5461-5466.

Ernzerhof, M., and Scuseria, G. E. (1999). Assessment of the Perdew–Burke–Ernzerhof exchange-correlation functional. *The Journal of Chemical Physics, 110*(11), 5029-5036.

Grajcarova, L. (2013). *Simulations of structural phase transitions in crystals using ab-initio metadynamics.*

Grimme, S., Antony, J., Ehrlich, S., and Krieg, H. (2010). A consistent and accurate ab initio parametrization of density functional dispersion correction (DFT-D) for the 94 elements H-Pu. *The Journal of Chemical Physics, 132*(15)

Hammer, B., Hansen, L. B., and Nørskov, J. K. (1999). Improved adsorption energetics within density-functional theory using revised Perdew-Burke-Ernzerhof functionals. *Physical Review B, 59*(11), 7413-7421.

Henkelman, G., Uberuaga, B. P., and Jónsson, H. (2000). A climbing image nudged elastic band method for finding saddle points and minimum energy paths. *The Journal of Chemical Physics, 113*(22), 9901-9904.

Hohenberg, P., and Kohn, W. (1964). Inhomogeneous Electron Gas. *Physical Review, 136*(3B), B864-B871.

Hoover, W. G. (1985). Canonical dynamics: Equilibrium phase-space distributions. *Physical Review A, 31*(3), 1695-1697.

Klimeš, J., Bowler, D. R., and Michaelides, A. (2010). Chemical accuracy for the van der Waals density functional. *Journal of Physics: Condensed Matter, 22*(2), 022201.

Kresse, G., and Furthmüller, J. (1996a). Efficiency of ab-initio total energy calculations for metals and semiconductors using a plane-wave basis set. *Computational Materials Science, 6*(1), 15-50.

Kresse, G., and Furthmüller, J. (1996b). Efficient iterative schemes for ab initio total-energy calculations using a plane-wave basis set. *Physical Review B, 54*(16), 11169-11186.

Monkhorst, H. J., and Pack, J. D. (1976). Special points for Brillouin-zone integrations. *Physical Review B, 13*(12), 5188-5192.

Nakamachi, E., Uetsuji, Y., Kuramae, H., Tsuchiya, K., and Hwang, H. (2013). Process Crystallographic Simulation for Biocompatible Piezoelectric Material Design and Generation. *Archives of Computational Methods in Engineering, 20*(2), 155-183.

Nosé, S. (1984). A unified formulation of the constant temperature molecular dynamics methods. *The Journal of Chemical Physics, 81*(1), 511-519.

Perdew, J. P., Burke, K., and Ernzerhof, M. (1996). Generalized Gradient Approximation Made Simple. *Physical Review Letters, 77*(18), 3865-3868.

Perdew, J. P., and Wang, Y. (1992). Accurate and simple analytic representation of the electron-gas correlation energy. *Phys Rev B Condens Matter, 45*(23), 13244-13249.

Santra, B. (2010). Density-Functional Theory Exchange-Correlation Functionals for Hydrogen Bonds in Water. *J. Chem. Phys. 127, 184104 (2007), J. Chem. Phys. 129, 194111 (2008), J. Chem. Phys. 131, 124509 (2009).*

Steinberg, S., and Dronskowski, R. (2018). The Crystal Orbital Hamilton Population (COHP) Method as a Tool to Visualize and Analyze Chemical Bonding in Intermetallic Compounds. *Crystals, 8*(5), 225.

Tang, W., Sanville, E., and Henkelman, G. (2009). A grid-based Bader analysis algorithm without lattice bias. *Journal of Physics: Condensed Matter, 21*(8), 084204.

Wan, Z., Wang, Q.-D., Liu, D., and Liang, J. (2021). Effectively improving the accuracy of PBE functional in calculating the solid band gap via machine learning. *Computational Materials Science, 198*, 110699.

CHAPTER IV
STRUCTURAL AND ELECTRONIC PROPERTIES OF $Mo_2B_2O_2$ AND SINGLE ATOM DECORATED $Mo_2B_2O_2$

Before studying and screeing the optimal single atom (SA) decorated Mo_2B_2 with oxygen functionalized surface (SA-$Mo_2B_2O_2$) as cathode materials, we first analyzed the structural and electronic porperties of both pristine and SA-$Mo_2B_2O_2$. The single atoms studied in this thesis include 3*d*- and 4*d*-transition metals, excluding molybdenum (Mo) since it is already present in the Mo_2B_2 structure. Although the synthesis of SA-$Mo_2B_2O_2$ has no yet been achieved, SA decoration has been successfully realized on MXenes, which share similar properties and structures with MBenes. This has been experimentally confirmed through advanced characterization techniques such as X-ray photoelectron spectroscopy (XPS). Moreover, computational studies strongly suggest that SA atoms preferentially bind to the surface of $Mo_2B_2O_2$, as demonstrated in previous research (Li et al., 2020; Mou et al., 2023). Therefore, SA-$Mo_2B_2O_2$ may be synthesized and is an interesting material for study in Li-S batteries.

In this thesis, a 4×4×1 $Mo_2B_2O_2$ supercell was used as the initial model. The potential adsorption sites for SA decoration on the $Mo_2B_2O_2$ surface, including four distinct sites, were systematically evaluated to suggest the most suitable positions. We studied the specific properties of each SA that influence adsorption behavior using Pearson correlation technique. Additionally, The electronic properties of both pristine and SA-decorated $Mo_2B_2O_2$ were further analyzed. All details were discussed in section 4.1. In section 4.2, we explored the specific properties of each SA that influence adsorption behavior using Pearson correlation technique. Furthermore, we analyzed the strengths of SA-O bond by crystal orbital Hamilton population (COHP).

4.1 Geometric and Electronic properties of calculated pristine and SA decorated $Mo_2B_2O_2$

We began by optimizing the pristine $Mo_2B_2O_2$ model, which serves as the supporting material for SA decoration. This 2D structure consists of two boron layers sandwiched between two molybdenum layers, with oxygen atoms functioning as surface groups covering the outermost layers of the Mo_2B_2 model, as shown in **Figure 4.1**. The calculations employed a 4 x 4 supercell consisting of 32 Mo atoms, 32 B atoms, and 32 O atoms. The optimized $Mo_2B_2O_2$ model has lattice parameters of 11.47 Å × 12.43 Å with a vacuum space of 20 Å and average bond lengths of Mo–B = 2.30 Å, Mo–O = 1.97 Å, and B–B = 1.68 Å. These results are consistent with previous computational research findings on the structural properties of $Mo_2B_2O_2$ (Xiao et al., 2021).

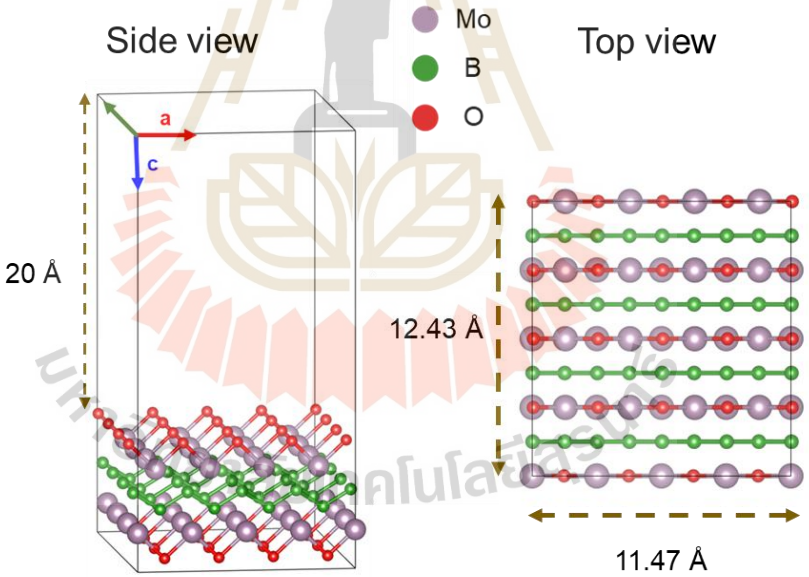

Figure 4.1 The most stable structure of $Mo_2B_2O_2$ before being decorated with SA.

Subsequently, we studied various configurations of SA-$Mo_2B_2O_2$, focusing on 3*d*-transition metals (Sc-Zn) and 4*d*-transition metals (Y-Cd, except Mo). The $Mo_2B_2O_2$ surface provides four potential sites for SA adsorption. These include the position on top of an oxygen atom (O_{Top}), the position on top of molybdenum atom bonded to

two oxygen atoms (Mo_{Top}), and hollow sites coordinated with either two oxygen atoms ($Hollow_{2O}$) or four oxygen atoms ($Hollow_{4O}$), as shown in **Figure 4.2**.

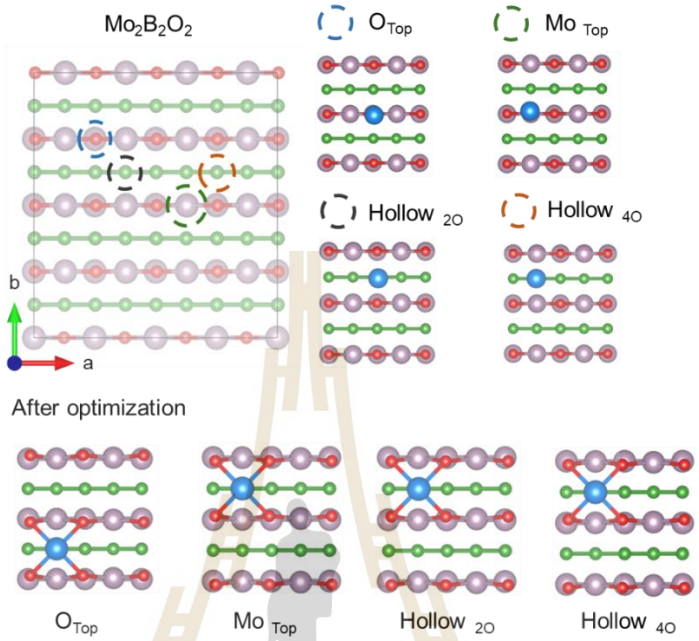

Figure 4.2 The possible configuration of the single transition metal atom on $Mo_2B_2O_2$ surface. Mo, B, O, and single transition metal (SA) atoms are represented by purple, green, red, and blue, respectively.

The most favorable configuration of SA-$Mo_2B_2O_2$ for each SA-$Mo_2B_2O_2$ system were identified by calculation single atom adsorption energy ($E_{ads,SA}$). A negative adsorption energy suggests that the SA adsorption on $Mo_2B_2O_2$ surface is energetically favorable. The adsorption energy was computed using the following equation (Lin et al., 2019).

$$E_{\mathrm{ads,SA}} = E_{\mathrm{SA-Mo_2B_2O_2}} - E_{\mathrm{Mo_2B_2O_2}} - E_{\mathrm{SA}} \qquad (4.1)$$

Where $E_{\mathrm{SA-Mo_2B_2O_2}}$, $E_{\mathrm{Mo_2B_2O_2}}$, and E_{SA} represent the total energy of SA-$Mo_2B_2O_2$, $Mo_2B_2O_2$, and an isolated single transition metal atom in vacuum (3*d*- and 4*d*-transition metals), respectively. Our results show that all SA prefer to adsorb at the hollow site with negative value of $E_{\mathrm{ads,SA}}$ (**Figure 4.3**).

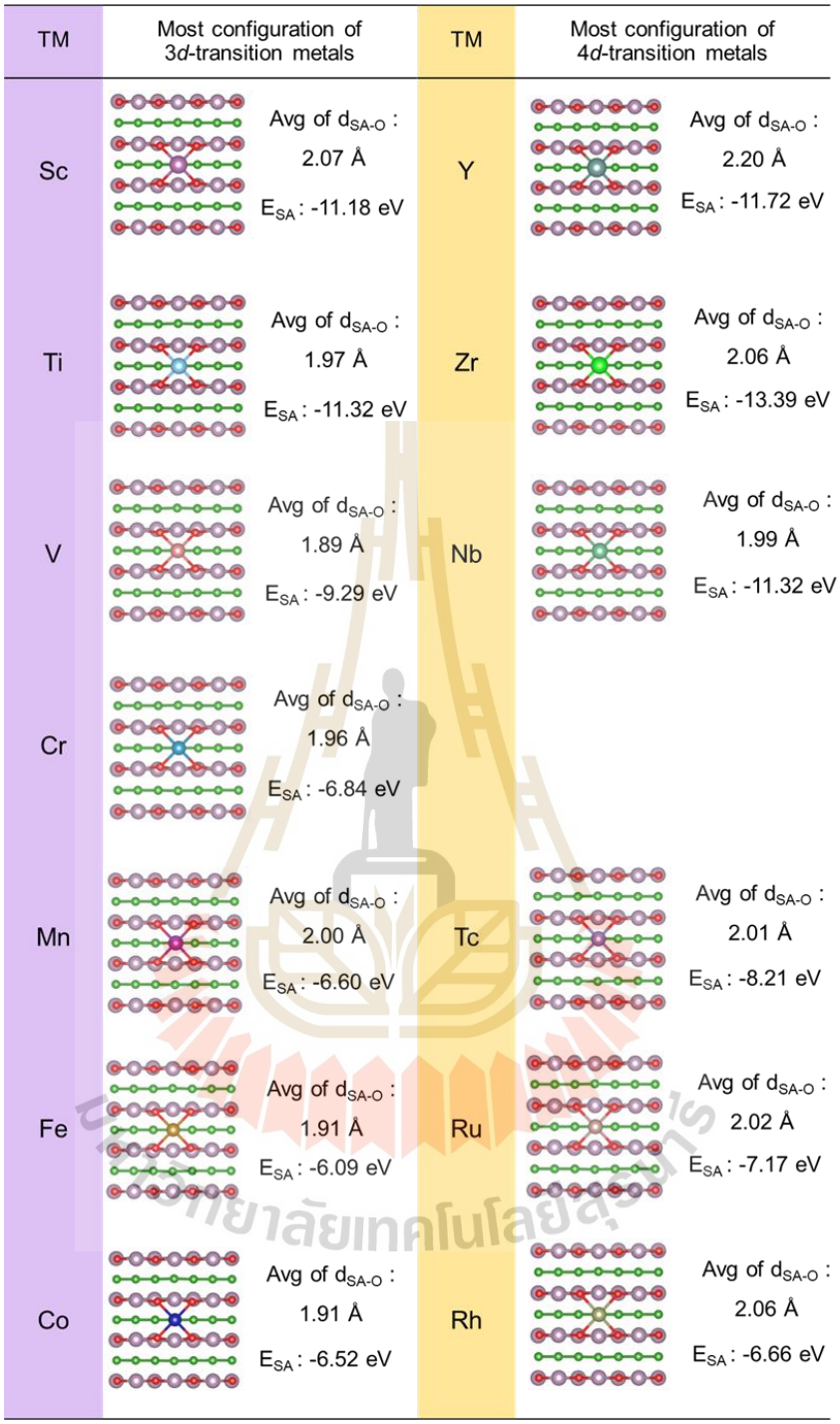

Figure 4.3 Configuration of SA-$Mo_2B_2O_2$, including 3*d*- and 4*d*-transtion metals. It exhibited average SA-O bond length of each substance (Avg of d_{SA-O}) and SA adsorption energy ($E_{ads,SA}$).

TM	Most configuration of 3*d*-transition metals	TM	Most configuration of 4*d*-transition metals
Ni	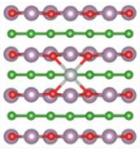 Avg of d_{SA-O} : 1.95 Å E_{SA} : -6.08 eV	Pd	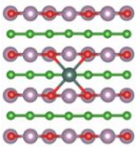 Avg of d_{SA-O} : 2.12 Å E_{SA} : -4.01 eV
Cu	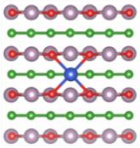 Avg of d_{SA-O} : 2.10 Å E_{SA} : -4.17 eV	Ag	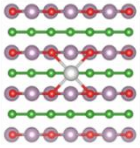 Avg of d_{SA-O} : 2.40 Å E_{SA} : -2.96 eV
Zn	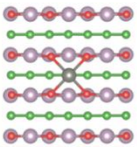 Avg of d_{SA-O} : 2.09 Å E_{SA-} : -2.84 eV	Cd	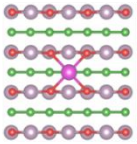 Avg of d_{SA-O} : 2.31 Å E_{SA-} : -2.38 eV

Figure 4.3 (Continued) Configuration of SA-$Mo_2B_2O_2$, including 3*d*- and 4*d*-transtion metals. It exhibited average SA-O bond length of each substance (Avg of d_{SA-O}) and SA adsorption energy ($E_{ads,SA}$).

When compared with atomic numbers, the SA adsorption energies show a strong correlation with atomic numbers within each period (**Figure 4.4**). The trend of single atom adsorption energy for each period shows more positive when number of d electrons increase, resulting weaker adsorption between SA and $Mo_2B_2O_2$ for late transition metals.

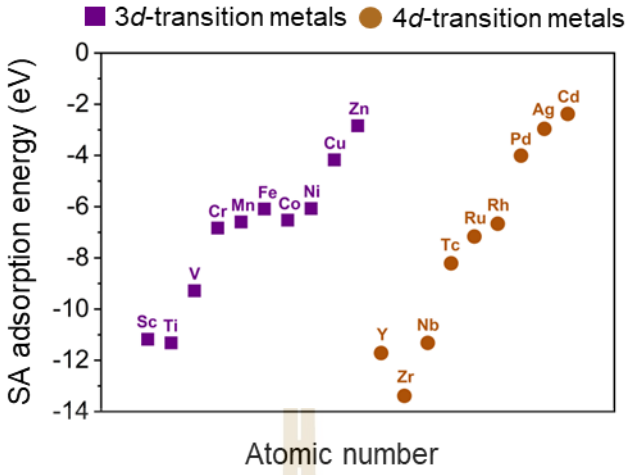

Figure 4.4 Correlation between SA adsorption energy and atomic number for 3*d*- and 4*d*-transition metals.

Additionally, a critical property for an effective single atom catalyst is its stability as single particle or atom, avoiding aggregation into clusters. Hence, we employed the climbing-image nudged elastic band (CI-NEB) method with five images to calculate the energy barrier for SA diffusion from one Hollow site to another Hollow site with the same symmetry. If a single atom (SA) requires high energy to diffuse from one hollow site to another on $Mo_2B_2O_2$, suggests that the SAs remain stable in their positions, reducing aggregation into metal clusters.

In this thesis, the diffusion path was calculated along [100] direction, as this path shows the lowest energy barrier for Li atom diffusion on the $Mo_2B_2O_2$ surface (**Figure 4.5a**). Therefore, we study SA diffusion along [100] direction, as example in V-$Mo_2B_2O_2$ system (**Figure 4.5b**). The calculated energy barriers for all SA-$Mo_2B_2O_2$ systems were shown in **Figure 4.5c**. Early and middle transition metals display high diffusion energy barriers, ranging from 1.00 to 3.50 eV (green region). In contrast, late transition metals, including Co to Zn (3*d*-transition metals) and Pd to Cd (4*d*-transition metals), exhibit lower diffusion energy barriers of less than 1.00 eV (red region). Consequently, early and middle transition metals demonstrate good stability as single atoms when decorated on the $Mo_2B_2O_2$ surface. Furthermore, the energies barrier for SA diffusion shows strong correlation with SA adsorption energies, as shown in **Figure 4.5d**. This relationship suggests that if $Mo_2B_2O_2$ can effectively bind with single

atoms, it minimizes the possibility of aggregation, making it suitable for multiple cycles of charge and discharge. The value of SA adsorption energy and energy of SA diffusion of each SA-$Mo_2B_2O_2$ were shown in **Table 4.1**

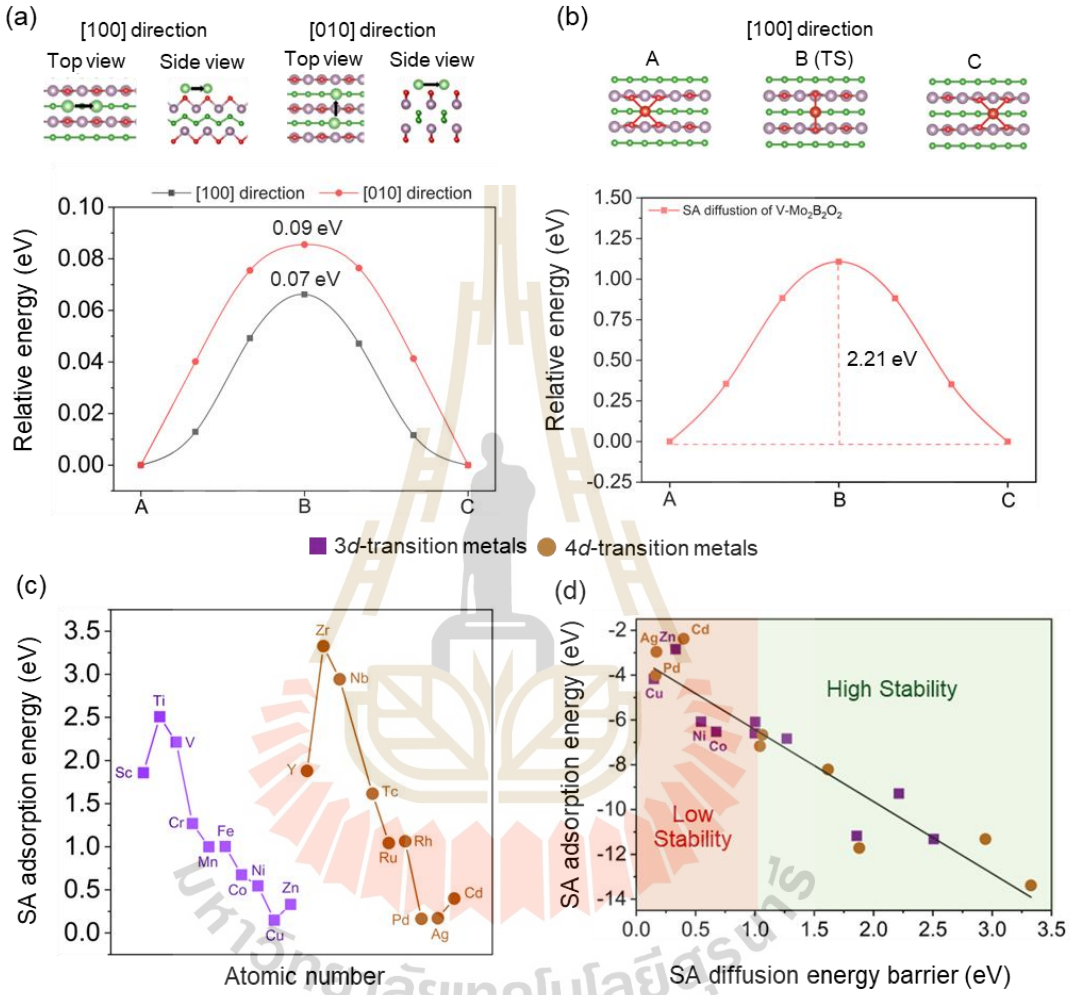

Figure 4.5 Potential energy profiles of (a) Li ion diffusion and (b) V ion diffusion on $Mo_2B_2O_2$. The relationship between the SA diffusion energy barrier and (c) atomic number and (d) SA adsorption energy for each period. In case of SA diffusion energy barrier compared with SA adsorption energy was separated by two regions, including green region (energy barrier more than 1.0 eV) and red region (energy barrier less than 1.0 eV).

Table 4.1. SA adsorption energy and SA diffusion energy barrier for each SA-$Mo_2B_2O_2$.

3d-TM	E_{SA} (eV)	$E_{SA\_diffuse}$ (eV)	*4d*-TM	E_{SA} (eV)	$E_{SA\_diffuse}$ (eV)
Sc	-11.18	1.86	Y	-11.72	1.88
Ti	-11.32	2.51	Zr	-13.39	3.33
V	-9.29	2.21	Nb	-11.32	2.94
Cr	-6.84	1.27			
Mn	-6.60	1.00	Tc	-8.21	1.62
Fe	-6.09	1.00	Ru	-7.17	1.04
Co	-6.52	0.67	Rh	-6.66	1.06
Ni	-6.08	0.55	Pd	-4.01	0.16
Cu	-4.17	0.15	Ag	-2.96	0.17
Zn	-2.84	0.33	Cd	-2.38	0.40

To understand the electronic properties when SA is absorbed, we calculated their projected density of states (PDOS). As shown in V- and Nb-$Mo_2B_2O_2$ example (**Figure 4.6**), they suggest that introduced SA show metallic character without an energy gap, like pristine $Mo_2B_2O_2$. The states from SA exhibit significant hybridization with O 2p states, corresponding to SA-O bond as shown in configuration. These additional states near the Fermi level, contributed by the SA, are likely to facilitate the redox reactions involved in the conversion of LiPSs during the charge-discharge cycles (Lin et al., 2019; Qiu et al., 2020).

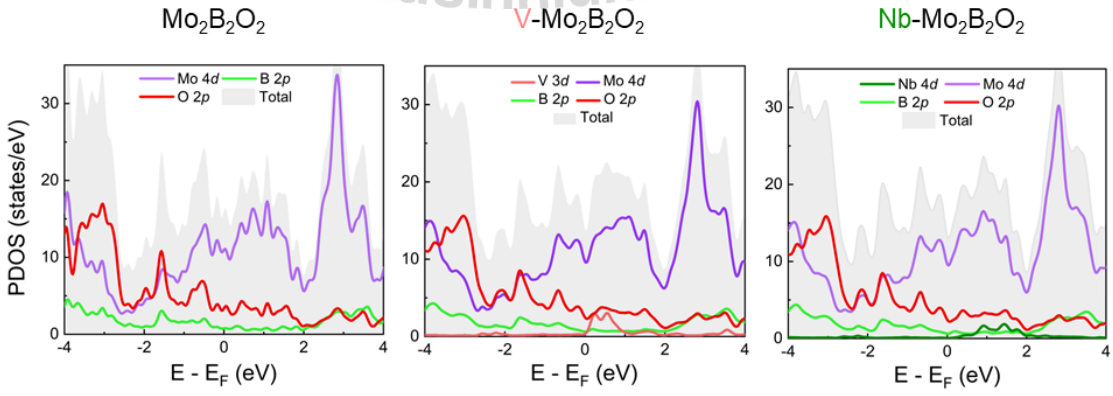

Figure 4.6 Projected density of states (PDOS) of $Mo_2B_2O_2$ and the example of SA-$Mo_2B_2O_2$ which are V- and Nb-$Mo_2B_2O_2$. Femi level is adjusted to 0 eV.

4.2 Key properties of single atoms affecting the stability of SA-$Mo_2B_2O_2$

As discussed in the previous section, we know that early transition metals, particularly the second element of each period (Ti- and Zr-$Mo_2B_2O_2$), exhibit strong SA adsorption, which helps prevent aggregation into metal clusters. However, the reasons why early transition metals show stronger SA adsorption than middle and late transition metals are still unclear. Additionally, it remains to be determined which specific properties of each SA are strongly correlated with SA adsorption energy, apart from atomic number. Understanding these relationships will provide deeper insights into the trends of SA adsorption energies. Furthermore, by suggesting the properties that most influence SA adsorption, we can apply this knowledge to select SAs that are stable when decorated on other support materials.

The properties of single atom which were used in this thesis were shown in **Table 4.2.** First step, we explored the relationship between each property and SA adsorption by Pearson correlation coefficients. As shown in **Figure 4.7-4.8**, the strength correlation of properties can be analyzed through the coefficient of determination. The values are between -1 and 1. Positive correlations are represented by blue, negative correlations by red-brown, and no correlation by white (0). A higher positive or negative value signifies a stronger correlation.

3*d*- and 4*d*-transition metals exhibit similar properties that show a strong correlation with SA adsorption energy, including atomic number, atomic weight and covalent radius of atom. Considering the properties of SA when decorated on $Mo_2B_2O_2$, the d-band center and SA charge transfer show strong correlation with SA adsorption energy for both 3*d*- and 4*d*-transition metals. Therefore, the atomic number or atomic weight of SA increases, the adsorption energy becomes less negative, indicating weaker adsorption. This is attributed to the increasing number of d-electrons in SA, leaving fewer vacant states in d-orbitals to accept electrons from oxygen, thereby weakening the SA-O bonds. Additionally, the strong correlation between the covalent radius and adsorption energy highlights the importance of the covalent character of SA-O bonds. Nevertheless, first elements of each period (Sc and Y) reveal weaker adsorption than second element due to large atomic(Han et al., 2021). Therefore, second

elements of each periods show strongest adsorption on $Mo_2B_2O_2$, including Ti and Zr atom.

Table 4.2 Description of properties to find correlation with SA adsorption energies.

Symbol	Description
N	Atomic number
A.W.	Atomic weight
R	Atomic radius
$R_{covalent}$	Covalent radius
EN	Electronegativity
EA	Electron affinity
d_{SA-O}	SA-O average bond length
Q_{SA}	Charge transfer of SA
$\boldsymbol{\varepsilon}_{d\uparrow}$,$\boldsymbol{\varepsilon}_{d\downarrow}$	d band center of SA in case of spin up and down
$\boldsymbol{\Phi}$	Work function

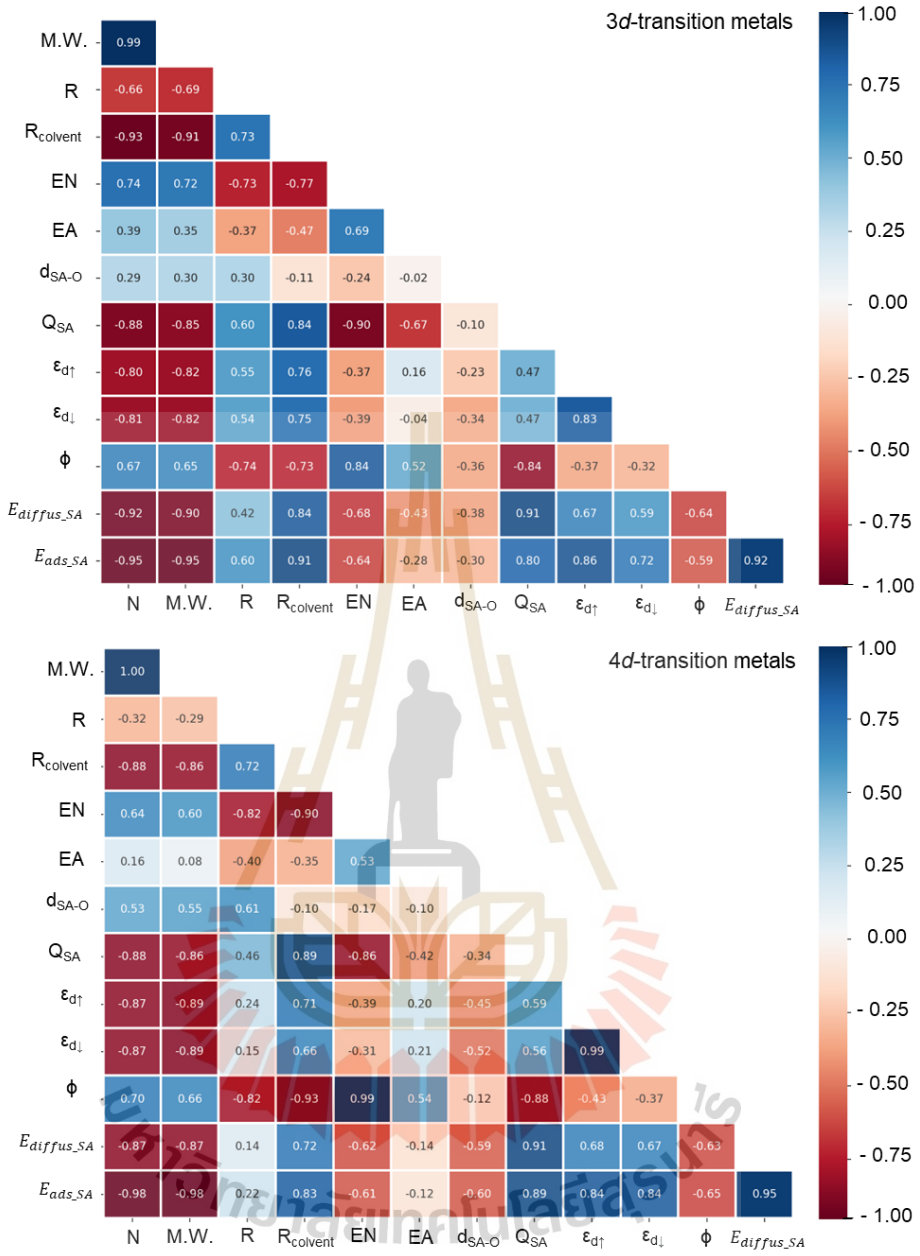

Figure 4.7 Heatmap of Pearson correlation coefficient matrix for SA adsorption energy of 3*d*- and 4*d*-transition metals.

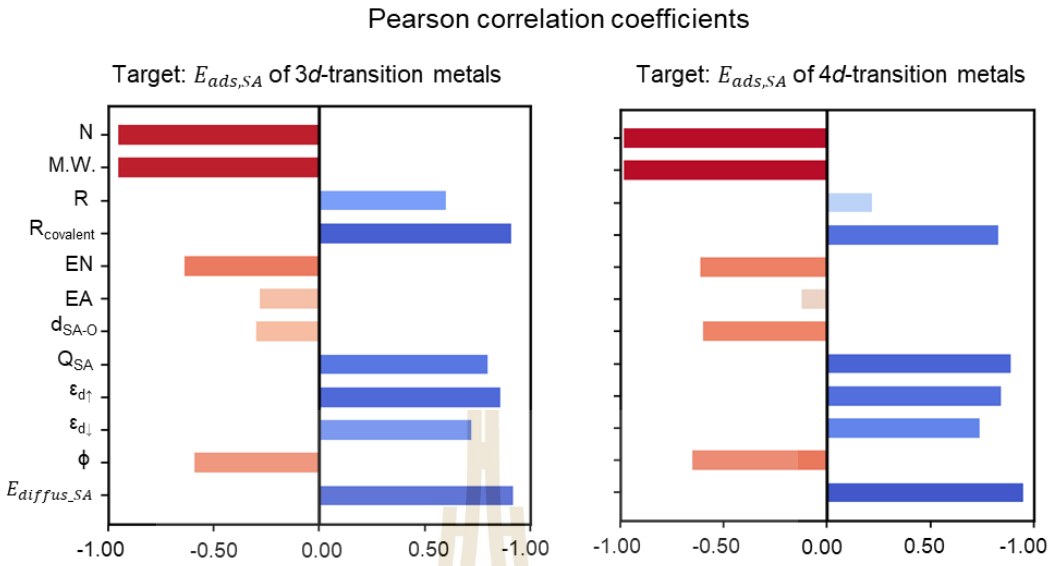

Figure 4.8 Feature correlation between properties and $E_{ads,SA}$ for each period. The x value represents the strength of correlation between pairs of variables, represented by Pearson correlation coefficients. A darker color suggests a stronger correlation with SA adsorption energy compared to other features.

In addition to employing Pearson correlation to explain the trend of SA adsorption, we used crystal orbital Hamilton population (COHP) to explain these. This analysis focuses on the bonding and antibonding states. We focused on the shortest SA-O bond to represent the other SA-O bonds. A shown in **Figure 4.9**, early transition metals within each period (Sc-V for 3*d*-transition metals and Y-Nb for 4*d*-transition metal) show only bonding states below the Fermi level. In contrast, as the number of d-electrons increases from middle to late transition metals, more electrons occupy antibonding states, resulting in the presence of antibonding states below the Fermi level. Consequently, early transition metals exhibit stronger SA adsorption on $Mo_2B_2O_2$.

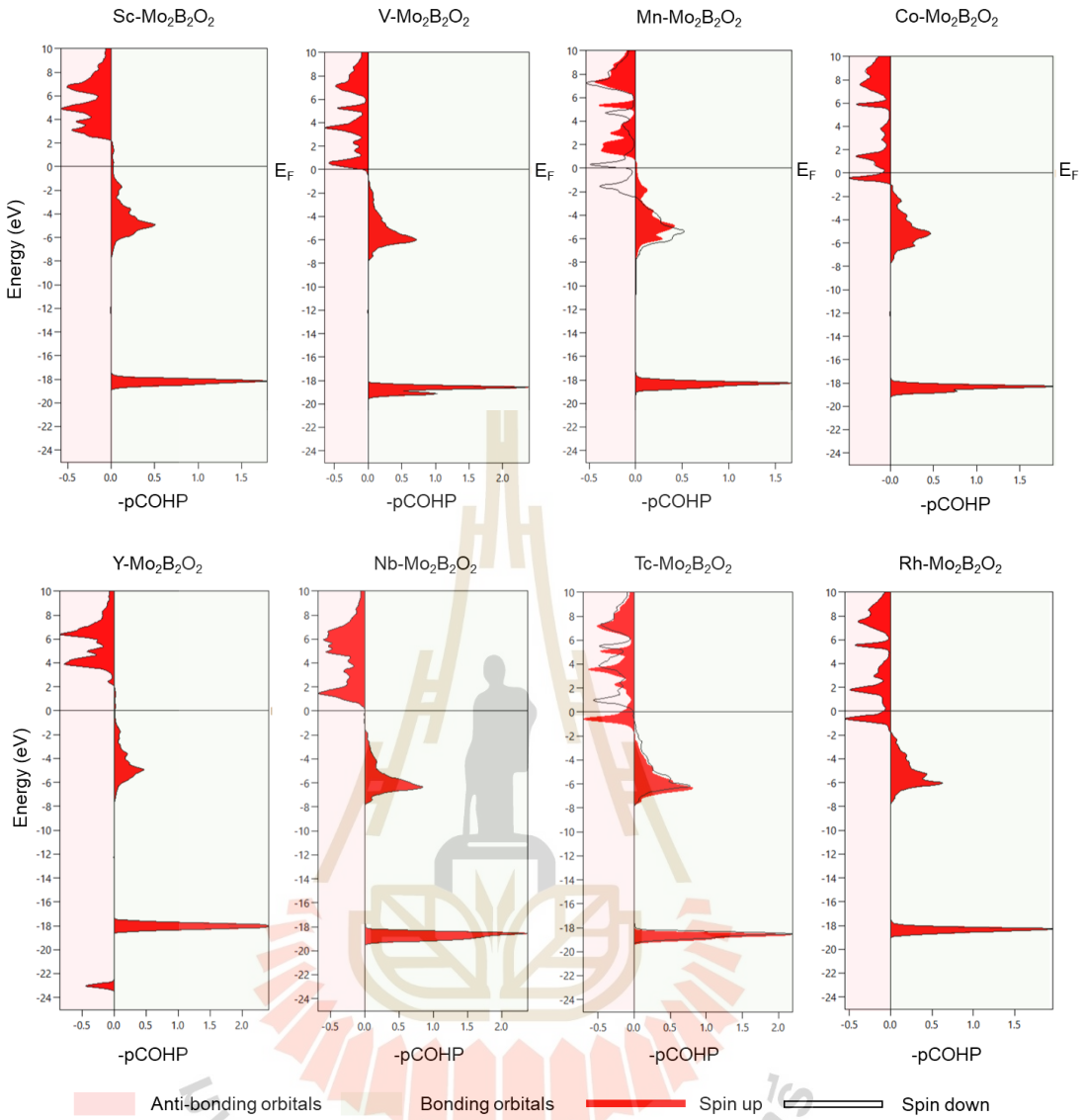

Figure 4.9 Crystal orbital Hamilton population (COHP) graph of the shortest SA-O bond for each example SA-$Mo_2B_2O_2$ from each period. Spin up and Spin down states were showed through red and black line. Green area suggests bonding orbital states, whereas antibonding orbital states were represented in red area.

4.3 References

Han, Z., Zhao, S., Xiao, J., Zhong, X., Sheng, J., Lv, W., Zhang, Q., Zhou, G., and Cheng, H.-M. (2021). Engineering d-p Orbital Hybridization in Single-Atom Metal-Embedded Three-Dimensional Electrodes for Li–S Batteries. *Advanced Materials, 33*(44), 2105947.

Li, B., Wu, Y., Li, N., Chen, X., Zeng, X., Arramel, Zhao, X., and Jiang, J. (2020). Single-Metal Atoms Supported on MBenes for Robust Electrochemical Hydrogen Evolution. *ACS Applied Materials & Interfaces, 12*(8), 9261-9267.

Lin, H., Jin, R., Wang, A., Zhu, S., and Li, H. (2019). Transition metal embedded C_2N with efficient polysulfide immobilization and catalytic oxidation for advanced lithium-sulfur batteries: A first principles study. *Ceramics International, 45*(14), 17996-18002.

Mou, Y., Wang, Y., Wan, J., Yao, G., Feng, C., Zhang, H., and Wang, Y. (2023). Rational design of 2D MBene-based bifunctional OER/ORR dual-metal atom catalysts: a DFT study. *Physical Chemistry Chemical Physics, 25*(42), 29135-29142.

Qiu, Y., Fan, L., Wang, M., Yin, X., Wu, X., Sun, X., Tian, D., Guan, B., Tang, D., and Zhang, N. (2020). Precise Synthesis of Fe-N_2 Sites with High Activity and Stability for Long-Life Lithium–Sulfur Batteries. *ACS Nano, 14*(11), 16105-16113.

Xiao, Y., Li, Y., Guo, Z., Tang, C., Sa, B., Miao, N., Zhou, J., and Sun, Z. (2021). Functionalized Mo_2B_2 MBenes: Promising anchoring and electrocatalysis materials for Lithium-Sulfur battery. *Applied Surface Science, 566*, 150634.

CHAPTER V
SUPPRESSION OF THE SHUTTLE EFFECT BY SINGLE ATOM DECORATION

In the previous chapter, we discussed that all 3*d*- and 4*d*-transition metals prefer to decorate $Mo_2B_2O_2$ surface, with early transition metals particularly favoring single particle. The presence of single atom does not disrupt the metallic properties of $Mo_2B_2O_2$ and instead, the additional states introduced by the single atoms near the Fermi level can enhance the redox reactions of LiPSs. To further understand the performance of each SA-$Mo_2B_2O_2$ as a cathode material for Li-S batteries, it is essential that the material strongly adsorbs LiPSs intermediates during SRR. The strong adsorption helps alleviate the shuttle effect and prevent capacity loss by reducing the dissolution of LiPSs. In this chapter, we first study the adsorption of LiPSs on each SA-$Mo_2B_2O_2$ without considering solvent effects (Section 5.1). We then extend our study by adding solvent molecules to examine how the presence of solvents influences the adsorption of LiPSs on both pristine and SA-$Mo_2B_2O_2$ (Section 5.2).

5.1 Effect of Single-Atom Decoration on LiPSs Adsorption Energy in $Mo_2B_2O_2$

To study LiPSs adsorption, SRR and Li_2S decomposition in chapter VI, we first determined the most stable adsorbed configurations, including S_8 and Li_2S_x (x = 1, 2, 4, 6, 8). Since S_8 and Li_2S are typically found in the solid state (Danner et al., 2019; Xiao et al., 2019), we modeled them as bulk structures. On the other hand, Li_2S_x intermediates with x = 1, 2, 4, 6, and 8 were treated as molecular systems. We examined both the bulk and molecular forms of Li_2S to simplify the study of Li_2S decomposition using the molecular form. The bulk structure was employed specifically when analyzing reactions within SRR. As shown in **Figure 5.1**, larger or liquid-phase LiPSs, such as Li_2S_8, Li_2S_6, and Li_2S_4, exhibit 3D spherical structures, whereas smaller or

solid-phase intermediates, including Li_2S_2 and Li_2S, favor non-linear configurations. Additionally, we study the bulk structure of S_8 (space group: Fddd) (Mikuriya et al., 2020) and Li_2S (space group: $Fm\bar{3}m$) (Xiao et al., 2019) in their solid phase. The geometric parameters of each structure are presented in **Table 5.1**.

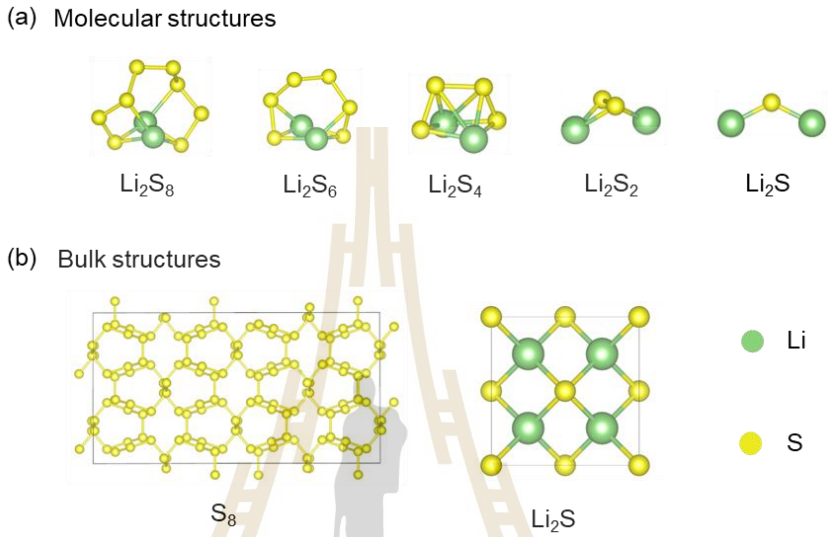

Figure 5.1 The relaxed (a) molecular structures of LiPS species and (b) bulk structures of S_8 and Li_2S.

Table 5.1 Geometric parameters of optimized molecular and bulk structure S_8/LiPS species.

Molecular/Bulk structure	S-S bond (Å)	Li-S bond (Å)
Li_2S_8	2.03-2.17	2.38-2.66
Li_2S_6	2.06-2.10	2.33-2.39
Li_2S_4	2.08-2.11	2.34-2.39
Li_2S_2	2.19	2.22
Li_2S	-	2.08
S_8 (bulk)	2.05-2.06	
Li_2S (bulk)		2.43

Among the LiPS intermediates, Li_2S_6 was chosen as a representative LiPS due to its generally weaker adsorption on cathode materials compared to other

intermediates (Boteju et al., 2023; Singsen et al., 2022). Additionally, Li_2S_6 is one of soluble LiPSs which prefer to dissolve into electrolyte. Enhancing ability of material to strongly bond with LI_2S_6 would indicate improved interactions with other LiPS intermediates, including S_8. Experimental studies also show that Li_2S_8 is less stable and quickly converts to other LiPS intermediates while Li_2S_6 consistently appears in cyclic voltammetry during charge-discharge cycles (Chen et al., 2015). Hence, we focused on studying the strong adsorption of LI_2S_6 on adsorption on pristine $Mo_2B_2O_2$ and SA-$Mo_2B_2O_2$.

First, the most stable configuration of Li_2S_6 adsorbed on each substrate were calculated and could be selected through Li_2S_6 adsorption energy $(E_{\mathrm{ads,Li_2S_6}^*})$ using the following equation (Lin et al., 2019),

$$E_{\mathrm{ads,Li_2S_6}^*} = E_{\mathrm{Li_2S_6+sub}} - E_{\mathrm{sub}} - E_{\mathrm{Li_2S_6}} \quad (5.1)$$

where $E_{\mathrm{Li_2S_6+sub}}$, E_{sub}, and $E_{\mathrm{Li_2S_6}}$ represent the total energy of the substrate with Li_2S_6 absorption, the bare substrate, and an isolated Li_2S_6 molecule, respectively. The most stable configuration of Li_2S_6 adsorbed on pristine and each SA-$Mo_2B_2O_2$ are presented in **Figure 5.2-5.4**. Additionally, the configurations of Li_2S_4 and Li_2S adsorbed on pristine and SA-$Mo_2B_2O_2$ are also presented in these figures for reference in other chapters. The adsorption of each LiPSs absorbed was shown in **Figure 5.5**.

Configuration	Li_2S_6	Li_2S_4	Li_2S_2	Li_2S
Pristine	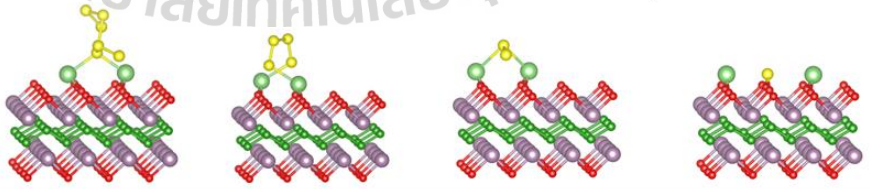			

Figure 5.2 Suitable adsorption configurations of Li_2S_6 on pristine $Mo_2B_2O_2$.

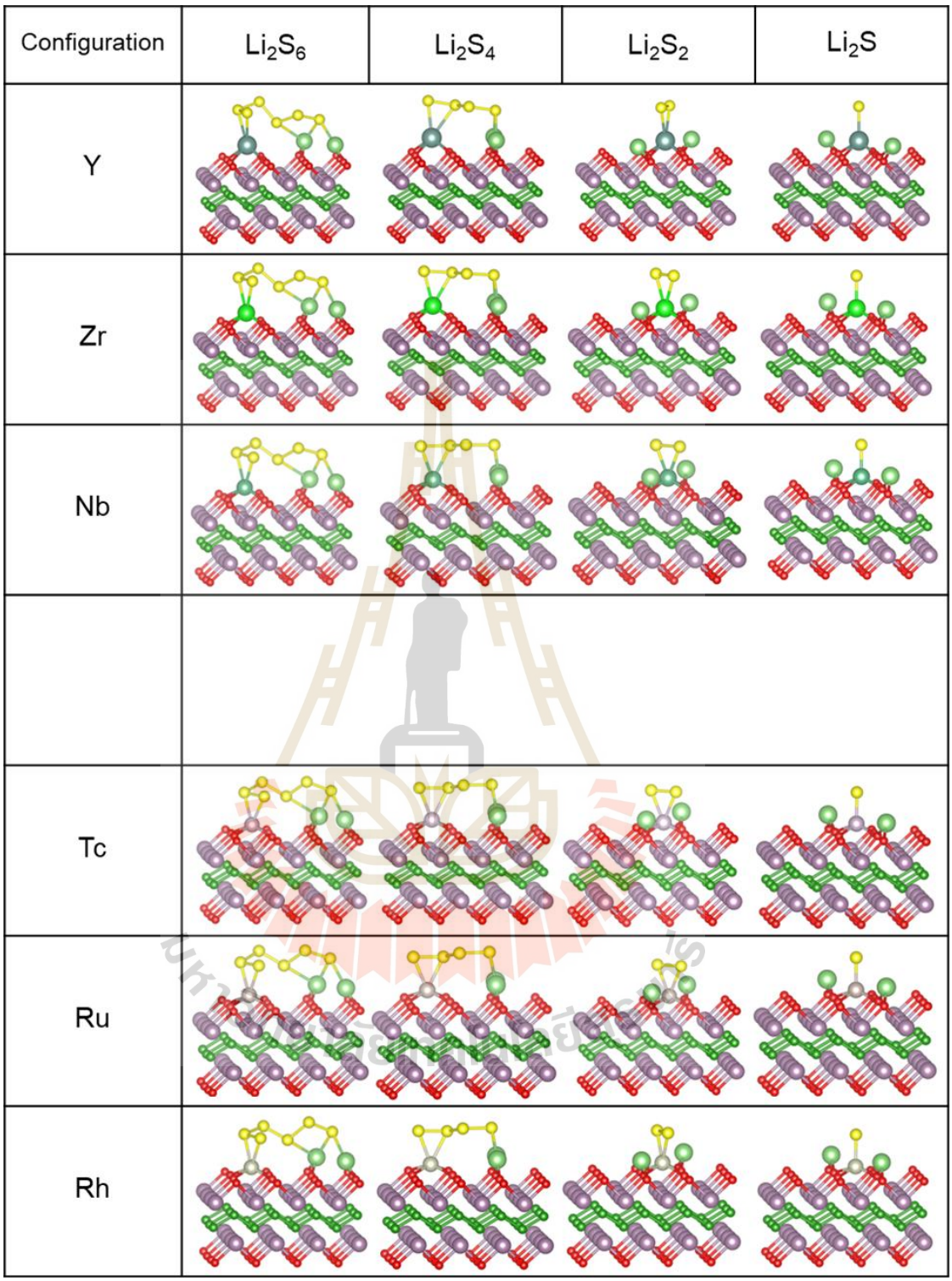

Figure 5.3 Suitable adsorption configurations of Li_2S_6 on SA-$Mo_2B_2O_2$ of 3*d*-transition metals.

Configuration	Li_2S_6	Li_2S_4	Li_2S_2	Li_2S
Pd	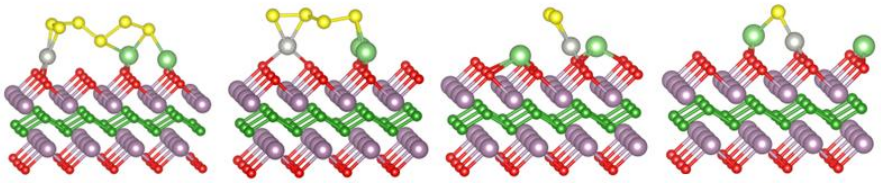			
Ag	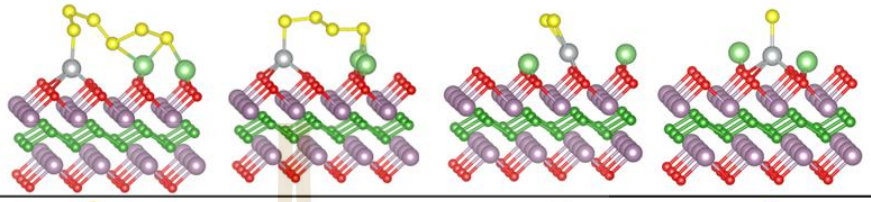			
Cd	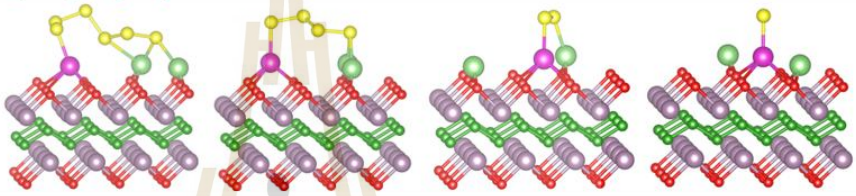			

Figure 5.3 (Continued) Suitable adsorption configurations of Li_2S_6 on SA-$Mo_2B_2O_2$ of 3*d*-transition metals.

Configuration	Li_2S_6	Li_2S_4	Li_2S_2	Li_2S
Y	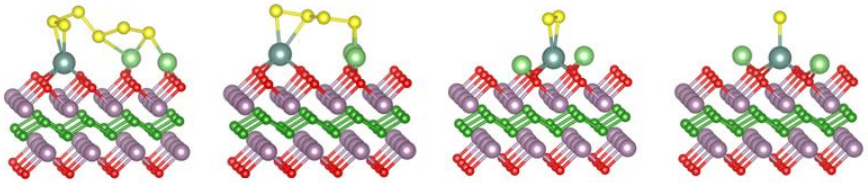			
Zr	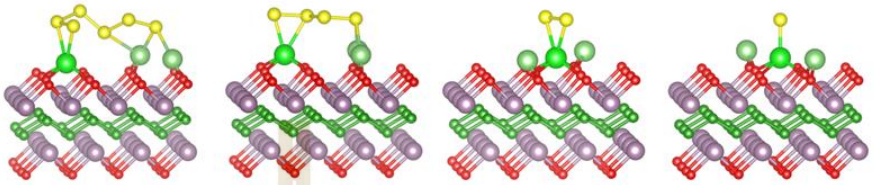			
Nb	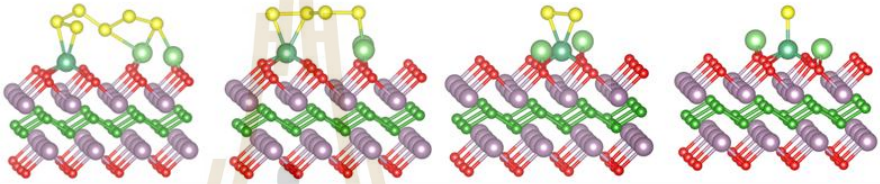			
Tc	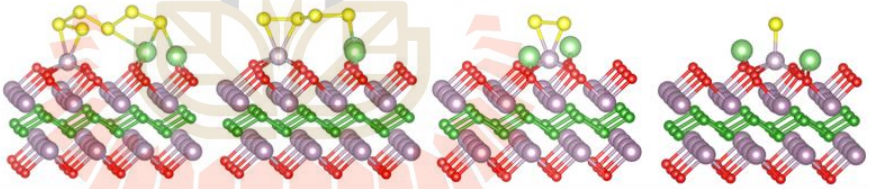			
Ru	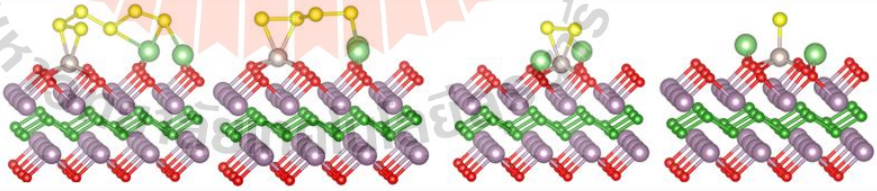			
Rh	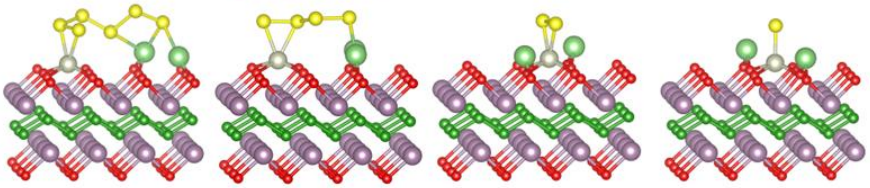			

Figure 5.4 Suitable adsorption configurations of Li_2S_6 on SA-$Mo_2B_2O_2$ of 4*d*-transition metals.

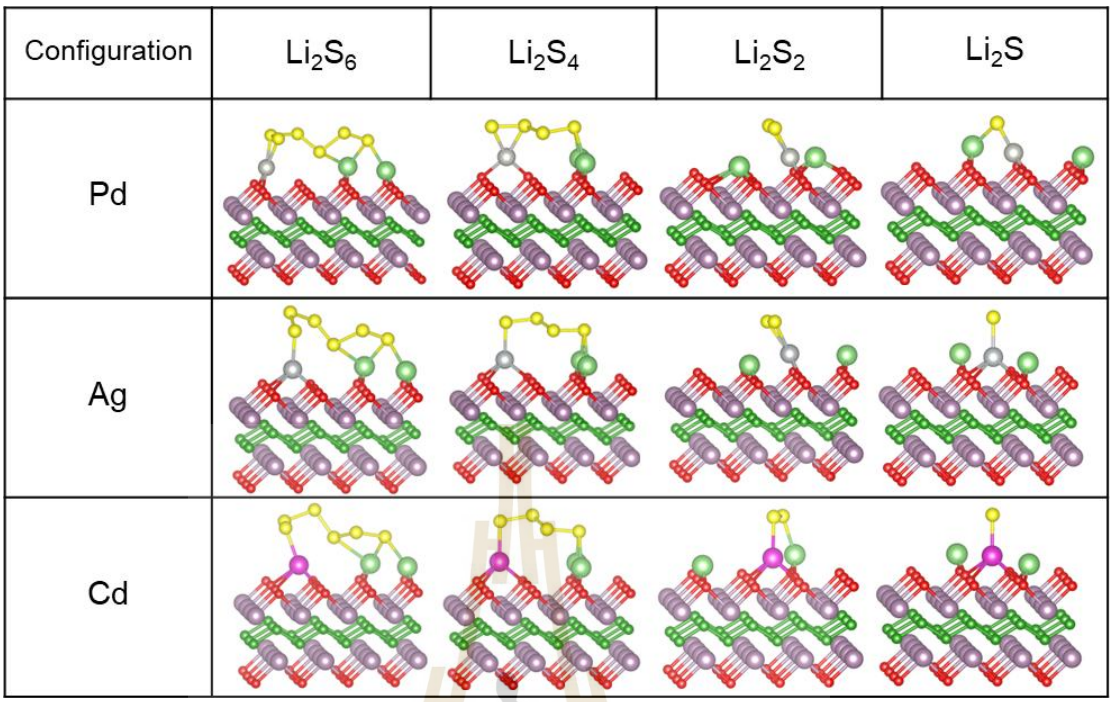

Figure 5.4 (Continued) Suitable adsorption configurations of Li_2S_6 on SA-$Mo_2B_2O_2$ of 4*d*-transition metals.

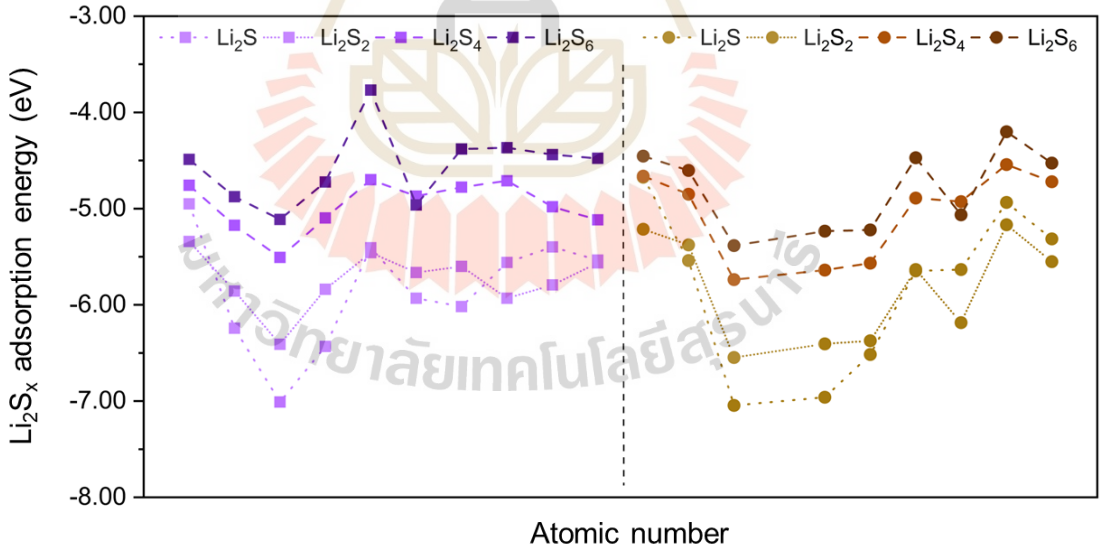

Figure 5.5 The Li_2S_x adsorption energy of 3*d*- and 4*d*-transition metals, including Li_2S, Li_2S_2, Li_2S_4, and Li_2S_6.

To explore the advantages of SA decorated, the calculation reveals that the presence of SA significantly enhances Li_2S_6 adsorption, leading to stronger interactions between Li_2S_6 and the substrate. This is evident from Li_2S_6 adsorption energies of most

SA-$Mo_2B_2O_2$ configurations, which range from -3.77 eV to -5.23 eV, compared to -3.86 eV for pristine $Mo_2B_2O_2$, as shown in **Figure 5.6**. The original strong adsorption can be explained by additive interaction between SA and sulfur atom of Li_2S_6 molecule. In contrast, for pristine $Mo_2B_2O_2$, Li_2S_6 referentially adopts a vertical planar configuration, interacting through Li of Li_2S_6 and O atoms of $Mo_2B_2O_2$ surface.

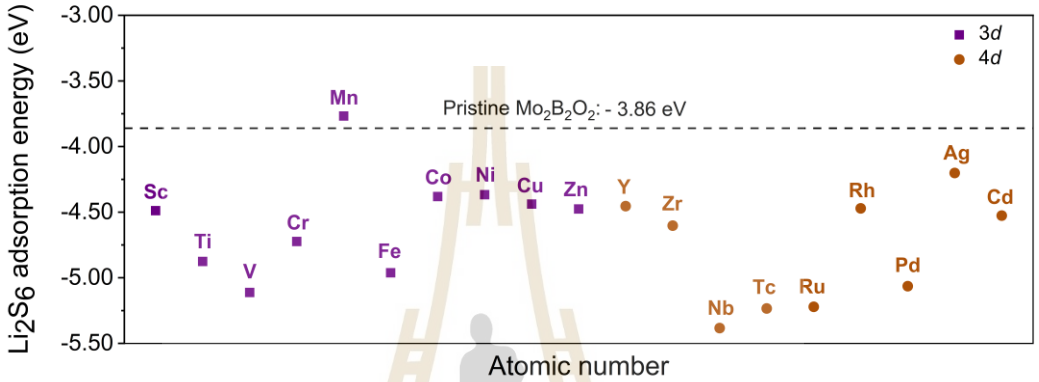

Figure 5.6 Li_2S_6 adsorption energies of various SA-$Mo_2B_2O_2$ compared to the pristine $Mo_2B_2O_2$ (dashed line).

The strong interaction between the substrate and Li_2S_6 molecule disrupts its original 3D spherical structure in pristine $Mo_2B_2O_2$. In contrast, when considering SA-$Mo_2B_2O_2$, Li_2S_6 molecule undergoes a significant structural transformation, shifting from a spherical configuration to an almost linear chain. The decomposition of Li_2S_6 facilitates the breakdown of long polysulfide chains into shorter sulfur chains, supported by the elongation of S-S bonds (Li et al., 2020). A similar elongation effect is suggested when Li_2S_4 is adsorbed onto SA-$Mo_2B_2O_2$. These structural changes are detailed in **Figure 5.7** and summarized in **Tables 5.2** and **5.3**. The presence of SA not only enhances LiPS adsorption and reduces their dissolution into the electrolyte but also promotes the conversion of larger LiPS molecules into smaller ones, further contributing to the improved performance of the system.

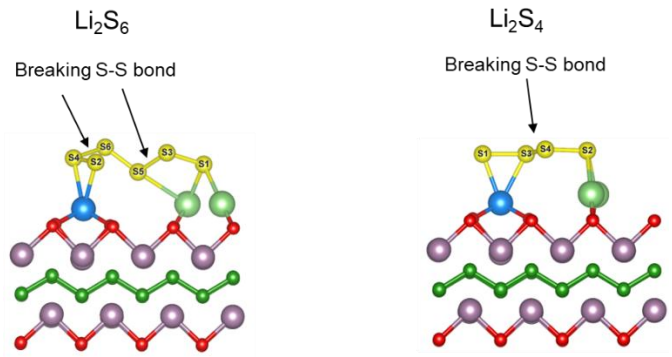

Figure 5.7 S-S bond breaking positions for Li_2S_6 and Li_2S_4 adsorption on SA-$Mo_2B_2O_2$, with numbered sulfur positions.

Table 5.2 Bond lengths of S-S at different positions for Li_2S_6 and Li_2S_4 adsorption on SA-$Mo_2B_2O_2$ (3*d*-transition metals).

TM	Li_2S_6				Li_2S_4			
	S2-S4	S4-S6	S6-S5	S5-S3	S3-S1	S1-S3	S3-S4	S4-S2
Sc	2.02	2.16	2.00	2.13	1.98	2.01	2.14	1.98
Ti	2.01	2.20	1.98	2.14	1.98	2.02	2.16	1.98
V	2.00	2.28	1.96	2.16	1.99	2.02	2.15	2.00
Cr	1.98	2.24	1.97	2.15	1.98	1.99	2.15	2.00
Mn	1.97	2.31	1.96	2.17	1.99	1.98	2.11	2.00
Fe	1.99	2.23	1.97	2.15	1.98	1.99	2.10	1.99
Co	1.96	2.27	1.97	2.15	1.98	1.96	2.09	2.00
Ni	1.94	2.25	1.97	2.18	1.98	1.96	2.09	1.99
Cu	1.95	2.22	1.98	2.18	1.98	1.98	2.07	1.98
Zn	1.98	2.22	1.97	2.18	1.97	2.02	2.09	1.98

Table 5.3 Bond lengths of S-S at different positions for Li_2S_6 and Li_2S_4 adsorption on SA-$Mo_2B_2O_2$ (4*d*-transition metals).

TM	Li_2S_6				Li_2S_4			
	S2-S4	S4-S6	S6-S5	S5-S3	S3-S1	S1-S3	S3-S4	S4-S2
Y	2.03	2.14	2.04	2.12	2.00	2.01	2.14	1.99
Zr	2.03	2.18	2.00	2.14	1.98	2.03	2.17	1.98
Nb	2.03	2.24	1.97	2.15	2.00	2.04	2.17	2.00
Tc	2.01	2.33	1.96	2.15	1.99	2.01	2.13	2.01
Ru	1.98	2.27	1.97	2.15	1.98	1.99	2.13	2.000
Rh	1.95	2.24	1.98	2.15	1.99	1.97	2.10	2.00
Pd	1.98	2.21	2.00	2.14	1.99	1.98	2.14	2.00
Ag	1.94	2.22	1.98	2.16	1.99	1.96	2.09	1.98
Cd	2.04	2.05	2.07	2.10	1.98	2.00	2.09	1.99

To understand bonding characteristics of pristine and SA-$Mo_2B_2O_2$ when Li_2S_6 is adsorbed, we employed PDOS to explain the bonding characteristics, which are presented in **Figure 5.8.** The results suggest that both pristine and SA-$Mo_2B_2O_2$, such as V- and Nb-$Mo_2B_2O_2$, retain their metallic properties after Li_2S_6 adsorption. This metallic nature facilitates efficient electron transfer within the substrate, helping to alleviate sluggish kinetics. When focusing on the electronic states of Li_2S_6 adsorbed on pristine. A small overlap is observed between the Li 1s states of Li_2S_6 and the O 2p and S 2p states, suggesting the formation of covalent bonds. Remarkably, the introduction of SA creates additional electronic states that overlap with the O and S states, leading to an increased number of covalent bonds between Li_2S_6 and the substrate.

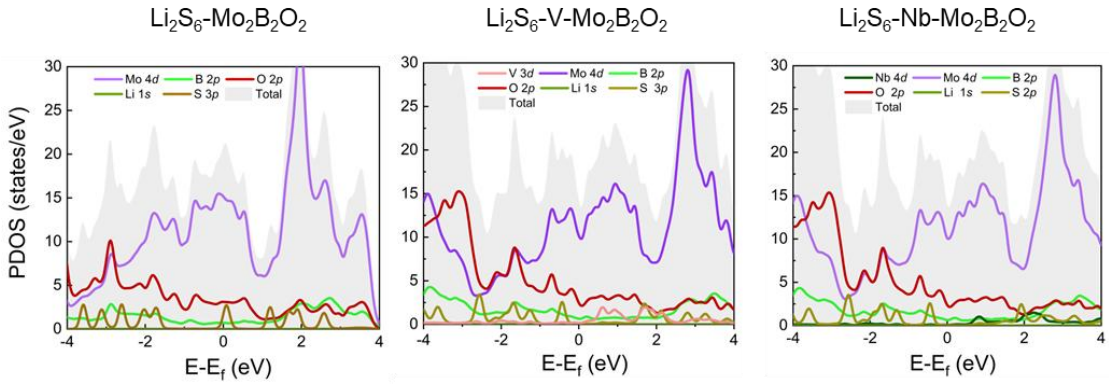

Figure 5.8 Projected density of states (PDOS) of Li_2S_6 adsorbed on $Mo_2B_2O_2$ and the example of SA-$Mo_2B_2O_2$ which are V- and Nb-$Mo_2B_2O_2$. Femi level is adjusted to 0 eV.

We further analyzed the charge distribution of Li_2S_6 and substrate, as shown in **Figure 5.9** and detailed in **Table 5.4**. The calculations revealed that Li_2S_6 molecule exhibits positive charge when adsorbed on both pristine and SA-$Mo_2B_2O_2$, suggesting electron transfer from Li_2S_6 to the substrate. Although the pristine $Mo_2B_2O_2$ shows a slightly higher positive charge on Li_2S_6 (+1.82 e^-) compared to all SA-$Mo_2B_2O_2$, the stronger adsorption on SA-$Mo_2B_2O_2$ is primarily attributed to the additional bonding interactions between the SA and the sulfur atoms of Li_2S_6. The charge of SA in each period becomes more negative as the atomic number increases, corresponding to higher electronegativity. This increased electronegativity makes the atom less likely to donate electrons.

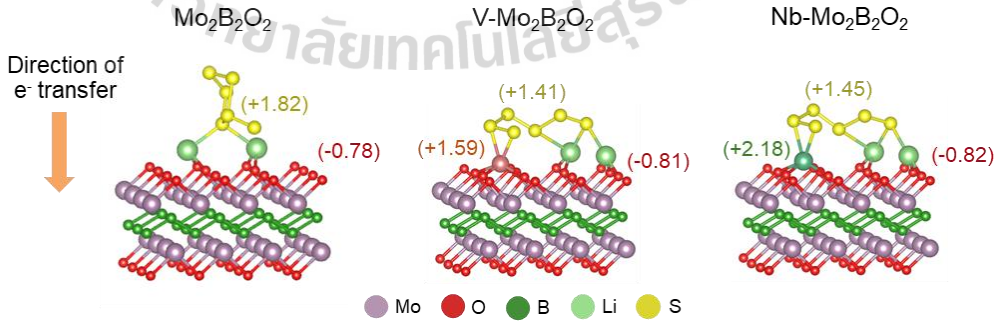

Figure 5.9 The most stable configuration and degree of charge transfer of Li_2S_6 molecule adsorbed on pristine $Mo_2B_2O_2$, V- and Nb-$Mo_2B_2O_2$.

Table 5.4 Charge of Li_2S_6, SA, and surface oxygen atom (O) in pristine and SA-$Mo_2B_2O_2$.

TM	Charges			TM	Charges		
	Li_2S_6	SA	O		Li_2S_6	SA	O
Sc	+1.20	+1.68	-0.81	-	+1.82	-	-0.98
Ti	+1.31	+1.70	-0.81	Y	+0.92	+2.08	-0.82
V	+1.41	+1.59	-0.81	Zr	+1.07	+2.27	-0.82
Cr	+1.49	+1.40	-0.81	Nb	+1.45	+2.18	-0.82
Mn	+1.57	+1.29	-0.81	Tc	+1.51	+1.39	-0.81
Fe	+1.50	+1.26	-0.81	Ru	+1.62	+1.05	-0.80
Co	+1.68	+0.92	-0.80	Rh	+1.69	+0.85	-0.80
Ni	+1.58	+0.87	-0.80	Pd	+1.65	+0.56	-0.79
Cu	+1.57	+0.79	-0.80	Ag	+1.57	+0.66	-0.80
Zn	+1.42	+1.13	-0.80	Cd	+1.37	+1.09	-0.80

Figure 5.6 shows the trends in Li_2S_6 adsorption strength for 3*d*- and 4*d*-transition metals. For both groups, adsorption strength initially increases with atomic number for the first three elements. However, different trends emerge beyond the third element. In the case of 3*d*-transition metals, adsorption strength decreases after the third element but increases again at Fe, with Co to Zn exhibiting relatively stable adsorption strengths. For 4*d*-transition metals, the trend is more straightforward, with adsorption strength steadily decreasing as the atomic number increases. This variation motivated us to explore the underlying reasons for this complexity, as discussed in chapter VI. Notably, single atoms with a d^3 electron configuration, including V- and Nb-$Mo_2B_2O_2$, suggest the strongest Li_2S_6 adsorption energies within their respective periods. These findings suggest that V- and Nb-$Mo_2B_2O_2$ cathode materials could effectively alleviate LiPS dissolution into the electrolyte while promoting the conversion of larger LiPS molecules into smaller ones.

5.2 LiPSs Adsorption Energy When Surrounded by Solvent Molecules

The dissolution of large LiPSs (Li_2S_8, Li_2S_6, and Li_2S_4) into electrolyte is a significant challenge contributing to the shuttle effect in Li-S batteries. Enhancing the adsorption of LiPSs onto the cathode is a potential solution to this issue. However, the influence of the electrolyte environment was not addressed in this thesis. To further study this task, we extended our study to explore how SA alleviates the dissolution of LiPSs into the electrolyte.

To study the influence of electrolytes on LiPS adsorption and dissolution, we carried out AIMD simulations of Li_2S_6 adsorption on SA-$Mo_2B_2O_2$ in the presence of electrolyte molecules, comparing these results to pristine $Mo_2B_2O_2$. We selected V- and Nb-$Mo_2B_2O_2$ to represent SA-$Mo_2B_2O_2$, as they exhibit the strongest Li_2S_6 adsorption energies and potentially suppress LiPS dissolution. For electrolyte, it usually contains a mixture of solvents along with Li-salts and other additives. In this work, the common solvent was simplified study by using either pure 1,2-dimenthoxyethane (DME) and 1,3-dioxolane (DOL), which are ether-based solvents (Choi et al., 2008; Kim et al., 2004; Scheers et al., 2014). The initial models are shown in **Figure 5.10**. The number of solvent molecules introduced into the vacuum region was determined based on their liquid densities: 1.06 g/cm³ for DOL and 0.87 g/cm³ for DME at room temperature. Helium atoms were employed to restrict the motion of solvent molecules along the z-axis.

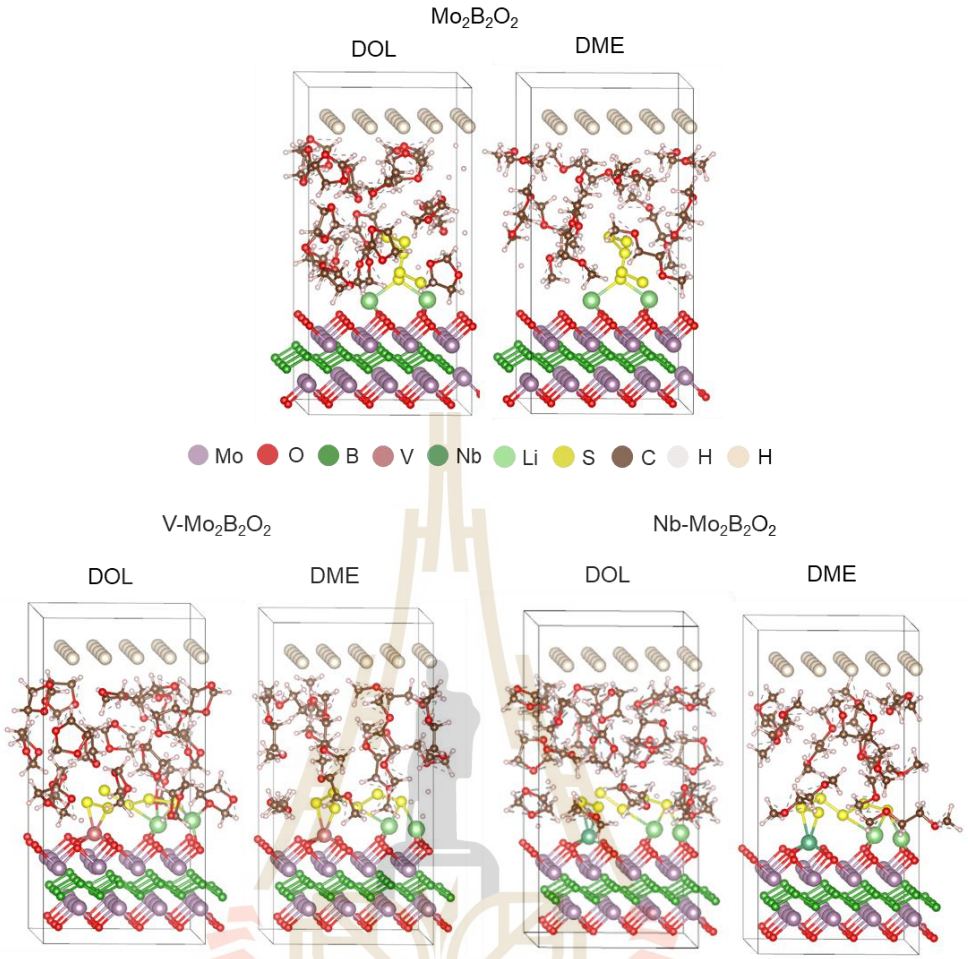

Figure 5.10 Initial configurations of pristine, V-, and Nb-$Mo_2B_2O_2$ surrounded by DOL and DME molecules before AIMD simulation.

AIMD simulations (**Figure 5.11**) reveal that both DME and DOL molecules coordinate with Li atoms of Li_2S_6 through their O atoms. Furthermore, the weakening of Li-S bonds in Li_2S_6 results in bond dissociation, resulting in a remaining polysulfide. This behavior is suggested in both pristine and SA-$Mo_2B_2O_2$ systems.

In pristine $Mo_2B_2O_2$ systems, the breaking of Li-S bonds caused by coordination with solvent molecules leads to the breakdown of polysulfides into smaller molecules, such as S_2, in both DME and DOL solvents. However, these polysulfides lack interaction with the substrate and subsequently dissolve into the electrolyte. Hence, pristine $Mo_2B_2O_2$ may be ineffective in addressing the shuttle effect. In contrast, polysulfide remains strongly bound to SA site of V- and Nb-$Mo_2B_2O_2$ even after the Li-S bonds are weakened by interactions with either DME or DOL. Therefore, the SA decoration

effectively anchors large LiPSs at the SA site, preventing their dissolution and significantly alleviating the shuttle effect.

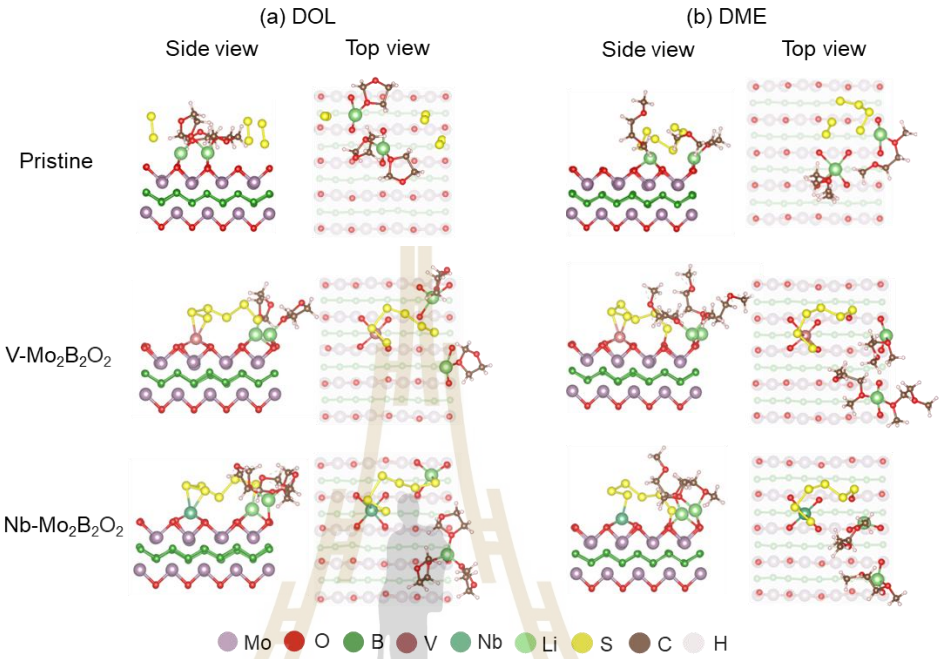

Figure 5.11 Low-energy configurations of (a) DOL- and (b) DME-solvated Li_2S_6. All configurations were calculated using AIMD with a time step of 1 fs for 10 ps.

5.3 References

Boteju, T., Abraham, A. M., Ponnurangam, S., and Thangadurai, V. (2023). Theoretical Study on the Role of Solvents in Lithium Polysulfide Anchoring on Vanadium Disulfide Facets for Lithium–Sulfur Batteries. *The Journal of Physical Chemistry C, 127*(9), 4416-4424.

Chen, J.-J., Yuan, R.-M., Feng, J.-M., Zhang, Q., Huang, J.-X., Fu, G., Zheng, M.-S., Ren, B., and Dong, Q.-F. (2015). Conductive Lewis Base Matrix to Recover the Missing Link of Li2S8 during the Sulfur Redox Cycle in Li–S Battery. *Chemistry of Materials, 27*(6), 2048-2055.

Choi, J.-W., Cheruvally, G., Kim, D.-S., Ahn, J.-H., Kim, K.-W., and Ahn, H.-J. (2008). Rechargeable lithium/sulfur battery with liquid electrolytes containing toluene as additive. *Journal of Power Sources, 183*(1), 441-445.

Danner, T., and Latz, A. (2019). On the influence of nucleation and growth of S8 and Li2S in lithium-sulfur batteries. *Electrochimica Acta, 322*, 134719.

Kim, S., Jung, Y., and Lim, H. S. (2004). The effect of solvent component on the discharge performance of Lithium–sulfur cell containing various organic electrolytes. *Electrochimica Acta, 50*(2), 889-892.

Li, H., Ma, S., Li, J., Liu, F., Zhou, H., Huang, Z., Jiao, S., and Kuang, Y. (2020). Altering the reaction mechanism to eliminate the shuttle effect in lithium-sulfur batteries. *Energy Storage Materials, 26*, 203-212.

Lin, H., Jin, R., Wang, A., Zhu, S., and Li, H. (2019). Transition metal embedded C2N with efficient polysulfide immobilization and catalytic oxidation for advanced lithium-sulfur batteries: A first principles study. *Ceramics International, 45*(14), 17996-18002.

Mikuriya, M., Taniguchi, K., Koyama, Y., Watanabe, H., Yoshioka, D., Mitsuhashi, R., and Asato, E. (2020). Crystal Structure of S_8 Molecule from Thiourea. *X-ray Structure Analysis Online, 36*, 1-2.

Scheers, J., Fantini, S., and Johansson, P. (2014). A review of electrolytes for lithium–sulphur batteries. *Journal of Power Sources, 255*, 204-218.

Singsen, S., Fongkaew, I., Hirunsit, P., and Suthirakun, S. (2022). Suppressing Polysulfides Shuttling and Promoting Sulfur Utilization via Transition Metal and Nitrogen Co-

Doping on Graphdiyne Cathodes of Lithium-Sulfur Batteries: A First-Principles Modeling. *ACS Applied Energy Materials, 5*(8), 9722-9732.

Xiao, J., Zhou, G., Chen, H., Feng, X., Legut, D., Fan, Y., Wang, T., Cui, Y., and Zhang, Q. (2019). Elaboration of Aggregated Polysulfide Phases: From Molecules to Large Clusters and Solid Phases. *Nano Letters, 19*(10), 7487-7493.

CHAPTER VI
TRANSITION METAL TYPES AND THEIR EFFECT ON LiPSs ADSORPTION

From our study of Lips adsorption on each SA-$Mo_2B_2O_2$, 3*d*- and 4*d*- transition suggest a similar trend. Among these, V- and Nb-$Mo_2B_2O_2$ show the strongest adsorption within their respective periods. However, for 3*d*-transition metals, the Li_2S_6 adsorption strength initially decreases with increasing atomic number, but increases again at Fe, with Co to Zn exhibiting relatively consistent adsorption strengths. In contrast, the 4*d*-transition metals show a steady decrease in adsorption strength as the atomic number increases. Understanding these variations remains a key challenge. Additionally, the reason why the third transition metal of each period shows the strongest adsorption compared to other transition metals is not yet clear. To suggest and better understand these, we employed three methods to support this trend, including analyzing the strength of correlation with Li_2S_6 adsorption (section 6.1), electron filling in d-p hybridization, and selective orbital coupling

6.1 Study Properties of SA-$Mo_2B_2O_2$ Affecting Lips Adsorption

Although we knew that the third transition metals exhibit the strongest Li_2S_6 adsorption among both 3*d*- and 4*d*-transition metals, it remains unclear which specific properties of SA or SA-$Mo_2B_2O_2$ cathode material play the most critical role in determining this strong adsorption. To suggest the key properties influencing Li_2S_6 adsorption, we analyzed Pearson correlation coefficients to determine which factors correlate most strongly with adsorption strength. In this thesis, 3*d*- and 4*d*-transition metals were analyzed separately to account for the differences in their atomic properties. Additionally, the properties examined in this work were grouped into two types: electronic (green region) and geometric properties (red region), as show in **Table 6.1.** Geometric properties were included because the symmetry of the SA-O bond

significantly affects Li_2S_6 adsorption. In contrast to the SA adsorption study, which examines $Mo_2B_2O_2$ as the base structure before the SA is adsorbed.

Table 6.1 Description of properties to find correlation, including electronic properties (green region) and geometric properties (red region).

Symbol	Description
N	Atomic number
A.W.	Atomic weight
EN	Electronegativity
EA	Electron affinity
Q_{SA}	Charge transfer of SA
$\varepsilon_{d\uparrow}$,$\varepsilon_{d\downarrow}$	d band center of SA in case of spin up and down
Φ	Work function
R	Atomic radius
$R_{covalent}$	Covalent radius
$d_{SA\text{-}O}$	SA-O average bond length

Beside Li_2S_6 adsorption energy ($E_{\mathrm{ads,Li_2S_6{}^*}}$) which is main target in this section, it is also important to consider the structural distortion of Li_2S_6 caused by its strong interaction with SA-$Mo_2B_2O_2$. Therefore, we examined additional targets, including the distortion energies of both Li_2S_6 ($E_{\mathrm{dis-Li_2S_x}}$) and substrate ($E_{\mathrm{dis-sub}}$). These energies were calculated using the following equations (Singsen et al., 2022):

$$E_{dis-Li_2S_x} = E_{Li_2S_6^*} - E_{\mathrm{Li_2S_6}} \tag{6.1}$$

$$E_{\mathrm{dis-sub}} = E_{sub\_distortion} - E_{sub} \tag{6.2}$$

where $E_{Li_2S_6^*}$ and $E_{sub\_distortion}$ are the single-point energy of the isolated Li_2S_6 and substrate after Li_2S_6 adsorption, respectively, whereas $E_{\mathrm{Li_2S_6}}$ and E_{sub} represent their energies before adsorption. Moreover, we also considered interaction energy between distorted Li_2S_6 and SA-$Mo_2B_2O_2$ (E_{int}) which eliminates energies from distortion:

$$E_{int} = E_{sub+Li_2S_6^*} - E_{\text{sub\_distortion}} - E_{Li_2S_6^*} \quad (6.3)$$

where $E_{sub+Li_2S_6^*}$, $E_{\text{sub\_distortion}}$, and $E_{Li_2S_6^*}$ are the single-point energy of system after Li_2S_6 adsorption, including the substrate with Li_2S_6 absorption, the substrate and isolate Li_2S_6 molecules, respectively. The details of how these energies are calculated using DFT are explained in **Figure 6.1**.

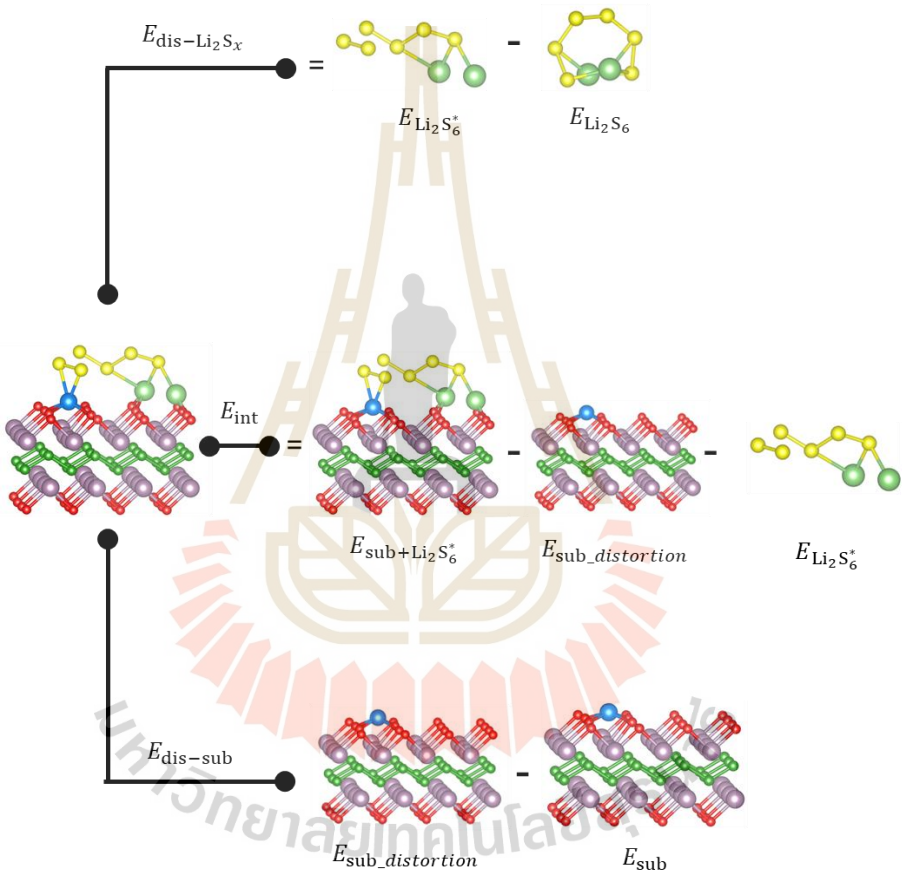

Figure 6.1 Representation of computational approaches for determining interaction energy (E_{int}) and decomposition energy of Li_2S_6 ($E_{dis-Li_2S_x}$) and SA-$Mo_2B_2O_2$ ($E_{\text{dis-sub}}$).

The heat maps for 3*d*- and 4*d*-transition metals, shown in **Figures 6.1** and **6.2**, suggested their correlations with Li_2S_6 adsorption energy and related properties. For 3*d*-transition metals, no significant correlations were suggested with Li_2S_6 adsorption energy. In contrast, 4*d*-transition metals displayed strong correlations with SA-O bond length (-0.77) and atomic radius (-0.63). When considering other energies,

3*d*-transition metals exhibited moderate correlations for interaction energy with atomic number (-0.62), atomic weight (-0.58), and SA charge transfer (0.63). Meanwhile, 4*d*-transition metals maintained strong correlations primarily with SA-O bond length (-0.73) and atomic radius (-0.60). For Li_2S_6 distortion, both 3*d*- and 4*d*-transition metals exhibited similar correlation as those suggested for interaction energy. However, 3*d*-transition metals also showed additional strong correlations with covalent radius (0.77) and electron affinity (-0.61). Regarding SA-$Mo_2B_2O_2$ distortion, no notable correlations were found for either 3*d*- or 4*d*-transition metals, suggesting that the properties analyzed in this study could not adequately explain the distortion behavior of SA-$Mo_2B_2O_2$.

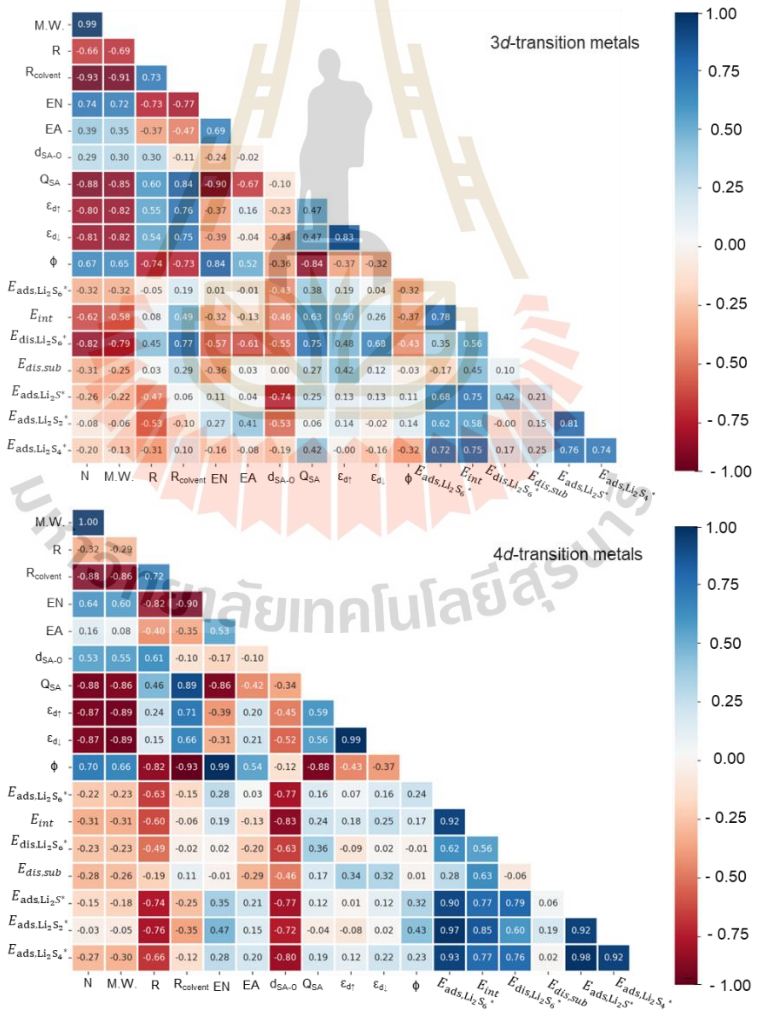

Figure 6.2 Pearson correlation heatmap for properties influencing LiPSs adsorption by 3*d*- and 4*d*-transition metals.

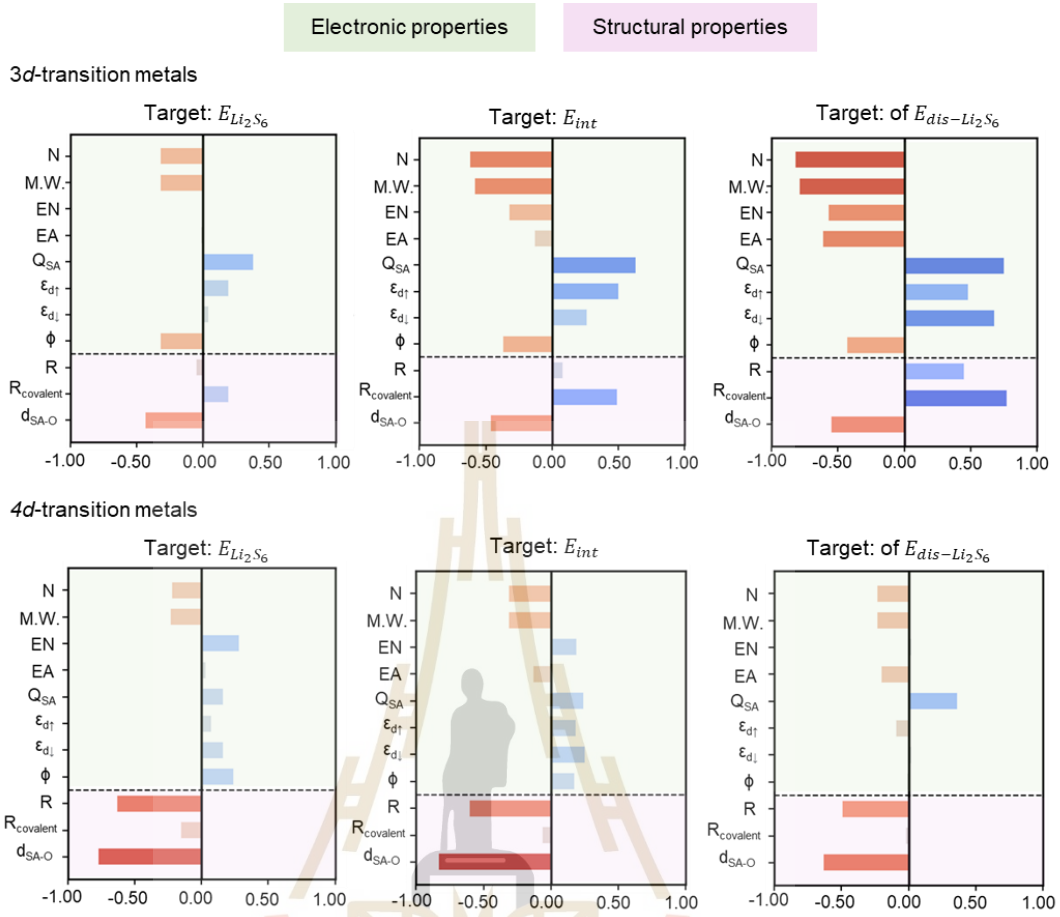

Figure 6.3 Feature correlation analysis between properties of SA/SA-$Mo_2B_2O_2$ and target, including $E_{Li_2S_6}$, E_{int}, $E_{dis-Li_2S_6}$ for each period. The x-axis represents the Pearson correlation coefficients, suggesting the strength of correlation between variable pairs. Darker colors suggest stronger correlations with SA adsorption energy relative to other features.

From results of Pearson correlations, it suggests that 3*d*- and 4*d*-transition metals show different properties that influence Li_2S_6 adsorption, as revealed by their correlation strengths. For 3*d*-transition metals, electronic properties such as charge transfer and atomic number (which impacts d-electron configuration) play a more significant role in Li_2S_6 adsorption than geometric properties. In contrast, for 4*d*-transition metals, geometric properties, including SA-O bond length and atomic radius, exhibit stronger correlations with Li_2S_6 adsorption. These can be attributed to the more delocalized nature of the d-orbitals in 4*d*-transition metals compared to those in 3*d*-

transition metals, resulting in comparable bonding interactions with sulfur atoms among the 4*d*-transition metals.

In summary, our study suggests that for 3*d*-transition metals, the electronic properties of SA-$Mo_2B_2O_2$ play a greater role in influencing Li_2S_6 adsorption and its structural distortion. In contrast, geometric properties are more critical for 4*d*-transition metals. Nevertheless, this analysis does not completely account for the trends suggested in the Li_2S_6 adsorption energy of 3*d*- and 4*d*-transition metals. nor does it clarify why the third transition metal in each period exhibits the best performance. The analysis mainly suggests the different key properties of 3*d*- and 4*d*-transition metals that impact Li_2S_6 adsorption. Hence, we further studied the bonding and antibonding states in the d-p hybridization, as these play a crucial role in determining the strength of Li_2S_6 adsorption, as discussed in Section 6.2.

6.2 Effect of Electron Occupancy in d-p Hybridization on Li_2S_6 Adsorption

In this section, we explore why third transition metal exhibit strongest Li_2S_6 adsorption and why 3*d*- and 4*d*-transiton metals show difference adsorption energy trend. The analysis used in this section is considering electron filling in d-p hybridization between SA and S atom of LiPSs. To provide this understanding, we used Ligand field theory (LFT), a framework that effectively explains electron occupancy in bonding, nonbonding, and antibonding states. It helps clarify the SA-S bond strength and the suggested trends in Li_2S_6 adsorption.

The energy diagram in LFT is based on the coordination of SA with four oxygen atoms, forming a D_{4h} crystal field. It splits the d-orbitals into four states: $d_{z^2}, d_{xy}, d_{x^2-y^2},$ and the degenerate d_{yz}/d_{xz} orbitals, as shown in **Figure 6.4**. These orbitals interact with S 3p orbitals of Li_2S_6, resulting in bonding, nonbonding, and antibonding states. In this thesis, we employed PDOS and COHP calculation to analyse LFT (Dronskowski et al., 1993; Han et al., 2021; Zhang et al., 2022). For simplicity, we used Li_2S as a representative molecule for Li_2S_6 because SA interacts with single sulfur atom in Li_2S, reducing complexity of LFT. Furthermore, the adsorption energy trend of Li_2S closely

aligns with that of Li_2S_6, suggesting that Li_2S adsorption can effectively explain the trends suggested for Li_2S_6 adsorption.

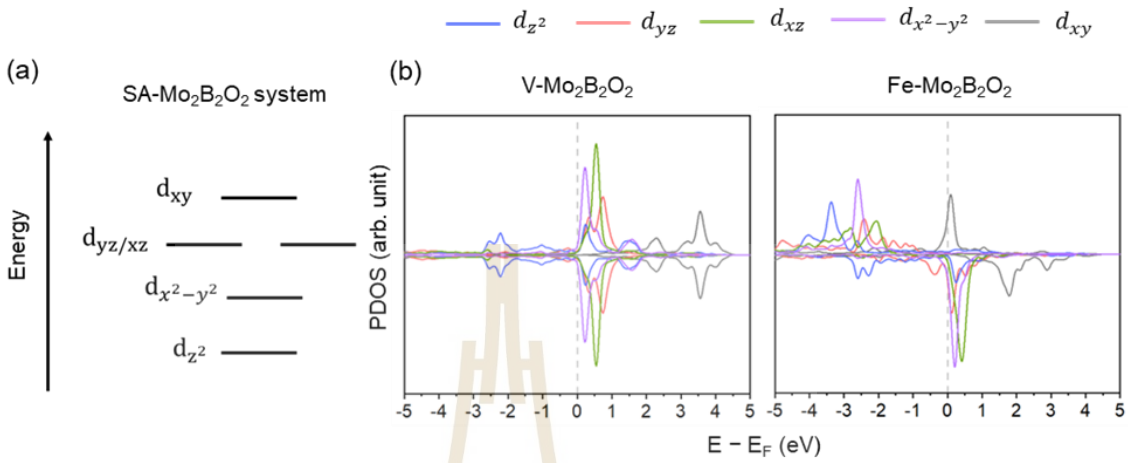

Figure 6.4 (a) Ligand field theory diagram with (b) example PDOS of SA-$Mo_2B_2O_2$, including V- and Nb-$Mo_2B_2O_2$.

After calculating PDOS and COHP results, both methods consistently explain electron filling in LFT, particularly concerning the energy positions of bonding, nonbonding, and antibonding states. The method was shown in **Figure 6.5**. When the d-orbitals overlap with the p-state of sulfur, they split into two distinct states: bonding and antibonding. Conversely, if the d-orbitals exhibit a single state, it indicates a nonbonding interaction. Our PDOS results suggest that bonding and antibonding states are suggested in d_{z^2} and d_{yz}/d_{xz}, while $d_{x^2-y^2}$ and d_{xy} show nonbonding. States located below the Fermi level suggest electron occupancy in those orbitals. Additionally, all SA-S bonding states are near the Fermi level, with no significant overlap between SA-O bonds, which are mainly located far from the Femi level, as shown in Figure **6.6a**. Nevertheless, in this thesis, Zn- and Cd-$Mo_2B_2O_2$ were excluded from the analysis due to their significant p-orbital hybridization with the sulfur p-orbital near the Fermi level, as shown in Figure **6.6b**. Consequently, the PDOS and COHP of each SA-$Mo_2B_2O_2$ used in this thesis were shown in **Figure 6.7-6.10**.

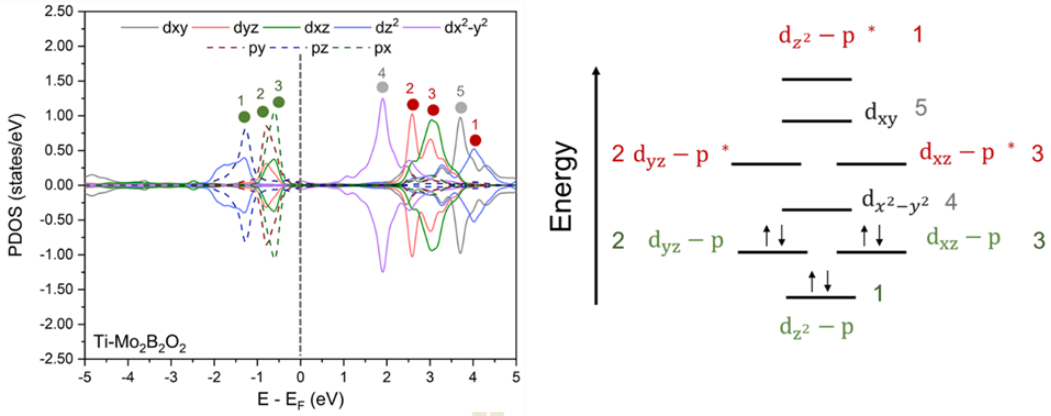

Figure 6.5 Schematic illustration of analysis projected density of states (PDOS) for Ligand field theory writing, as shown in Ti-$Mo_2B_2O_2$ example.

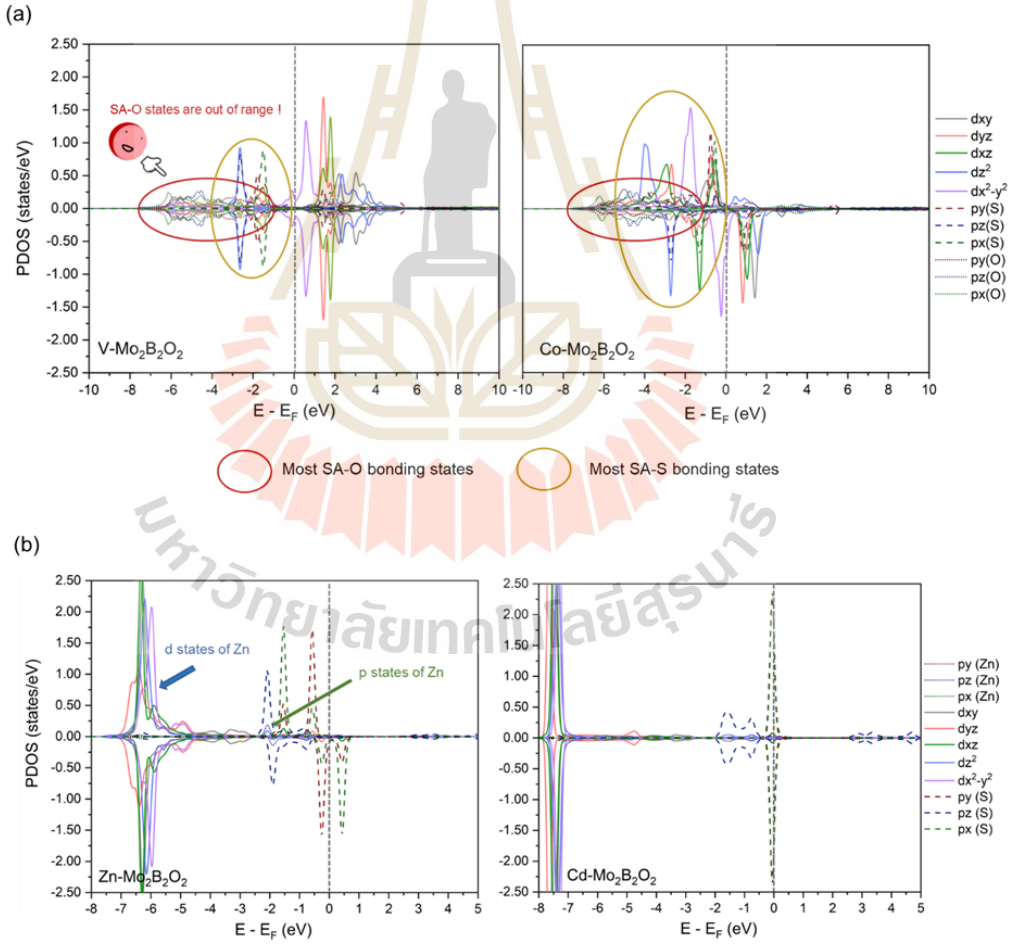

Figure 6.6 (a) Projected density of states (PDOS) of example SA-$Mo_2B_2O_2$ which show SA-O bonding are more negative energy than SA-S bonding. (b) Considering PDOS of Zn and Cd-$Mo_2B_2O_2$, d^{10} transition metals, which show p state of S and Zn near Femi energy.

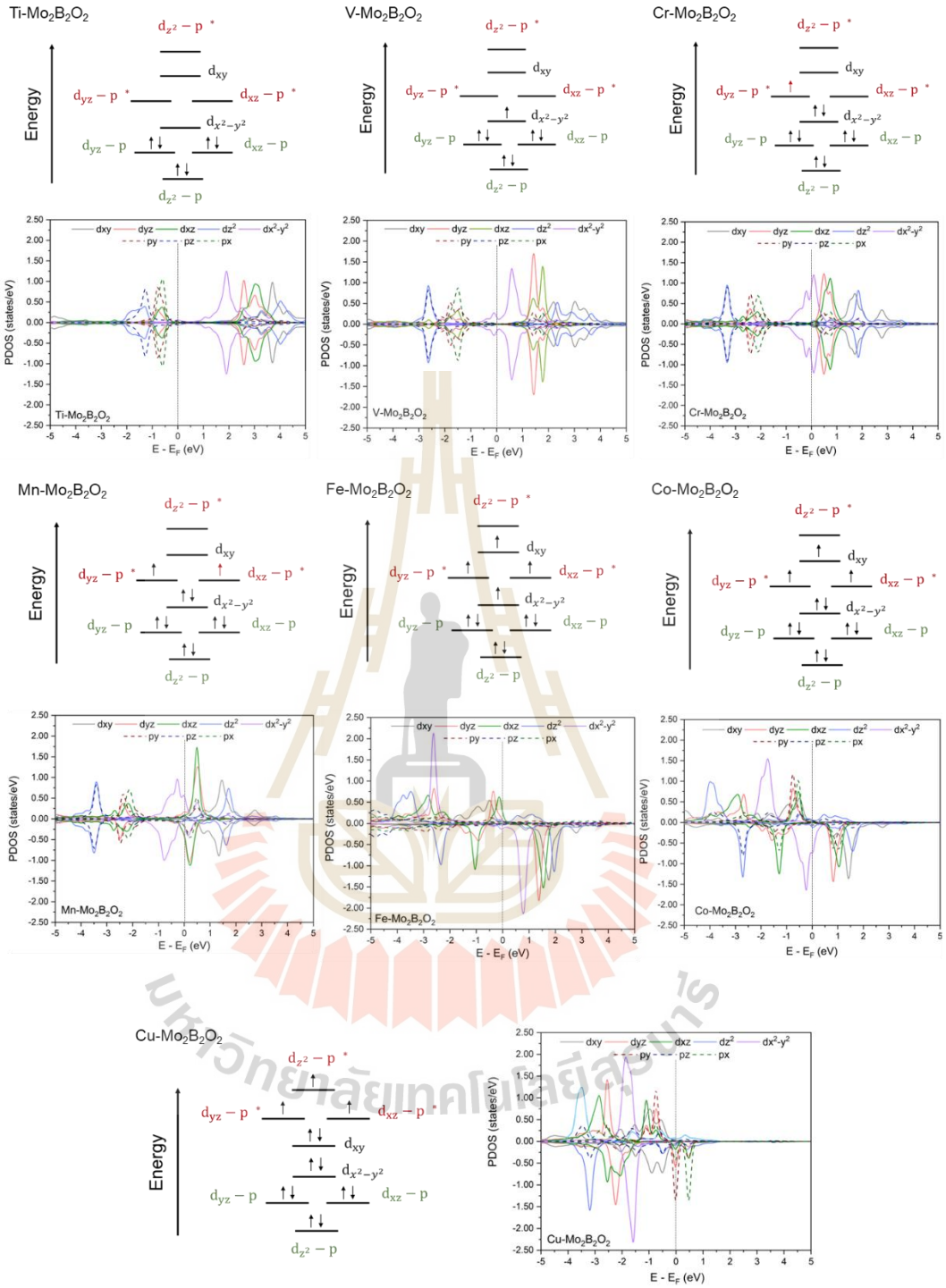

Figure 6.7 Ligand field theory diagrams with PDOS of each 3*d*-transtion metal for SA-$Mo_2B_2O_2$.

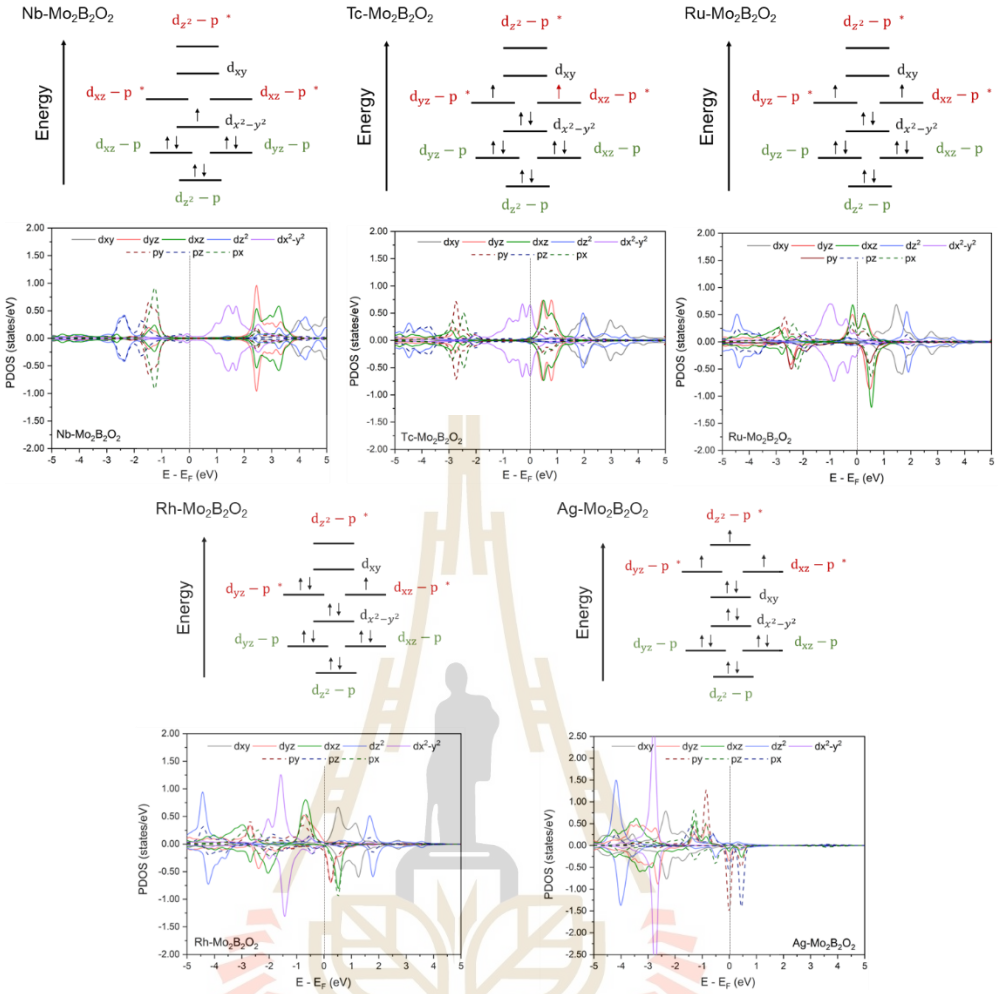

Figure 6.8 Ligand field theory diagrams with PDOS of each 4*d*-transtion metal for SA-$Mo_2B_2O_2$.

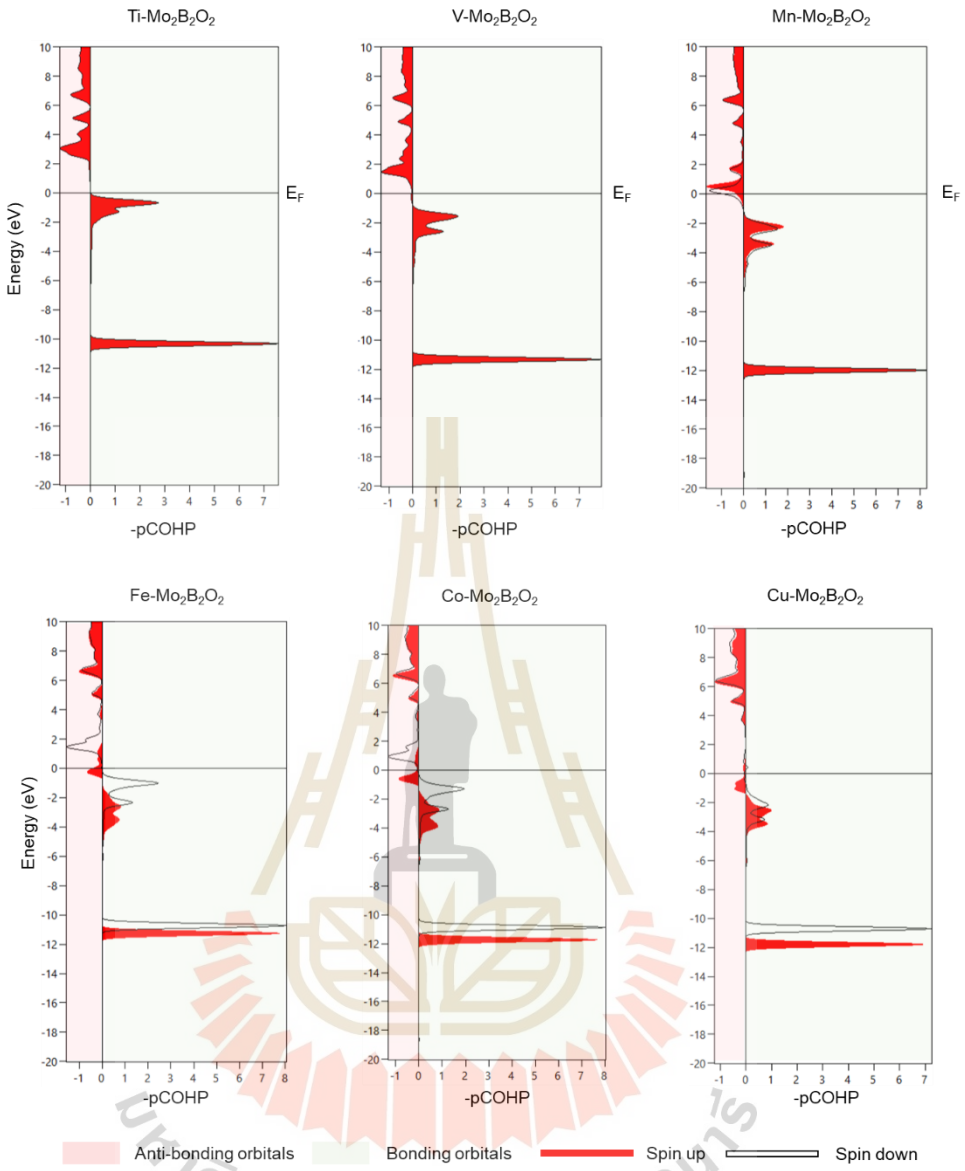

Figure 6.9 Crystal orbital Hamilton population (COHP) graph of 3*d*-transition metals for SA-$Mo_2B_2O_2$ when Li_2S adsorbed. Spin up and Spin down states were showed through red and black line. Green area suggests bonding orbital states, whereas antibonding orbital states were represented in red area.

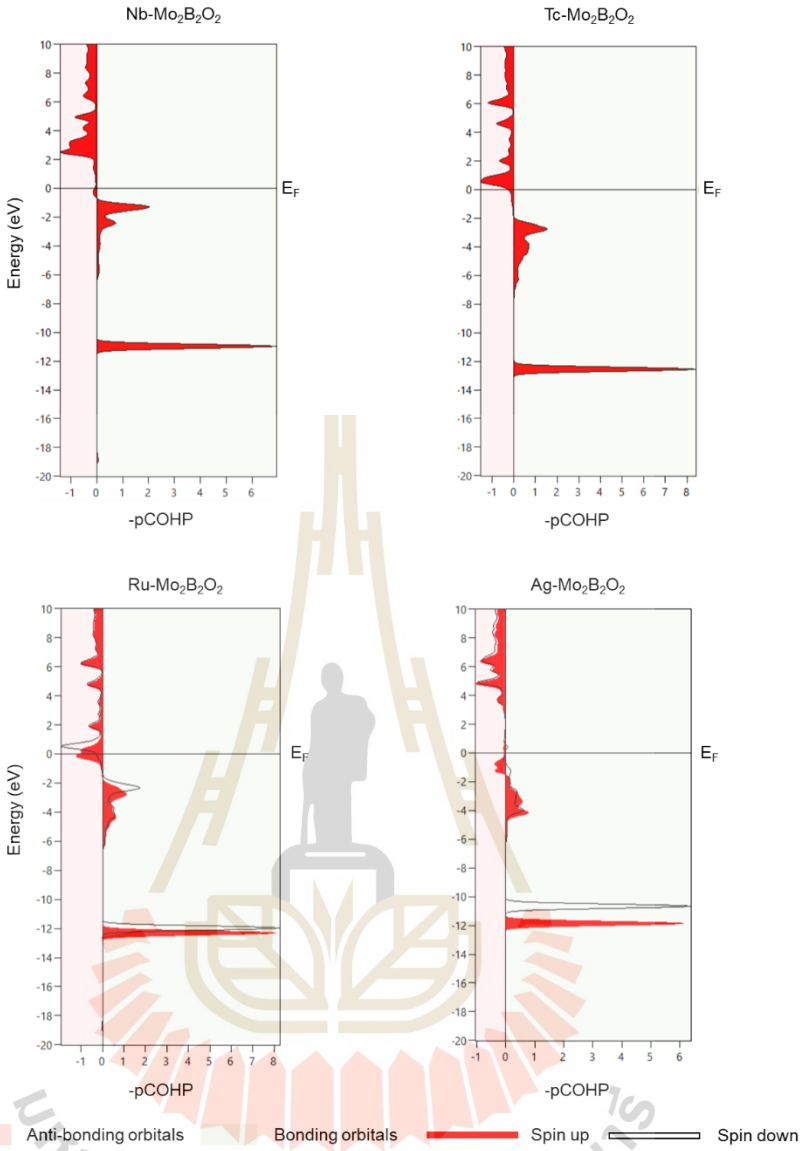

Figure 6.10 Crystal orbital Hamilton population (COHP) graph of 4*d*-transition metals for SA-$Mo_2B_2O_2$ when Li_2S adsorbed. Spin up and Spin down states were showed through red and black line. Green area suggests bonding orbital states, whereas antibonding orbital states were represented in red area.

Using LFT for all SA-$Mo_2B_2O_2$, we categorized the Li_2S adsorption energy trends for both 3*d*- and 4*d*-transition metals based on their distinct electron filling, as shown in **Figure 6.11**. However, in the case of Pd-$Mo_2B_2O_2$, the energy levels of each state and the electron filling pattern differ from the others. Therefore, in this work, it is analyzed separately, as shown in **Figure 6.12**.

First, the bonding region (highlighted in green) suggests that electrons occupy only the bonding state, with no electrons in the antibonding state. As the atomic number increases, more electrons fill the bonding states, thereby strengthening the SA-S bond. It corresponds to Li_2S_6 adsorption suggested in this region. As a result, early transition metals, particularly the third transition metals (V- and Nb-$Mo_2B_2O_2$), exhibit stronger LiPSs adsorption.

In the antibonding region (Type I) or yellow region, the bonding states are fully occupied. As the atomic number increases, more electrons populate the antibonding states, leading to a decrease in SA-O bond strength.

Interestingly, the antibonding region (Type II) or red region is suggested only in 3d-transition metals. Although this region shows a similar adsorption trend to the yellow region, its electron filling pattern is noticeably different. The PDOS of Fe suggests spin-up and spin-down states for the same orbitals at different energy levels, suggesting different electron filling order between the red and yellow regions. Consequently, as the atomic number increases, paired electrons occupy the antibonding orbitals, weakening the SA-S bond.

In the ninth transition metal region, the d_{xy}-*p* orbital shifts below the d_{yz}/d_{xz} -*p* orbitals orbital. This results in partial electron occupancy within all antibonding states.

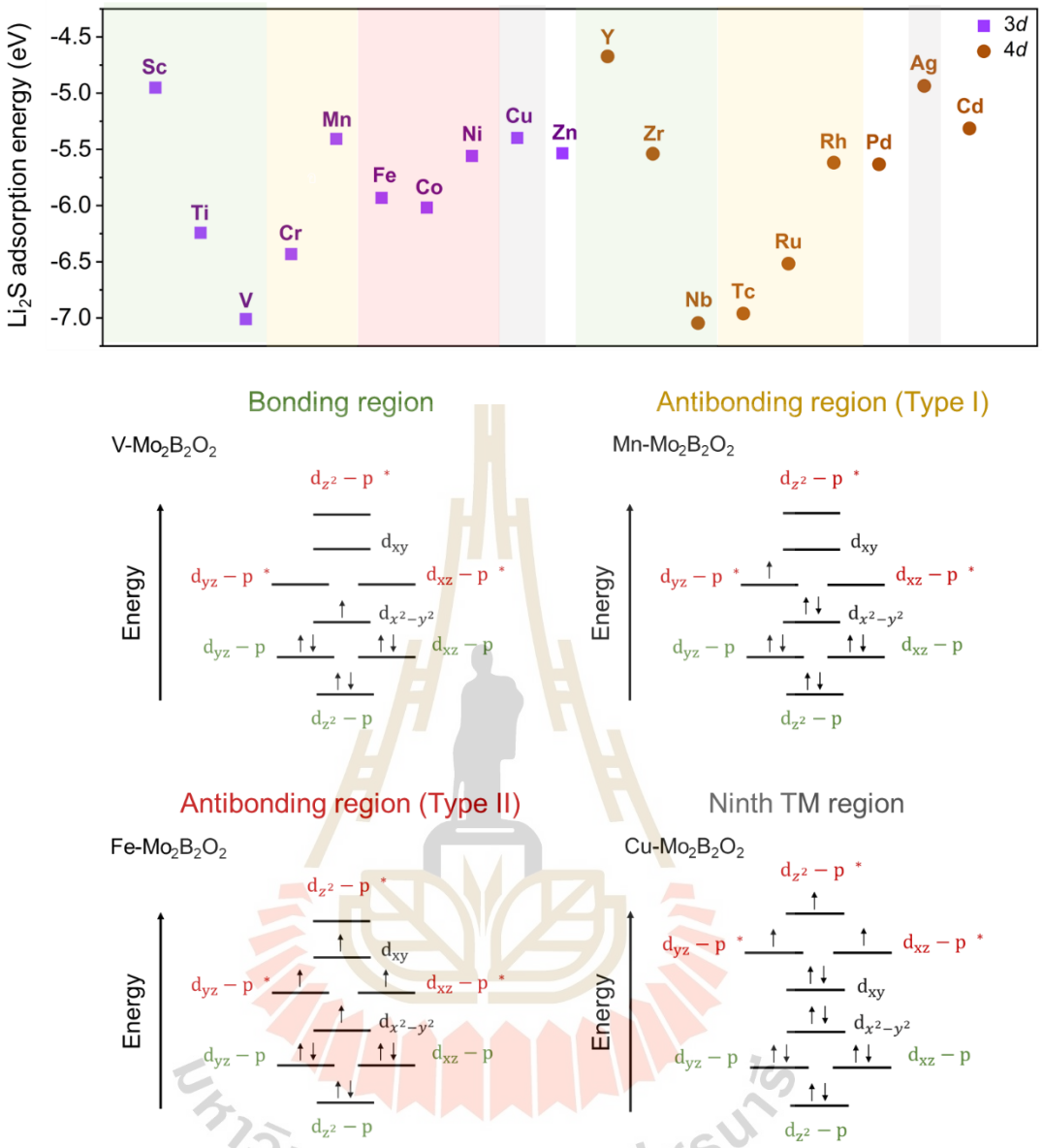

Figure 6.11 This diagram shows the methods for filling electron states in response to changes in the type of transition metal, with groups separated by color regions. Zn- and Cd-$Mo_2B_2O_2$ are excluded from consideration due to their use of p states in bonding with sulfur (S) atoms.

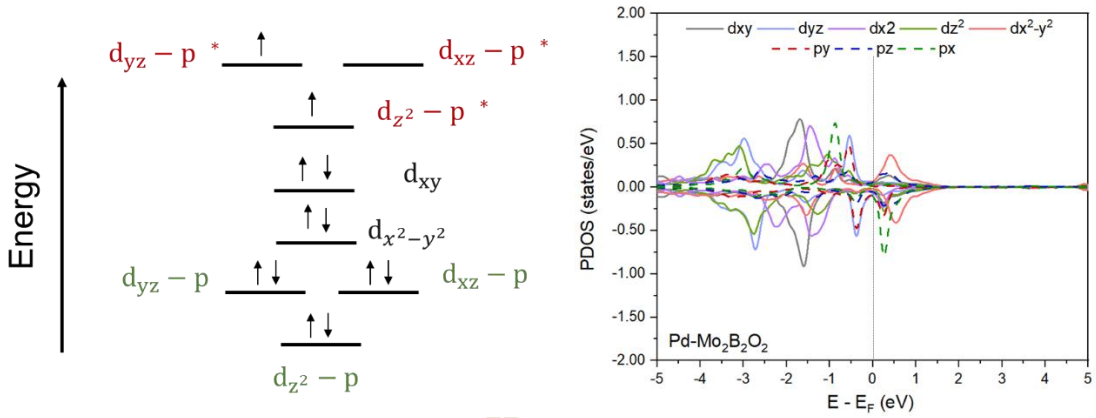

Figure 6.12 Ligand field theory diagrams with PDOS of Pd-$Mo_2B_2O_2$.

Additionally, we considered the difference in the number of electrons between bonding and antibonding states, which we refer to as the "transition complex bond order" in this thesis. The numbers are derived from the LFT results. This bond order was compared with the Li_2S adsorption energy, as shown in **Figure 6.13**. The result suggests that the bond order value obtained from LFT can effectively explain the strength of Li_2S adsorption. An increase in bond order corresponds to stronger Li_2S adsorption. From this result, it supports the correctness of the number of electrons suggested in LFT of this thesis.

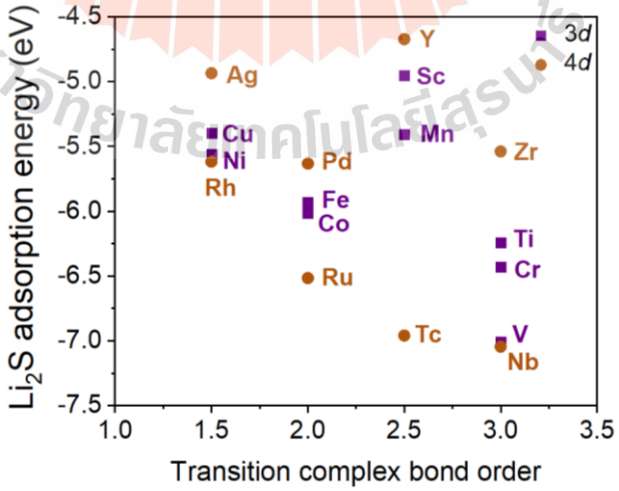

Figure 6.13 Relationship between transition complex bond order and Li_2S adsorption energy on SA-$Mo_2B_2O_2$ for 3*d*- and 4*d*-transition metals

Overall, the differences in Li_2S_6 and Li_2S adsorption energy trends, especially for late transition metals between 3*d*- and 4*d*- transition metals, can be attributed to differences in electron occupancy within the d-p hybridization of the SA-S bond. For late transition metals, 3*d*-transition metals exhibit a shift in electron filling patterns from the antibonding (Type I) region to the antibonding (Type II) region. In contrast, 4*d*-transition metals retain the same electron filling pattern associated with the antibonding (Type I) region.

6.3 Selective Orbital Coupling

To further explain the trend in LiPSs adsorption strength for SA-$Mo_2B_2O_2$, we employed the concept of selective orbital coupling (He et al., 2024). This approach involves analyzing the energy levels of specific d-states of the SA and their interaction with the p or π states of the adsorbate, offering an alternative perspective on SA interactions. In this study, S_2 molecule was used as a simplified model for Li_2S_6 adsorption, as the polysulfide binding to the SA site primarily involves two sulfur atoms. Using S_2 reduces the complexity associated with the electronic states of the Li_2S_6 molecule. To suggest selective orbital coupling, PDOS of SA-$Mo_2B_2O_2$ and isolated S_2 molecules were employed, as shown in **Figure 6.14**. For S_2 molecules, we focused on the unoccupied π^* state near the Fermi level, specifically the $\pi^*\downarrow$ state, as this state plays a critical role in overlapping with the d-states of the SA. For suggest selective d state of this thesis, we study PDOS of SA-$Mo_2B_2O_2$ after S_2 adsorption. In example of V- and Nb-$Mo_2B_2O_2$ shown in **Figure 6.15**, the results suggest significant overlap between the $d_{x^2-y^2}$ orbital as the critical state for S_2 adsorption. Notably, we only considered the unoccupied $d_{x^2-y^2}\downarrow$ state, as suggested by the electronic structure of most SA-$Mo_2B_2O_2$.

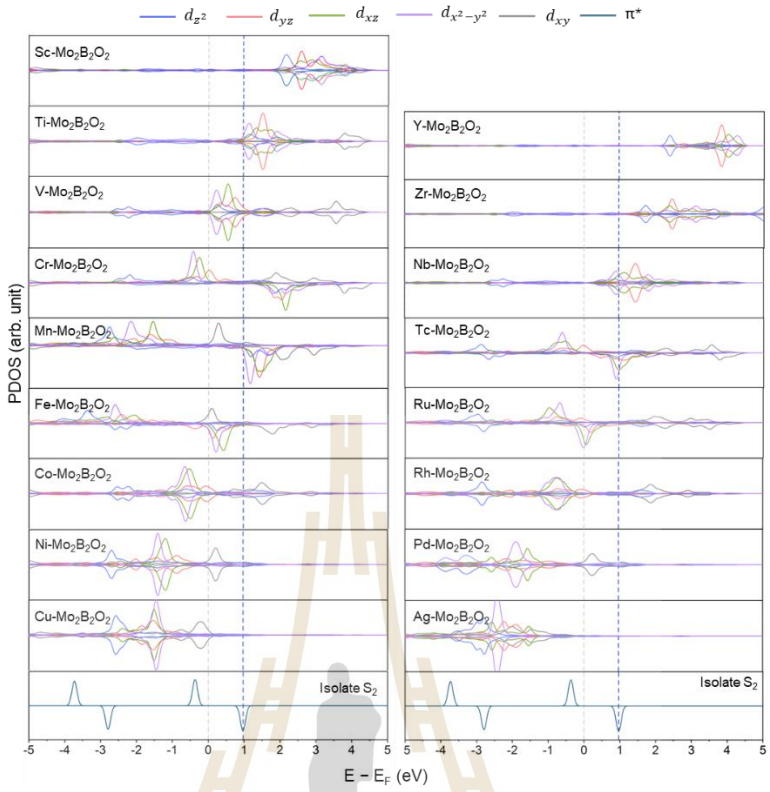

Figure 6.14 PDOS of d states of each SA-$Mo_2B_2O_2$ and π state of isolate S_2 molecule. The gray dashed line represents the Fermi level, while the blue dashed line indicates the $\pi^*\downarrow$ energy level.

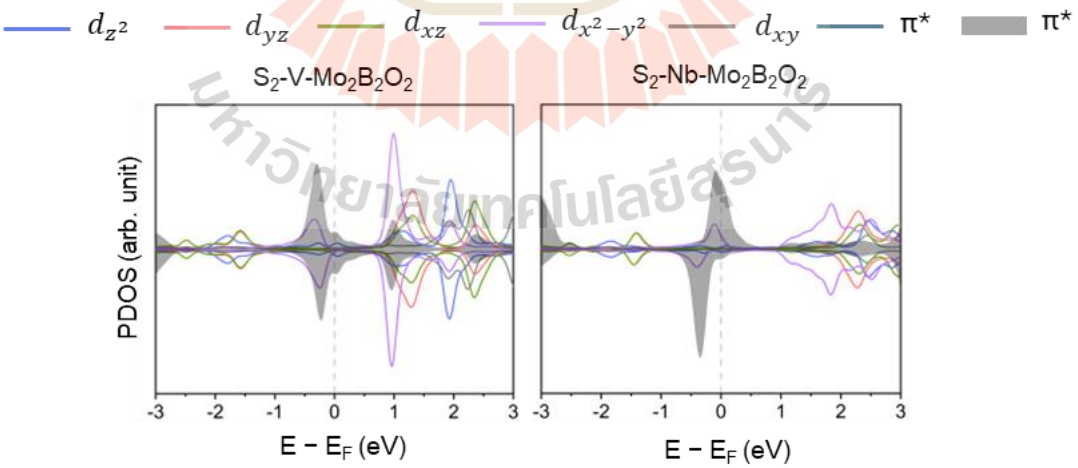

Figure 6.15 PDOS for S_2 adsorbed on V- and Nb-$Mo_2B_2O_2$. The gray dashed line represents the Fermi level.

In the next step, we compared the energy level of $d_{x^2-y^2}\downarrow$ state for each SA-$Mo_2B_2O_2$ with $\pi^*\downarrow$ state of S_2 to explain the trends in Li_2S_6 adsorption energy. The comparison of these energy levels is based on the hybridization energy (ΔE_{hyb}), which is used to suggest adsorption strength. The hybridization energy is defined as:

$$\Delta E_{hyb} = \frac{\left|H_{d_{x^2-y^2}\downarrow,\pi^*\downarrow}\right|^2}{\varepsilon_{d_{x^2-y^2}\downarrow} - \varepsilon_{\pi^*\downarrow}} \quad (6.4)$$

In this thesis, the adsorption strength was quantified using the integrated crystal orbital Hamilton population (-ICOHP), which represents the bond strength between the SA and the nearest sulfur atom. As shown in **Figure 6.16**, the relationship between -ICOHP and the energy level of $d_{x^2-y^2}\downarrow$ state show a volcano plot. The -ICOHP increases as the energy level of the $d_{x^2-y^2}\downarrow$ become closer the $\pi^*\downarrow$ state of S_2, suggesting stronger bonding of SA-S bond. We focus on early to mid-transition metals (green region) because late transition metals exhibit a different configuration, bonding with only one sulfur atom (yellow region).

Among the 3*d*-transition metals, V-$Mo_2B_2O_2$ exhibits the closest energy alignment with the $\pi^*\downarrow$ state, resulting in the strongest SA-S bond and the highest Li_2S_6 adsorption energy. Furthermore, the $d_{x^2-y^2}\downarrow$ energy level in Fe-$Mo_2B_2O_2$ is closer to the $\pi^*\downarrow$ state than in Cr-$Mo_2B_2O_2$, explaining why Fe as the SA leads to stronger Li_2S_6 adsorption. For 4*d*-transition metals, a similar trend is suggested in Li_2S_6 adsorption energy. While Tc-$Mo_2B_2O_2$ has the closest energy alignment with the π^* state, it suggests weaker Li_2S_6 adsorption compared to Nb-$Mo_2B_2O_2$. It can be explained by -ICOHP values not accounting for van der Waals interactions. When excluding van der Waals forces, the Li_2S_6 adsorption energies for Tc- and Nb-$Mo_2B_2O_2$ are -4.05 eV and -2.06 eV, respectively.

In summary, the strength of Li_2S_6 adsorption can be explained by the alignment of the selective d-state energy level with π^* state of the adsorbate. This alignment also clarifies why the third transition metals exhibit stronger LiPSs adsorption and why Fe shows increased adsorption strength with LiPSs.

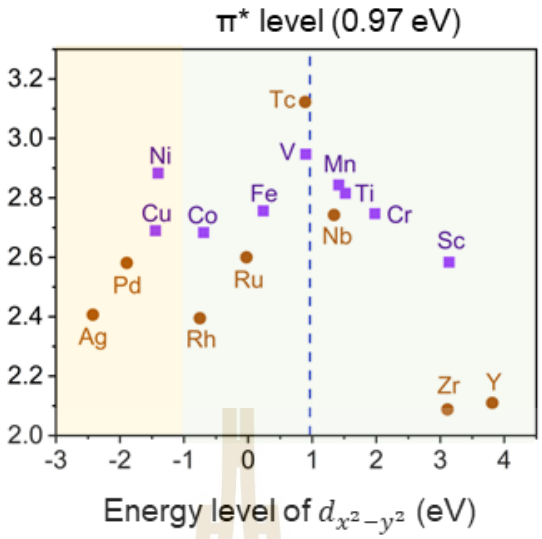

Figure 6.16 Relationship between the energy level of $d_{x^2-y^2}\downarrow$ state and the integrated crystal orbital Hamilton populations (-ICOHP), using the $\pi^*\downarrow$ energy level as a reference. The blue dashed line indicates the $\pi^*\downarrow$ energy level.

6.4 Reference

Dronskowski, R., and Bloechl, P. E. (1993). Crystal orbital Hamilton populations (COHP): energy-resolved visualization of chemical bonding in solids based on density-functional calculations. *The Journal of Physical Chemistry, 97*(33), 8617-8624.

Han, Z., Zhao, S., Xiao, J., Zhong, X., Sheng, J., Lv, W., Zhang, Q., Zhou, G., and Cheng, H.-M. (2021). Engineering d-p Orbital Hybridization in Single-Atom Metal-Embedded Three-Dimensional Electrodes for Li–S Batteries. *Advanced Materials, 33*(44), 2105947.

He, C., Lee, C.-H., Meng, L., Chen, H.-Y. T., and Li, Z. (2024). Selective Orbital Coupling: An Adsorption Mechanism in Single-Atom Catalysis. *Journal of the American Chemical Society, 146*(18), 12395-12400.

Singsen, S., Fongkaew, I., Hirunsit, P., and Suthirakun, S. (2022). Suppressing Polysulfides Shuttling and Promoting Sulfur Utilization via Transition Metal and Nitrogen Co-Doping on Graphdiyne Cathodes of Lithium-Sulfur Batteries: A First-Principles Modeling. *ACS Applied Energy Materials, 5*(8), 9722-9732.

Zhang, N., Chen, X., Sun, C., Xie, W., Wang, X., and Yao, J. (2022). Revealing the key role of bonding states in surface chemisorption. *Chemical Engineering Science, 249*, 117345.

CHAPTER VII
ELECTROCHEMICAL REACTION OF SULFUR ON SA-$Mo_2B_2O_2$

In the previous chapters, we evaluated the LiPSs adsorption performance of various SA-$Mo_2B_2O_2$ systems and found that V- and Nb-$Mo_2B_2O_2$ exhibited the strongest LiPSs adsorption energy within their periods. Furthermore, we suggested the reasons why the third transition metal shows the strongest adsorption and explained the differing LiPSs adsorption energy trends between 3*d*- and 4*d*-transition metals. In this chapter, we extend our study to the catalytic activity of SA-$Mo_2B_2O_2$ compared to pristine $Mo_2B_2O_2$ during reduction and oxidation reactions. For the reduction process, referred to as the "sulfur reduction reaction (SRR)," a significant challenge arises from the high potential-limiting step during the conversion of Li_2S_4 to Li_2S. This challenge is due to the phase transition between liquid and solid, combined with the insulating properties of Li_2S_2 and Li_2S. In the oxidation process, we focus on the decomposition of Li_2S, which requires overcoming a high energy barrier to break the Li-S bond. Therefore, If the presence of SA effectively resolves these challenges, it would highlight the high catalytic activity of SA-$Mo_2B_2O_2$, making it a promising material for Li-S batteries. The SRR process is explained in Section 7.1, and the oxidation process is discussed in Section 7.2.

7.1 SRR Catalytic Activity of Pristine and SA-$Mo_2B_2O_2$

In addition to strong LiPS adsorption and suppression of the shuttle effect, high-performance cathode materials for Li-S batteries must also exhibit substantial catalytic activity to enhance SRR. Effective SRR catalysis is essential for reducing high potential barriers, particularly during the conversion of Li_2S_4 to Li_2S, which involves a phase transition from liquid to solid and the challenging conductivity issues of Li_2S_2 and Li_2S. In this section, we explored the catalytic activity of SA-$Mo_2B_2O_2$ for SRR and compared

it with pristine $Mo_2B_2O_2$. We aimed to suggest the specific role of SA in lowering energy barriers and facilitating redox reactions.

The sulfur reduction reaction (SRR) involves the transformation of S_8 into Li_2S through a 16-electron transfer mechanism. As showed in Equations (6)-(11) (Assary et al., 2014; Barchasz et al., 2012; Zhou et al., 2020), this process consists of five electron transfer steps and the final Li_2S nucleation step that does not involve electron transfer:

$$S_8 + 2\,Li^+ + 2\,e^- + * \rightarrow Li_2S_8^* \tag{7.1}$$

$$Li_2S_8^* + \frac{2}{3}Li^+ + \frac{2}{3}e^- + \frac{1}{3}* \rightarrow \frac{4}{3}Li_2S_6^* \tag{7.2}$$

$$\frac{4}{3}Li_2S_6^* + \frac{4}{3}Li^+ + \frac{4}{3}e^- + \frac{2}{3}* \rightarrow 2Li_2S_4^* \tag{7.3}$$

$$2Li_2S_4^* + 4Li^+ + 4e^- + 2* \rightarrow 4Li_2S_2^* \tag{7.4}$$

$$2Li_2S_2^* + 8Li^+ + 8e^- + 4* \rightarrow 4Li_2S^* \tag{7.5}$$

$$2Li_2S^* \rightarrow 4Li_2S + 8* \tag{7.6}$$

These electrochemical reaction mechanisms proceed via the ($Li^+ + e^-$) process, differing from conventional reaction mechanisms that involve the addition of S_8 and are typically analyzed in thermodynamic calculations (Boteju et al., 2024; Khossossi et al., 2020; Zhou et al., 2020). Among the steps involved in the SRR process, the conversion from Li_2S_4* to Li_2S* (Equations (7.4)-(7.6)) is typically the potential limiting step for many SA catalysts (Han et al., 2021; Li Wang et al., 2022; Zhou et al., 2020). To efficiently evaluate the SRR catalytic activity of the SA-$Mo_2B_2O_2$ while minimizing computational effort, we focused on analyzing the critical reaction steps at the equilibrium potential (U_{eq}) of 2.15 V, which corresponds to the average cell voltage of Li-S batteries (Akridge et al., 2004; Evers et al., 2012). The equation of each elementary steps of conversion from Li_2S_4 to Li_2S were shown in Equations (7.7)-(7.9), with the final state used as the reference state (0 eV)

$$Li_2S_4^* + 2Li^+ + 2e^- + 1* \rightarrow 2Li_2S_2^* \tag{7.7}$$

$$2Li_2S_2^* + 4Li^+ + 4e^- + 2* \rightarrow 4Li_2S^* \quad (7.8)$$

$$4Li_2S^* \rightarrow 4Li_2S + 4* \quad (7.9)$$

First, the configurations of Li_2S_4 and Li_2S adsorbed on pristine and SA-$Mo_2B_2O_2$ were optimized before calculating the Gibbs free energy. Detailed configurations and LiPSs adsorption energies are provided in Chapter VI. As shown in **Figure 7.1-7.2** and **Table 7.1**, for pristine and most SA-$Mo_2B_2O_2$, the conversion steps from Li_2S_4* to Li_2S_2* and from Li_2S_2* to Li_2S* are exothermic. Although the final Li_2S nucleation step is highly endothermic, it is step which does not include electron transfer. However, the SA-$Mo_2B_2O_2$, including Sc-, Ni-, Cu-, Y-, Pd-, Ag-, and Cd-$Mo_2B_2O_2$ the conversion from Li_2S_2* to Li_2S* transitions to an endothermic reaction, making it the potential-determining step.

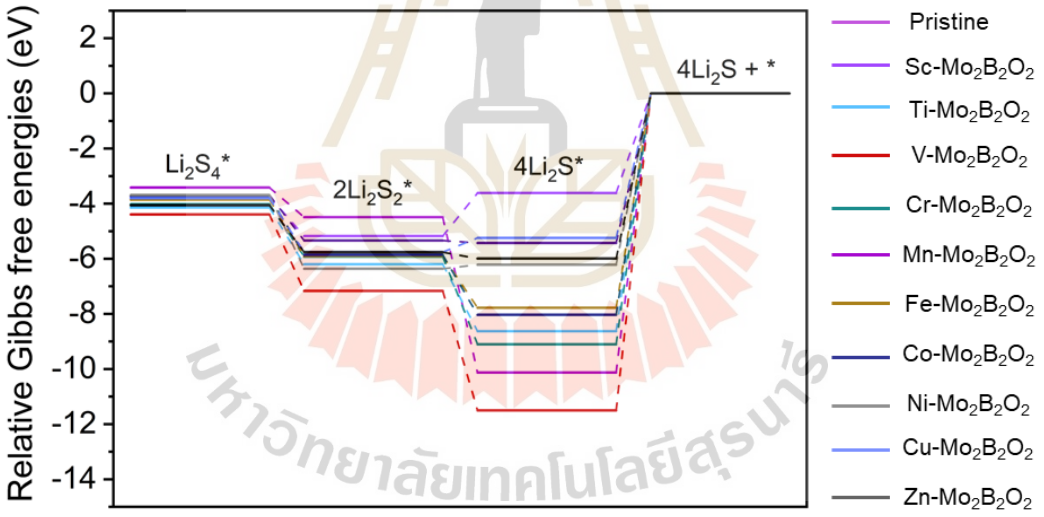

Figure 7.1 Gibbs free energy diagram for conversion from Li_2S_4 to Li_2S when adsorbed on pristine and SA-$Mo_2B_2O_2$ of 3*d*-transition metals at U_{eq} = 2.15 V.

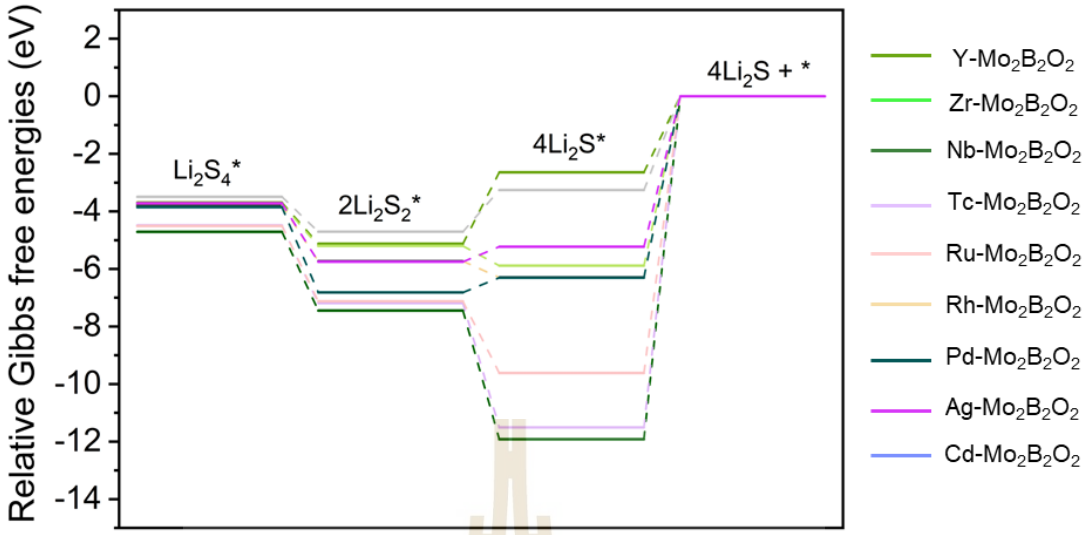

Figure 7.2 Gibbs free energy diagram for conversion from Li_2S_4* to Li_2S* when adsorbed on SA-$Mo_2B_2O_2$ of 4*d*-transition metals at U_{eq} = 2.15 V.

Additionally, we analyzed the the SRR overpotentials for the two critical electron transfer steps (Li_2S_4* to Li_2S*). The overpotential was calculated using the following equation:

$$\eta_{SRR} = U_{eq} - \min\left[\frac{\Delta G_{0,i}}{ne}\right] \quad (7.10)$$

where $\Delta G_{0,i}$ represents the Gibbs free energy change of each elementary step, and ne denotes the number of electrons transferred in each step. The SRR overpotentials for the Li_2S_4* to Li_2S* conversion across all SA-$Mo_2B_2O_2$ systems is presented in **Figure 7.3**. We found that Sc-, Ni-, Cu-, Y-, Pd-, Ag-, and Cd-$Mo_2B_2O_2$ show overpotentials of this conversion, suggesting that these systems exhibit lower catalytic efficiency and are less effective as cathode materials compared to the others.

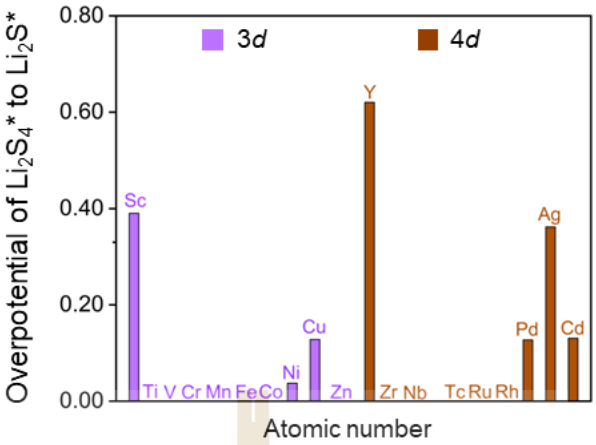

Figure 7.3 Overpotential for the Li_2S_4* to Li_2S* conversion steps at an equilibrium potential of U_{eq} = 2.15 V for SA-$Mo_2B_2O_2$ systems with 3*d*- and 4*d*-transition metal single atoms (SA).

We further analyzed the complete SRR process, which consists of five electron transfer steps, for selected SA-$Mo_2B_2O_2$ systems and compared the results to the pristine material. The selection process targeted the top three transition metals in each period that exhibited the strongest Li_2S_6 adsorption and zero overpotential during the Li_2S_4* to Li_2S* conversion. For 3*d*-transition metals, Ti, V, and Fe were chosen, while Zr, Nb, and Ru were selected from 4*d*-transition metals. Tc was excluded due to its radioactivity. At U=0 eV, it was shown in **Figure 7.4**. SRR of pristine and SA-$Mo_2B_2O_2$ show all exothermic steps.

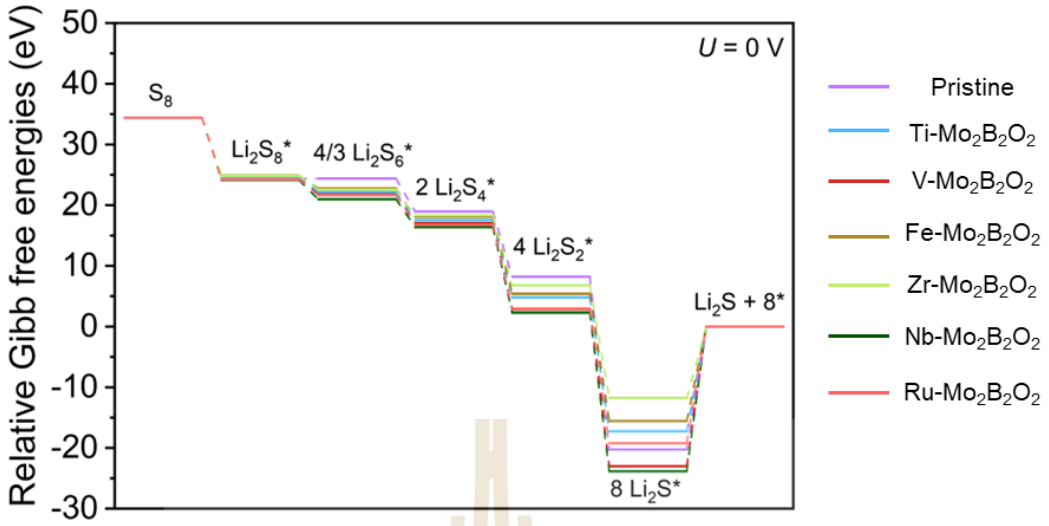

Figure 7.4 Gibbs free energy diagram showing conversion from S_8 to Li_2S when adsorbed on pristine and three representative SA-$Mo_2B_2O_2$ system from 3*d*- and 4*d*-transition metals at U = 0 eV.

At the equilibrium reduction potential of U = 2.15 V, all selected SA-$Mo_2B_2O_2$ systems exhibited exothermic reactions throughout the SRR process, from S_8 to Li_2S* (**Figure 7.5**). In contrast, pristine $Mo_2B_2O_2$ displayed a potential-limiting step during the Li_2S_8* to Li_2S_6* conversion with energy of 0.59 eV, which was attributed to significant structural distortion of Li_2S_8. When considering overpotential, all selected SA-$Mo_2B_2O_2$ systems showed zero overpotential, whereas the pristine form exhibited a significantly high overpotential of 0.88 V. These findings suggest that incorporating suitable SA can accelerate the conversion of LiPSs during SRR without introducing overpotential. Notably, V- and Nb-$Mo_2B_2O_2$ stand out due to their strong LiPS adsorption and efficient catalytic performance.

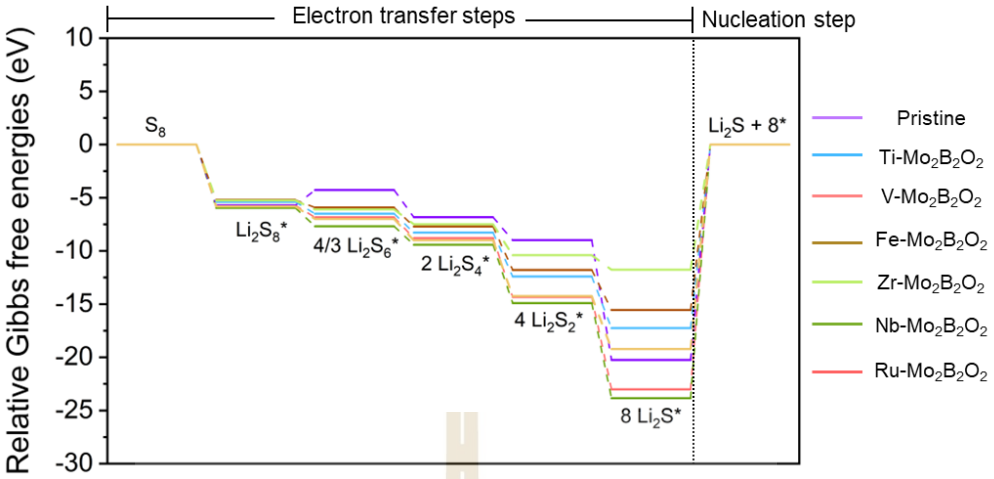

Figure 7.5 Gibbs free energy diagram for sulfur reduction reaction (SRR) of pristine and various SA-$Mo_2B_2O_2$ at U_{eq} = 2.15 V. The SRR process consists of five electron transfer steps and the final Li_2S nucleation step that does not involve electron transfer.

7.2 Oxidation Reaction Process of Pristine and SA-$Mo_2B_2O_2$

In this section, we address a critical challenge in the charging process of Li-S batteries: the sluggish kinetics of the reverse reaction of the SRR. This issue plays a major role in reduced sulfur utilization, capacity fading, and shortened cycle life(Assary et al., 2014). The main cause is the irreversible delithiation of LiPSs back to sulfur, particularly the decomposition of smaller LiPSs. Specifically, the decomposition of Li_2S is hindered by the high activation energy needed to break the ionic Li-S bond in Li_2S, which prevents Li^+ from dissolving into the electrolyte.

$$Li_2S \rightarrow S^{2-} + 2Li^+ + 2e^- \tag{7.11}$$

Following this step, the product may either directly convert to sulfur or react with other LiPSs to form sulfur (Arneson et al., 2018; S. Li et al., 2020; X. Li et al., 2016; Lina Wang et al., 2015; Zhang et al., 2017). Lowering the activation energy for Li_2S decomposition is crucial for enhancing delithiation kinetics and improving the overall performance of Li-S batteries (Ye et al., 2020). In this study, we examined the decomposition mechanism of Li_2S on SA-$Mo_2B_2O_2$ and compared it with pristine $Mo_2B_2O_2$ to suggest the effect of SA doping on the activation energy required for Li-S bond dissociation. The results suggest that Li-S bond breaking occurs spontaneously

after Li_2S adsorption, without any activation energy barrier in all cases. It could explain from the strong interaction between Li_2S and the substrate, which induces significant distortion of the LI_2S structure and facilitates Li-S bond dissociation, as shown in **Figure 7.6**.

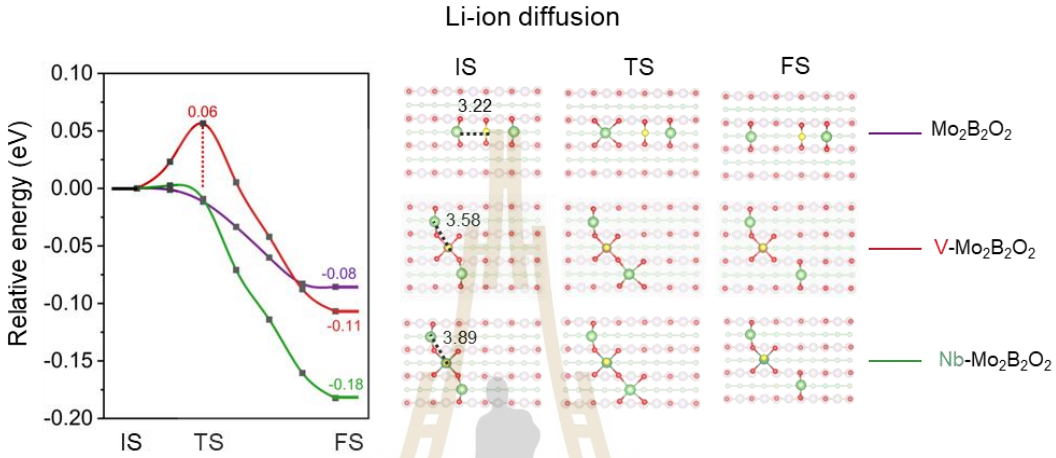

Figure 7.6 Potential energy profiles for Li ion diffusion on pristine and candidates SA-$Mo_2B_2O_2$ surfaces, with initial state (IS), transition state (TS), and final state (FS).

Following the dissociation of the Li-S bond, the Li ion tends to diffuse across the surface before dissolving into the electrolyte. For an effective catalyst, a low energy barrier for Li diffusion is advantageous, as it improves charge/discharge kinetics. In this thesis, we calculated the energy barrier for Li diffusion from dissociated Li_2S on pristine and SA-$Mo_2B_2O_2$, focusing on V- and Nb-$Mo_2B_2O_2$ due to their strong Li_2S adsorption. As shown in **Figure 7.6**, Both pristine and Nb-$Mo_2B_2O_2$ allow Li diffusion without any energy barrier, whereas V-$Mo_2B_2O_2$ presents a negligible diffusion barrier of 0.06 eV. Furthermore, when Li ions move further from the SA site, they diffuse with energy barriers of 0.04–0.05 eV, comparable to pristine $Mo_2B_2O_2$ (**Figure 7.7**).

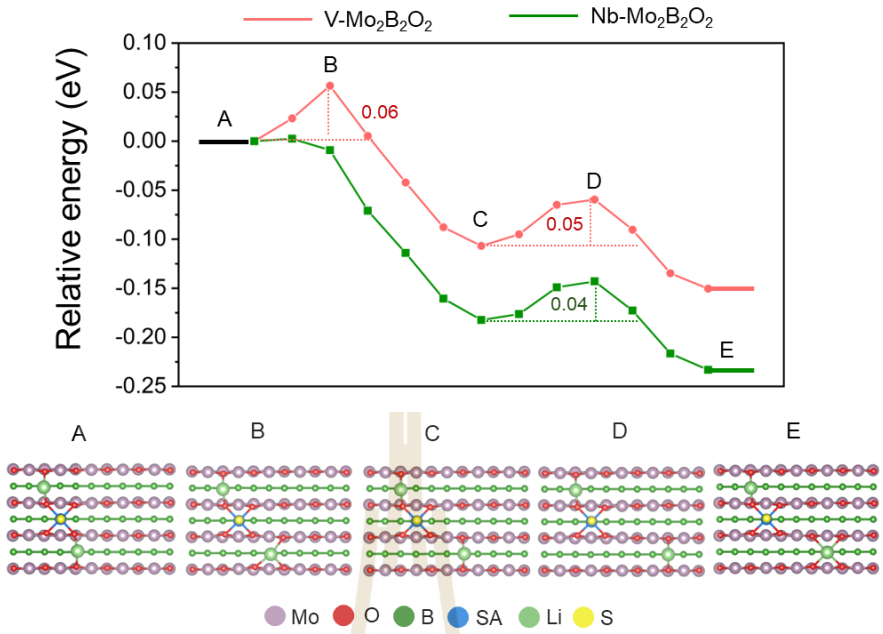

Figure 7.7 Potential energy profiles of Li diffusion through [100] for V- and Nb-$Mo_2B_2O_2$.

After Li ions diffuse away from the adsorption site, the remaining sulfur atoms stay bound to both the SA site and the $Mo_2B_2O_2$ surface. From this dissociation of Li_2S on both SA and pristine, it suggests that monoatomic sulfur anions are dispersed over the surface and SA site. These sulfur anions covered on $Mo_2B_2O_2$ surface tend to accumulate and diffuse, leading to the formation of S_8 during the oxidation process (Steudel et al., 2019; Wu et al., 2020). At SA site, the sulfur anion exhibits strong binding, with high bond breaking barriers of 3.16 eV and 3.15 eV for V- and Nb-$Mo_2B_2O_2$, respectively (**Figure 7.8**). We studied the energy barrier for sulfur diffusion from SA site using CI-NEB. While this strong sulfur adsorption may lead to sulfur poisoning at the SA site, potentially reducing catalytic activity in subsequent cycles, the sulfur anion at the SA site may also serve as a nucleation center for S_8 formation during the oxidation process.

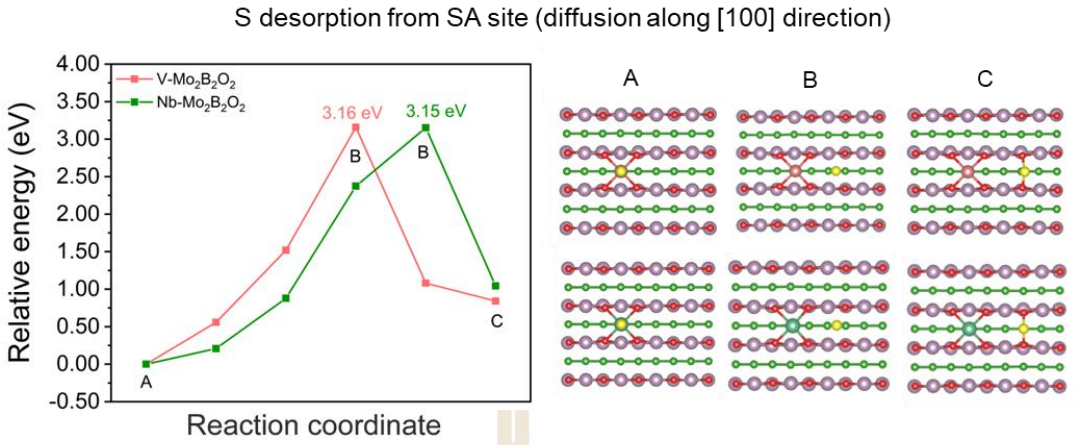

Figure 7.8 Potential energy profiles of S diffusion from SA site through [100] for V- and Nb-$Mo_2B_2O_2$.

Furthermore, to studies the impact of sulfur poisoning, we analyzed its effect by placing a sulfur atom at the SA site (S-SA-$Mo_2B_2O_2$) and studying the adsorption performance of Li_2S_6 (representing soluble LiPSs) and Li_2S (representing solid LiPSs) without considering solvent effects. As shown in **Figure 7.9**, both S-V-$Mo_2B_2O_2$ and S-Nb-$Mo_2B_2O_2$ exhibited significant distortion of the Li_2S_6 structure from a closed to an open configuration, while the Li-S bonds in Li_2S tended to break. The calculated adsorption energies for Li_2S_6 were -4.53 eV and -4.57 eV for V and Nb, respectively, and the corresponding values for Li_2S were -6.83 eV and -7.03 eV. These results suggest strong adsorption, comparable to the performance of SA-$Mo_2B_2O_2$ without sulfur poisoning. Interestingly, in both cases, the sulfur chains of Li_2S_6 and Li_2S bonded with the sulfur atom representing sulfur poisoning, forming extended sulfur chains.

When solvent effects were included through AIMD simulations with DOL or DME molecules (**Figure 7.10**), the S-SA-$Mo_2B_2O_2$ maintain interactions between the SA and the polysulfides of Li_2S_6. The polysulfides retained their open structure, even as the Li-S bonds were weakened by solvent molecules. Therefore, the presence of sulfur poisoning on SA-$Mo_2B_2O_2$ has minimal impact on the substrate's adsorption performance.

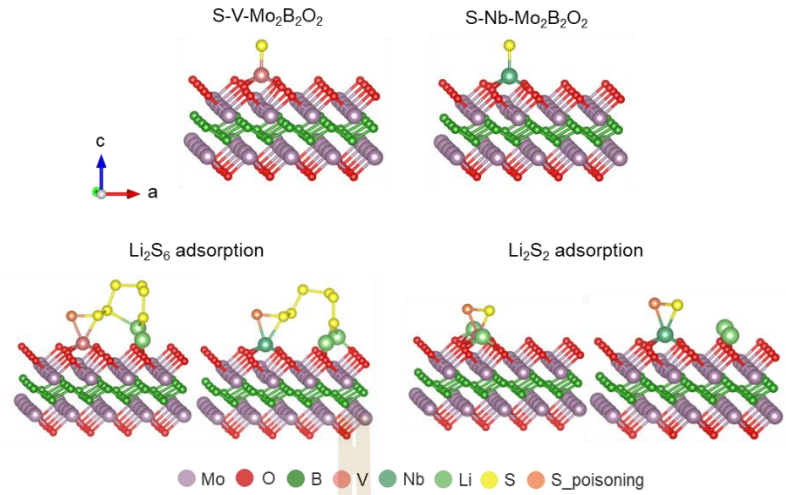

Figure 7.9 Most stable configurations of sulfur poisoning before and after the adsorption of Li_2S_6 and Li_2S on V- and Nb-$Mo_2B_2O_2$.

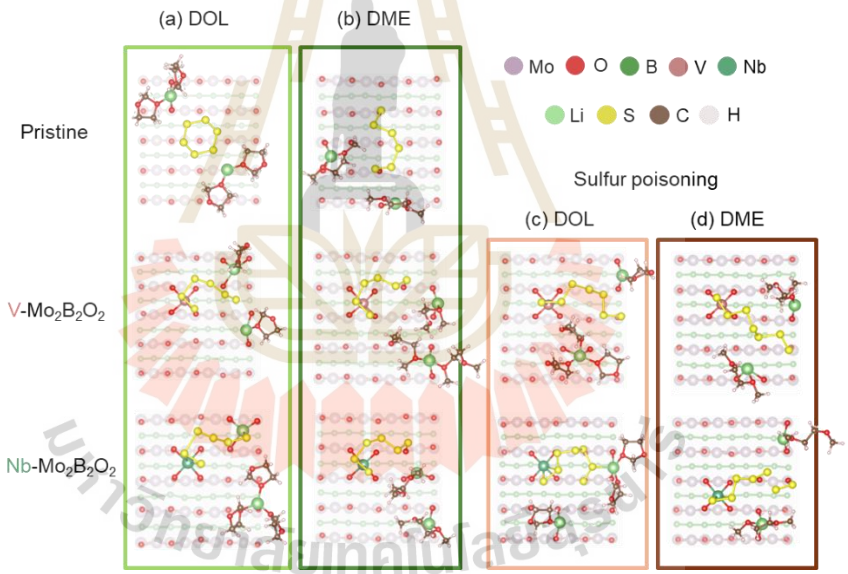

Figure 7.10. Low-energy configurations of (a) DME- and DOL-solvated Li_2S_6, and (c) DME- and (d) DOL-solvated Li_2S_6 under sulfur poisoning on candidates SA-$Mo_2B_2O_2$. All configurations were calculated using AIMD with a time step of 1 fs for 10 ps.

In summary, both pristine and SA-$Mo_2B_2O_2$ effectively facilitate Li_2S decomposition and Li diffusion, enhancing reaction kinetics during the oxidation process. Moreover, the strong sulfur adsorption at the SA site promotes the formation of larger polysulfides by aggregating sulfur anions on both the $Mo_2B_2O_2$ surface and the SA site.

7.3 Reference

Akridge, J. R., Mikhaylik, Y. V., and White, N. (2004). Li/S fundamental chemistry and application to high-performance rechargeable batteries. *Solid State Ionics, 175*(1), 243-245.

Arneson, C., Wawrzyniakowski, Z. D., Postlewaite, J. T., and Ma, Y. (2018). Lithiation and Delithiation Processes in Lithium–Sulfur Batteries from Ab Initio Molecular Dynamics Simulations. *The Journal of Physical Chemistry C, 122*(16), 8769-8779.

Assary, R. S., Curtiss, L. A., and Moore, J. S. (2014). Toward a Molecular Understanding of Energetics in Li–S Batteries Using Nonaqueous Electrolytes: A High-Level Quantum Chemical Study. *The Journal of Physical Chemistry C, 118*(22), 11545-11558.

Barchasz, C., Molton, F., Duboc, C., Leprêtre, J.-C., Patoux, S., and Alloin, F. (2012). Lithium/Sulfur Cell Discharge Mechanism: An Original Approach for Intermediate Species Identification. *Analytical Chemistry, 84*(9), 3973-3980.

Boteju, T., Ponnurangam, S., and Thangadurai, V. (2024). MXenes as Effective Sulfur Hosts and Electrocatalysts to Suppress Lithium Polysulfide Shuttling: A Computational Study. *The Journal of Physical Chemistry C, 128*(9), 3652-3661.

Evers, S., Yim, T., and Nazar, L. F. (2012). Understanding the Nature of Absorption/Adsorption in Nanoporous Polysulfide Sorbents for the Li–S Battery. *The Journal of Physical Chemistry C, 116*(37), 19653-19658.

Han, X., Zhang, Z., and Xu, X. (2021). Single atom catalysts supported on N-doped graphene toward fast kinetics in Li–S batteries: a theoretical study. *Journal of Materials Chemistry A, 9*(20), 12225-12235.

Khossossi, N., Panda, P. K., Singh, D., Shukla, V., Mishra, Y. K., Essaoudi, I., Ainane, A., and Ahuja, R. (2020). Rational Design of 2D h-BAs Monolayer as Advanced Sulfur Host for High Energy Density Li–S Batteries. *ACS Applied Energy Materials, 3*(8), 7306-7317.

Li, S., Leng, D., Li, W., Qie, L., Dong, Z., Cheng, Z., and Fan, Z. (2020). Recent progress in developing Li_2S cathodes for Li–S batteries. *Energy Storage Materials, 27*, 279-296.

Li, X., Zai, J., Xiang, S., Liu, Y., He, X., Xu, Z., Wang, K., Ma, Z., and Qian, X. (2016). Regeneration of Metal Sulfides in the Delithiation Process: The Key to Cyclic Stability. *Advanced Energy Materials, 6*(19), 1601056.

Steudel, R., and Chivers, T. (2019). The role of polysulfide dianions and radical anions in the chemical, physical and biological sciences, including sulfur-based batteries. *Chemical Society Reviews, 48*(12), 3279-3319.

Wang, L., Hu, Z., Wan, X., Hua, W., Li, H., Yang, Q.-H., and Wang, W. (2022). Li_2S_4 Anchoring Governs the Catalytic Sulfur Reduction on Defective $SmMn_2O_5$ in Lithium–Sulfur Battery. *Advanced Energy Materials, 12*(20), 2200340.

Wang, L., Wang, Y., and Xia, Y. (2015). A high performance lithium-ion sulfur battery based on a Li_2S cathode using a dual-phase electrolyte. *Energy & Environmental Science, 8*(5), 1551-1558.

Wu, T., Qi, J., Xu, M., Zhou, D., and Xiao, Z. (2020). Selective S/Li_2S Conversion via in-Built Crystal Facet Self-Mediation: Toward High Volumetric Energy Density Lithium–Sulfur Batteries. *ACS Nano, 14*(11), 15011-15022.

Ye, H., Li, M., Liu, T., Li, Y., and Lu, J. (2020). Activating Li2S as the Lithium-Containing Cathode in Lithium–Sulfur Batteries. *ACS Energy Letters, 5*(7), 2234-2245.

Zhang, L., Sun, D., Feng, J., Cairns, E. J., and Guo, J. (2017). Revealing the Electrochemical Charging Mechanism of Nanosized Li_2S by in Situ and Operando X-ray Absorption Spectroscopy. *Nano Letters, 17*(8), 5084-5091.

Zhou, G., Zhao, S., Wang, T., Yang, S.-Z., Johannessen, B., Chen, H., Liu, C., Ye, Y., Wu, Y., Peng, Y., Liu, C., Jiang, S. P., Zhang, Q., and Cui, Y. (2020). Theoretical Calculation Guided Design of Single-Atom Catalysts toward Fast Kinetic and Long-Life Li–S Batteries. *Nano Letters, 20*(2), 1252-1261.

CHAPTER VIII

CONCLUSIONS

In this thesis, we employed the first-principles method to study how single atom deposited on $Mo_2B_2O_2$ affects performance of Li-S batteries. We focused on improving the adsorption of LiPSs, enhancing catalytic activity for SRR, and facilitating Li_2S decomposition. In the most stable configurations of all SA-$Mo_2B_2O_2$, the SA prefers to adsorb at the hollow site with four oxygen atoms. The strong SA adsorption is influenced by various properties, including atomic number, atomic weight, covalent radius, d-band center, and charge transfer of the SA. Ti and Zr exhibit the strongest adsorption on $Mo_2B_2O_2$ in their periods.

We further studied LiPSs adsorption, using Li_2S_6 molecules as a representative for all LiPSs. The calculated results suggest that the presence of SA improve absorptivity of Li_2S_6, especially V- and Nb-$Mo_2B_2O_2$ which show strongest adsorption. Due to strong adsorption, SA-$Mo_2B_2O_2$ transform Li_2S_6 molecules into more linear-like chain structure, promoting the conversion of Li_2S_6 into short-chain sulfur. Additionally, when considering solvent effects, both V- and Nb-$Mo_2B_2O_2$ continue to bind with polysulfides, suggesting suppression of the dissolution of large LiPSs and the shuttle effect. The strong Li_2S_6 adsorption on SA-$Mo_2B_2O_2$ is influenced by both electronic and geometric properties. For 3*d*-transition metals, electronic properties like charge transfer, d-band center, and atomic number primarily affect Li_2S_6 adsorption. In contrast, for 4*d*-transition metals, properties like SA-O bond length and atomic radius play a more significant role. Additionally, the electron filling also affects Li_2S_6 adsorption energy, leading to different adsorption trends between 3*d*- and 4*d*-transition metals.

The difference can be explained by ligand field theory, as late 3*d*-transition metals exhibit a changing electron filling pattern, while 4*d*-transition metals maintain the same pattern. Additionally, selective orbital coupling analysis provides insights consistent with the findings derived from Ligand Field Theory.

Besides LiPSs adsorption, the SRR catalytic activity of cathode material should exhibit good performance. In this this thesis, most SA-$Mo_2B_2O_2$ can facilitate SRR conversion process without significant overpotential, whereas pristine material exhibits overpotential during the conversion from Li_2S_8 to Li_2S_6.

Interestingly, in the decomposition of Li_2S, both pristine and SA-$Mo_2B_2O_2$ show breaking of Li-S bond without a significant energy barrier. Furthermore, pristine, V- and Nb-$Mo_2B_2O_2$ also exhibit Li diffusion without an energy barrier. These advantages can reduce sluggish kinetics during the delithiation process. Although SA-$Mo_2B_2O_2$ is prone to sulfur poisoning due to the strong SA-S bond interaction. They maintain similar LiPS adsorptivity and suggest the formation of larger polysulfides through sulfur anion aggregation during oxidation process.

Overall, we suggest that the presence of SA enhances absorption, improves catalytic activity for SRR, and resolves issues related to Li_2S decomposition. Therefore, these findings provide guidance for future experimental and theoretical studies on SA-$Mo_2B_2O_2$ to enhance the performance of Li-S batteries.

APPENDIX

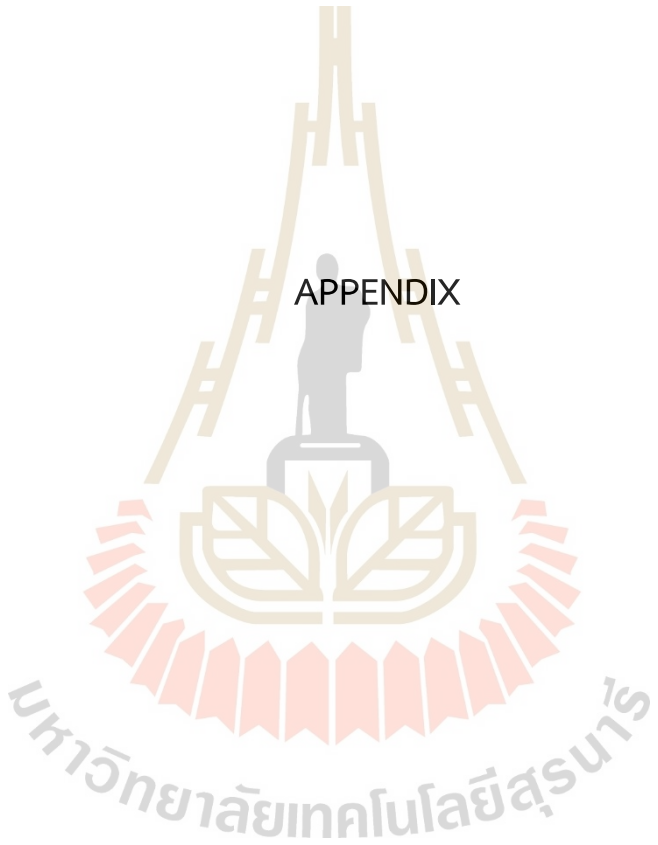

APPENDIX

PUBLICATION AND PRESENTATIONS

A.1 List of publication

- Zhao, H., Xin, X., Tian, L., Siritanon, T., Suthirakun, S., Kaewraung, W., Menghang, Q., Ruoxiu, X., Jingyi, R., Jiang, P. (2024). Novel Mn^{5+}-activated Ba_2TiO_4 phosphor emitting in the second near-infrared biological window. Progress in Solid State Chemistry, 76, 100493.
- Singsen, S., Untarabut, P., Kaewraung, W., Ngamwongwan, L., Prasongkit, J., & Suthirakun, S. (2024). Strain and External Electric Field Engineering of S-Terminated MXene on Selective and Sensitive Detection of N-Containing Compound Gases: A Computational Study. Langmuir, 40(43), 22693-22704.
- Wang, Z., Tian, L., Suthirakun, S., Kaewraung, W., Verma, A., Yu, Y., Bin, W., Peng, J., Hang, Z., Xin, X., Subramanian, M. A. (2025). Study on the novel green magnetoplumbite-type oxide $BaZn_{6-x}Ni_xTi_6O_{19}$: synthesis, structure and properties. Applied Surface Science, 679, 161185.
- Wang, Z., Wang, Q., Liu, Q., Suthirakun, S., Kaewraung, W., Jiang, P., Hang, Z., Xin, X., Subramanian, M. A. (2024). Application and Properties of Co^{2+}-Doped $BaAl_2Si_2O_8$ Blue Pigments in Glazes. ACS Applied Optical Materials, 2(2), 313-322.

A.2 List of presentations

- Kaewraung, W.; Singsen, S.; Junkaewc, A.; Suthirakuna S., Theoretical Investigation of Enhanced C_2N through Transition Metal Doping for Sodium-Sulfur Batteries, The 27th International Annual Symposium on Computational Science and Engineering, Chulalongkorn University, Thailand, 30th July – 3rd August 2024. (Oral presentation)
- Kaewraung, W.; Singsen, S.; Ngamwongwan L.; Junkaewc, A.; Suthirakuna S., Computational Screening of Transition Metal Doped $Mo_2B_2O_2$ as Cathode Materials of Li-Sulfur Batteries, The 26th International Annual Symposium on Computational Science and Engineering, CHE-O12, A-One the Royal Cruise Hostel Pattaya, Thailand, 20th July – 22nd July 2023. (Oral presentation)
- Kaewraung, W.; Singsen, S.; Ngamwongwan L.; Junkaewc, A.; Suthirakuna S., Computational Screening of Transition Metal Doped $Mo_2B_2O_2$ as Cathode Materials of Li-S Batteries, The 4th Materials Research Society of Thailand International Conference, S12_P3, Sunee Grand Hotel & Convention Center, Thailand, 28th February – 4th March 2023. (Poster presentation)

Abstract submitted in The 27th International Annual Symposium on Computational Science and Engineering

ANSCSE27 Bangkok — The 27th International Annual Symposium on Computational Science and Engineering

Theoretical Investigation of Enhanced C_2N through Transition Metal Doping for Sodium-Sulfur Batteries

Wongsathorn Kaewraung[1], Sirisak Singsen[2], Anchalee Junkaew[3]*, and Suwit Suthirakun[1]*
[1]*School of Chemistry, Institute of Science, Suranaree University of Technology, Nakhon Ratchasima, Thailand 30000*
[2]*School of Physics, Institute of Science, Suranaree University of Technology, Nakhon Ratchasima, Thailand 30000*
[3]*National Nanotechnology Center (NANOTEC), National Science and Technology Development Agency (NSTDA), Pathum Thani, Thailand 12120*
*A. Junkaew: anchalee@nanotec.or.th and S. Suthirakun: suthirak@sut.ac.th

Introduction

Metal-sulfur batteries have been proposed as a next-generation energy storage technology due to their high theoretical capacity and energy density. Among them, sodium-sulfur (Na-S) are particularly promising due to their high theoretical capacity, nontoxicity, environmental friendliness, and low cost. However, Na-S batteries still face challenges in terms of capacity and cycling stability due to shuttle effect and sluggish kinetics of sulfur reduction reaction (SRR).[1] Recently, C_2N, new 2D monolayer, has been shown to improve the performance of Na-S batteries, although it still have problem form Na-trapping.[2] To solve this problem and enhance catalytic activity, transition metal doping could be considered. Herein, in this presentation, we design transition metal doping on C_2N using first-principles methods, focusing on iron (Fe) and cobalt (Co) due to strong interaction with sodium polysulfide (NaPSs) and their popularity in experimental studies. We study and compare the performance of single-atom and dual-atom in alleviating shuttle effect and enhancing the delithiation reaction, aiming to provide a deeper understanding. Ultimately, we could suggest new transition metal doping C_2N for future high-performance Na-S batteries.

Methodology

All calculations are carried out using the spin polarized DFT method as implemented in Vienna ab initio simulation package (VASP 5.4). The frozen-core projector augmented wave (PAW) method was used to describe the electron-ion interaction. The exchange-correlation contributions were approximated by the generalized gradient approximation (GGA) with Perdew-Burke-Ernzerhof (PBE). Weak van der Waals interactions between the adsorbates and TM-C_2N were partially corrected using the DFT-D3 method with Becke-Jonson damping. The surface structures were optimized with a kinetic energy cutoff of 500 eV and were used k-point sampling of the Monkhorst-Pack scheme as 4 x 4 x 1 for structural optimization and 9 x 9 x 1 for electronic properties. The optimization is completed where the energy difference was 10^{-6} eV, and the calculation of residual forces lower than 0.02 eV/Å for convergence criteria.

Results and Discussion

Starting with results comparing TM doping and bare C_2N, we found that doping with TM suggest strong interaction with NaPSs, like adsorption on bare C_2N. However, TM-C_2N could avoid Na Trapping. When examining the adsorption on C_2N when Na trapping, it shows decreased performance in the adsorption of NaPSs. Consequently, doping with TM could be alternative to resolve Na trapping in C_2N while maintaining strong adsorption with NaPSs.

Focusing on different performance between single-atom and dual-atom, doping with dual-atom show stronger NaPSs adsorption compared to single-atom doping due to the increased number of active transition metal sites that bind with sulfur in NaPSs. However, both same dual-atom transition metal (Fe-Fe and Co-Co) and different dual-atom transition metal (Co-Fe) exhibit similar adsorption energy, suggesting that using different transition metals, when both metal groups are next to each other, does not significantly affect adsorption with NaPSs.

Studying the catalytic activity through Gibbs free energy profile during SRR, computational results show that Co-Fe doping reduces the energy of the potential limiting step in the Na_2S_4 to Na_2S_2 conversion more effectively than the same dual-atom combinations (Fe-Fe and Co-Co) and single-atom doping. This suggests that different dual-atom doping on C_2N could more effectively accelerate the SRR process.

From the examples explained above, it could be summarized that dual-atom C_2N, especially Co-Fe doped C_2N, shows better performance. Additionally, all the results in this work could guide and suggest directions for future research, leading to the discovery of high-performance Na-S batteries.

Significance

This research addresses a significant challenge and improvement in the field of sodium-sulfur (Na-S) batteries by exploring transition metal doping on C_2N monolayers through single-atom and dual-atom transition metals.

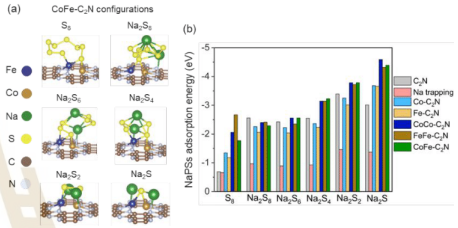

Figure 1. (a) The most stable adsorption configurations of S_8 and NaPSs on CoFe-C_2N. (b) Adsorption energy of S_8 and NaPSs when adsorbed on bare C_2N, Na trapping (Na doped on C_2N), single-atom doping, and dual-atom doping.

References

1. Manthiram, A., Yu, X. *Small* 11, 2108-2114 (2015).
2. Sajjad, M., Hussain, T., Singh, N., and Larsson, L.A. *Langmuir* 36, 13104-13111 (2020)

Abstract submitted in The 26th International Annual Symposium on Computational Science and Engineering

The 26th International Annual Symposium on Computational Science and Engineering (ANSCSE26) *8-11 July 2023*

COMPUTATIONAL SCREENING OF TRANSITION METAL DOPED $Mo_2B_2O_2$ AS CATHODE MATERIALS OF LI-SULFUR BATTERIES

Wongsathorn Kaewraung[1], Sirisak Singsen[2], Lappawat Ngamwongwan[2], Anchalee Junkaew[3*], Suwit Suthirakun[1*]

[1]*School of Chemistry, Institute of Science, Suranaree University of Technology,Nakhon Ratchasima, Thailand 30000*

[2]*School of Physics, Institute of Science, Suranaree University of Technology, Nakhon Ratchasima, Thailand 30000*

[3]*National Nanotechnology Center (NANOTEC), National Science and Technology Development Agency (NSTDA), 111 Thailand Science Park, Pathum Thani, Thailand 12120*

*Corresponding address (E-mail: anchalee@nanotec.or.th; suthirak@sut.ac.th)

Lithium-sulfur batteries have been proposed as a next-generation energy storage technology owing to their high theoretical energy density. However, they are limited by capacity fading and cycling stability caused by the shuttle effect from soluble lithium polysulfides (LiPSs), and the sluggish decomposition of small LiPSs. In this presentation, I will discuss the design strategy for promising cathode materials based on two-dimensional transition metal boride (MBene), $Mo_2B_2O_2$, using first-principles methods. Various transition metal atom doping as single-atom catalysts (TM-$Mo_2B_2O_2$) was explored to alleviate the shuttle effect and reduce the energy barrier of the delithiation reaction during the charging process. Our computational studies suggest that the presence of TM doping can significantly enhance Li polysulfide (LiPS) adsorption due to the strong formation of TM-S and Li-O bonds, which can help to prevent LiPS dissolution and inhibit the shuttle effect. TM doping can facilitate the delithiation kinetics of small LiPS by reducing the energy barrier. Furthermore, the type of transition metal doping can influence the adsorption energy and reactions in the charging process due to the distinct characteristics of each transition metal atom. In summary, we suggest that all TM-$Mo_2B_2O_2$ is a promising cathode material that can accelerate the reactions of Li-S batteries. Our finding provides useful guidance for the rational design of new MBene cathodes for high-performance Li-S batteries.

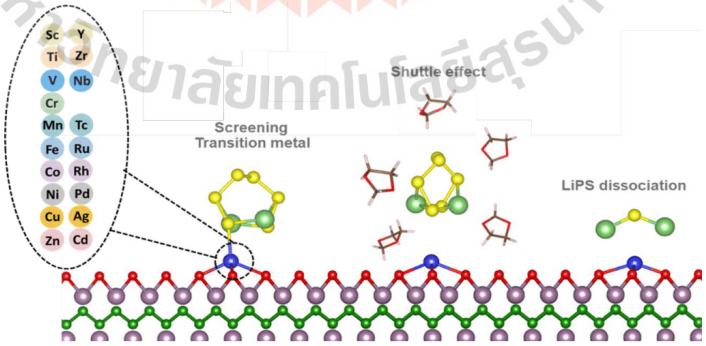

Keywords: Lithium-sulfur batteries, Single-atom catalysts, Transition metal borides (MBene), Density functional theory, First-principles method

Abstract submitted in The 4th Materials Research Society of Thailand International Conference

The 4th Materials Research Society of Thailand International Conference
(MRS-Thailand 2023) 28 February – 4 March 2023
Ubon Ratchathani, Thailand

Computational Screening of Transition Metal Doped $Mo_2B_2O_2$ as Cathode Materials of Li-S Batteries

Wongsathorn Kaewraung[a], Sirisak Singsen[a], Lappawat Ngamwongwan[a], Anchalee Junkaew[b,*], Suwit Suthirakun[a,*]

[a] *School of Chemistry, Institute of Science, Suranaree University of Technology, Nakhon Ratchasima, Thailand 30000*
[b] *National Nanotechnology Center (NANOTEC), National Science and Technology Development Agency (NSTDA), 111 Thailand Science Park, Pathum Thani, Thailand 12120,*

*Corresponding Author's E-mail: anchalee@nanotec.or.th, suthirak@sut.ac.th

Abstract

Lithium-sulfur batteries are one of the alternative next-generation energy storage devices because of their high theoretical energy density. However, they still have major challenges such as poor capacity and cycling stability occurring from shuttling of lithium polysulfides (LiPSs), and sluggish decomposition of small LiPSs. Here, using first-principles methods, we computationally design promising cathode materials based on two-dimensional transition metal boride (MBene), $Mo_2B_2O_2$. Various transition metal atom doping (TM-$Mo_2B_2O_2$) was screened to suppress the shuttle effect and accelerate the delithiation reaction during the charging process. Our computations reveal that the doped $Mo_2B_2O_2$ substrates can substantially enhance the LiPS adsorption due to the strong formation of TM-S and Li-O bonds. Such strong adsorptions contribute to preventing LiPS dissolution and inhibiting the shuttle effect. The presence of TM doping also facilitates delithiation kinetics of small LiPS. From computational perspective, we suggest that TM-$Mo_2B_2O_2$ are promising candidate cathodes. The study serves as useful guidance to rationally design new MBene cathodes for high-performance Li-S batteries.

Keywords: Lithium-sulfur batteries, Single-atom catalysts, Transition metal borides (MBene), Density functional theory, First principles method

CURRICULUM VITAE

Wongsathorn Kaewraung was born on August 14th, 1999, in Bangkok, Thailand. He received his B.Sc. in Physics (first-class honors) in 2021 from the Department of Chemistry, Faculty of Science, Kasetsart university, Thailand. He has been granted a scholarship from the Development and Promotion of Science and Technology Talents Project (DPST, THAILAND) since 2018. During his bachelor's degree, he started research in experimental materials science for developing anode materials for lithium-ion batteries and formic-acid fuel cells under the supervision of Asst. Prof. Dr. Panitat Hasin and Asst. Prof. Dr. Patraporn Luksirikul. In the master's degree program at School of Chemistry, Suranaree University of Technology, Thailand, he changed to focus on density functional theory for screening cathode materials for metal-sulfur batteries under the supervision of Assoc. Prof. Dr. Suwit Suthirakun. In 2023, He was a graduate research assistant at Graduate School of Chemical Sciences and Engineering, Hokkaido University, Japan, under supervision of Assoc. Prof. Min Gao. He has published articles in participated in international conferences (listed in APPENDIX C) during the course of his master's program.